POLITECNICO DI TORINO

MASTER's Degree in ENERGY AND NUCLEAR ENGINEERING

MASTER's Degree Thesis

Investigation of the Impact of Magnetic Island Geometric Parameters on Divertor Performance in Stellarators

Advisors

Prof. Fabio SUBBA

Dr. Felix REIMOLD

Co-advisor

Nassim MAAZIZ

Candidate

Francesco ONORATI

MARCH 2026

Abstract

Nuclear fusion power represents a possible secure and carbon-free energy source, offering a sustainable solution to future global energy demands. As of today, magnetic confinement fusion (MCF) is the most promising and investigated approach to employ thermonuclear fusion for large-scale energy production. In this context, three-dimensional, non-axisymmetric magnetic devices, called stellarators, represent a promising pathway for steady-state reactor operation. In these devices, managing the high particle and energy fluxes that exit the confined plasma and enter the boundary region, the so-called Scrape-Off Layer (SOL), remains a critical challenge to ensure the integrity of plasma-facing components and the performance of the confined plasma. The island divertor is a leading power exhaust concept for stellarators, utilizing intrinsic magnetic islands to safely channel power and particles in the SOL to a localized surface, the divertor target plates.

Operating the divertor in a regime called detachment is highly desired, as it leads to power starvation at the targets, which mitigates the risk of thermal overload and reduced erosion on/off plasma-facing components. While complete detachment has been successfully achieved in the Wendelstein 7-X (W7-X) island divertor, current experiments are underpowered and significant challenges remain for viable extrapolation to a reactor. Divertor capabilities, such as particle exhaust and radiative power dissipation, scale strongly with divertor density. However, significantly lower divertor density has been obtained in W7-X in comparison to tokamaks. It has been shown that the geometry of the magnetic islands affects the performance of the island divertor. Specifically, island radius r_i, field line pitch Θ, and target placement have been identified as divertor-relevant geometric parameters.

In the present thesis, the extent to which these island geometry parameters affect divertor performance is analyzed through a systematic parametric study. Using a simplified island model based on the Hamiltonian Grids (HaGrids) code, specific points in the $r_i - \Theta$ design space are selected for comparison and various target placements are evaluated. Fully 3D, self-consistent edge plasma and neutral transport simulations are then performed across the selected parameter space using the EMC3-EIRENE code package.

Simulations show that target density build-up generally improves with an increase

in island radius, but an optimal trade-off with the field line pitch is required. Notably, configurations with larger r_i and Θ values with respect to the basic W7-X-like case exhibit a novel "neutral-transparent O-point" regime. This state is characterized by a low-temperature, neutral-dense volume surrounding the O-point that, if physically realizable, could potentially be exploited in future closed divertor designs to shield target plates from direct plasma interaction. Three target configurations are simulated. When targets are placed on the outboard side of the torus, target concavity, which increases neutral retention in the island, and to a lesser extent total flux expansion, improve density build-up in the divertor.

Finally, density build-up on the field lines within the Power Carrying Layer (PCL) is discussed for the different configurations. Differences in field line behavior are tackled utilizing the Stellarator Two-Point Model (STPM) framework. Quantities such as parallel heat flux $q_{\parallel}$, Θ, and connection length L_c are used to elucidate the underlying differences in density build-up across configurations. A STPM onion-skin method is applied to evaluate the extent to which the analytical model can be used to predict target conditions in the different configurations. While the method qualitatively reproduces the peaks and general trends along the target, it overestimates temperatures and underestimates density within a factor of 2. Furthermore, a better agreement is achieved when $q_{\parallel}$ is evaluated downstream rather than upstream. Discrepancies can likely be attributed to the fact that flux surface $\perp$ transport toward the island O-point is not accounted for in the STPM.

Keywords: Nuclear fusion, Stellarator, Island divertor, EMC3-EIRENE, Plasma physics, SOL transport, modelling

Table of Contents

Chapter 1

Introduction

1.1 Nuclear Fusion

Energy is a fundamental quantity in physics. However, as a broader concept, it has expanded to various other disciplines. It pervades human evolution since the discovery of fire [1] and it is one of the key aspects dictating political behavior today.

Despite its importance, the concept of energy as we use it today is fairly young. Born in the 1840s and 1850s in thermodynamics and denoted as the "capacity of doing work", it started to expand outside of the physical and technical domains only during the twentieth century, as energy consumption rose and energy sources started to be critical. While the management of energy resources has been a strategic concern since the Industrial Revolution, the energy crises of the 1970s catalyzed the development of formalized, comprehensive energy policies [2].

Nowadays, energy plays an essential role in economical and political decision-making, shaping our individual and collective life. Despite this, the related challenges risk to outnumber the solutions: the modern age of fossil fuels can last just so long as the resources last [3] and supply of critical minerals for renewable energy sources remains problematic. In addition to this, climate change poses limits to net zero CO_2 emissions, while escalating conflict in the Middle East and Ukraine, along with energy market crises, are exposing the underlying fragility of the global energy system [4], showing more and more the need for secure energy, not bound to importing and exporting nations.

This already critical situation is not expected to heal on its own, as energy demand, in particular electrical, is pictured to grow tirelessly in the coming years [5]. While many of the experts and policy makers assess clean electricity to be the future, infrastructure and clean supply cannot keep up with the increasing demand and, therefore, new choices of energy production need to be implemented.

In this context, nuclear fusion power emerges as a secure and carbon-free energy source, capable of very high energy densities, widespread fuel availability and minimal CO_2 equivalent emissions [6].

However, while the prospect of nuclear fusion power holds great promise for the world, its realization is by no means guaranteed. Today scientists are still working in the unprecedented effort of building a nuclear fusion reactor; and while a lot of research is still needed, incredible milestones have been achieved so far (including a net production of energy in 2022 [7]) and much more are expected in the years to come [8]. In fact, the current decade has seen a worldwide renewed interest in fusion [9], with increased state-funded pursuit and global private investments surpassing US $10 billion [10].

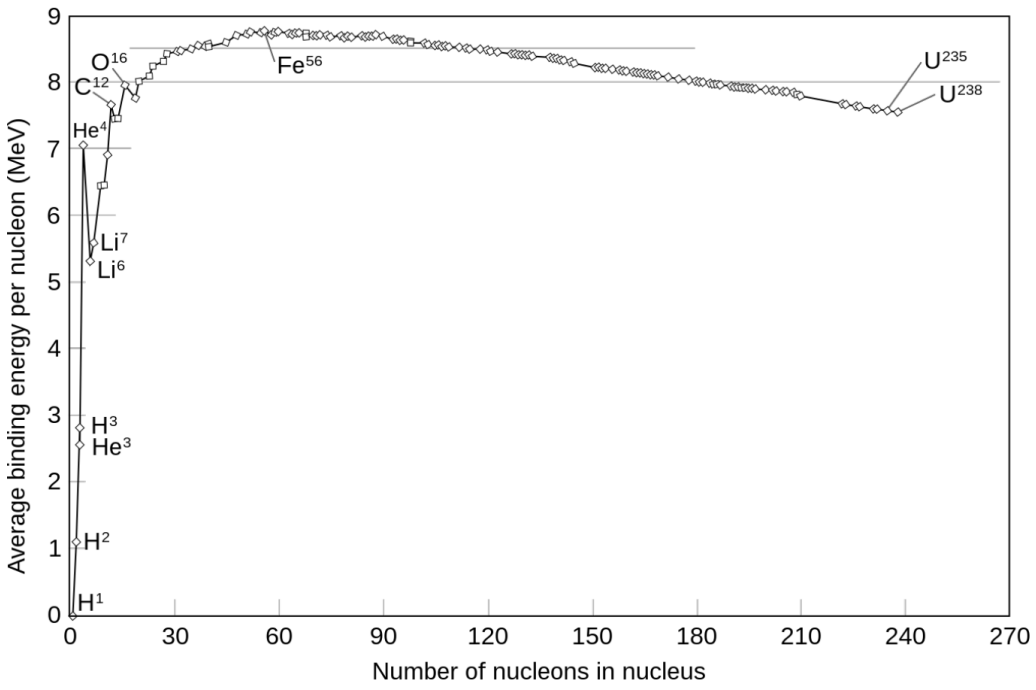

Figure 1.1: Nuclei binding energy per nucleon

The physical basis of nuclear fusion power involves a reaction in which two atomic nuclei combine to form a larger one, plus other products. Fusion is an exothermic reaction for elements with atomic mass less than the one of Fe_{56}, while it is endothermic for elements with a higher mass. This is due to the interplay of short range nuclear force and electrostatic Coulomb force in defining the binding energy for different atomic species. As atomic mass increases, the binding energy is determined by the strong attractive nuclear force, that eventually saturates for heavier nuclei. After the saturation, a low electrostatic repulsive force dominates the binding energy, slowly reducing it and creating a profile peaked at medium size elements, Fig. 1.1.

Consequently, fusing light elements pushes one up the curve to more strongly bound heavier elements implying that energy will be released by such reactions; while at the same time creating a mass defect in the products of the fusion reaction with respect to the reactants.

Reaction rates for fusion reactions are obtained as the convolution of the energy-

dependent fusion cross section with the thermal velocity distribution of the reacting ions, which is usually well defined by a Maxwellian distribution.

In order for two nuclei to undergo a fusion reaction, they need a high momentum to overcome the very high repellent Coulomb force of the positively charged nuclei at distances short enough to allow the strong interaction to dominate. This is why fusion reaction rates Fig. 1.2 have very high temperature/energy thresholds. At this state, the only viable medium in which fusion can occur is that of a hot, thermalized and confined plasma.

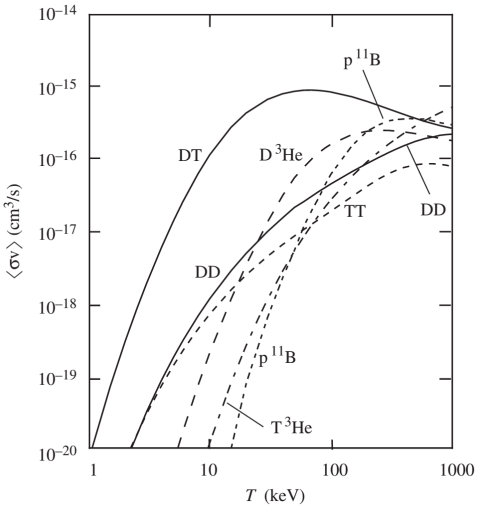

Figure 1.2: Reaction rates for various fusion reactions.

Out of the considered light-weight atoms fusion reactions, the one with the highest reaction rate and lower temperature threshold is Deuterium–Tritium fusion (D-T fusion). This makes it the most promising candidate for present and future fusion reactor experiments.

$$^2_1\mathrm{H} + ^3_1\mathrm{H} \rightarrow ^4_2\mathrm{He} + ^1_0\mathrm{n} + 17.6\,\mathrm{MeV} \tag{1.1}$$

In order for a nuclear fusion reactor to be feasible, it has to satisfy a *power balance* requirement $P_{out} \gg P_{in}$ [11]. After providing an initial heating power, the reactor has to reach a stationary state in which the fusion heating power has to be sufficiently large to match the radiative (Bremsstrahlung) and thermal conduction losses:

$$P_f > P_r + P_\kappa \tag{1.2}$$

When this happens, the plasma has reached *ignition*. If we consider an ideal plasma, having electrons and ions at the same temperature T, expressed in eV, and Deuterium and Tritium ions being each a half of the electron density n, we can rewrite Eq. 1.2 as:

$$k_f\langle\sigma v\rangle n^2 > k_r n^2 T^{\frac{1}{2}} + \frac{3nT}{\tau_e} \tag{1.3}$$

Where k_f and k_r are constants, and τ_e is the energy confinement time, which is a measure of how long the plasma's thermal energy is confined within the plasma before escaping.

Rearranging, we obtain the expression:

$$nT\tau_e > \frac{3T^2}{k_f\langle\sigma v\rangle - k_r T^{\frac{1}{2}}} \approx \frac{3T^2}{k_f\langle\sigma v\rangle} \tag{1.4}$$

Which is known as the fusion triple product, an extension of the Lawson Criterion

[12] that is a well known figure of merit for thermonuclear fusion reactions.

Knowing that the minimum value of the triple product with respect to temperature is in the range of 10-20 keV [13], we can use the representation of the average $\langle \sigma v \rangle$ in that range:

$$\langle \sigma v \rangle \approx 1.1 \cdot 10^{-24} T^2 \ \frac{m^3}{s} \tag{1.5}$$

Then, knowing that $k_f = \frac{E_\alpha}{4}$ and E_α, which is the energy carried by the fusion alpha particles, is $\approx 3500 keV$, Eq. 1.4 becomes:

$$nT\tau_e > \frac{4 \cdot 3 \cdot T^2}{3.5 \cdot 1.1 \cdot 10^3 \cdot 10^{-24} \cdot T^2} \approx 3 \cdot 10^{21} \ \frac{keVs}{m^3} \tag{1.6}$$

Which means that, in order for the D-T fusion plasma to sustain itself, the triple product has to satisfy this condition. This is a very useful form, since it underlines that, in order to reach ignition, requirements are needed on density, temperature and confinement time.

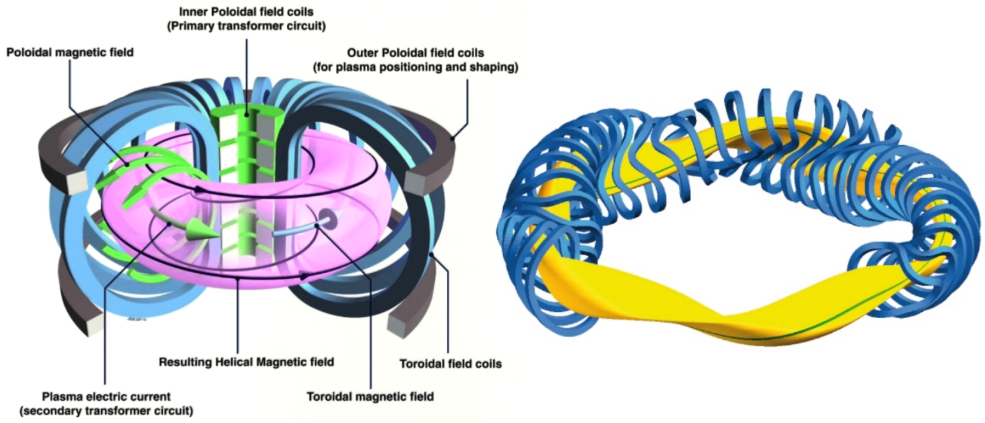

Figure 1.3: Left: scheme of a tokamak [14]. Right: scheme of a Stellarator [15].

1.2 Magnetic Confinement Fusion

To satisfy the Lawson criterion for D-T fusion reactor, the operational temperature is theoretically optimized within a window of $T \approx 10$–$15 \ keV$, where the required Lawson triple product reaches its theoretical minimum. While current-day experiments rarely achieve this ion temperature simultaneously with reactor-relevant densities, this theoretical temperature optimization means that the path to ignition relies on increasing either the plasma density n or the energy confinement time τ_E.

Choosing which parameter to focus on increasing is what differentiates the two most common branches of thermonuclear fusion research: inertial and magnetic confinement fusion.

In inertial confinement fusion (ICF), cryogenic capsules containing a layer of solid

D-T fuel are isotropically heated by intense laser or ion beams. The surface of the pellet ablates, compressing the inner part of the pellet to conditions of $n \approx 10^{31}$–10^{32} m^{-3} and $T \approx 10$ keV [16]. This method aims to satisfy Lawson criterion by reaching these high densities for a brief inertial confinement time, $\tau \approx 10$–100 ps [17]. ICF schemes were developed in direct drive and later expanded to indirect drive. In direct drive, the laser (or ion) beams are directed directly onto the surface of the target capsule. In indirect drive, the driver energy is first absorbed in a high-Z enclosure (a hohlraum), which surrounds the fuel capsule [18]. The material heated by the driver emits X-rays, which drive the capsule implosion.

Due to relaxed requirements on laser beam uniformity, and reduced sensitivity to hydrodynamic instabilities, several efforts were made on indirect drive ICF [19]. This approach has been the first fusion technology to reach Q > 1 at present [7].

In magnetic confinement fusion (MCF), charged particles are confined via magnetic fields, producing much bigger and less dense ($n \approx 10^{20}$ m^{-3}) plasmas confined for a much longer time ($\tau_e \approx 1$ s).

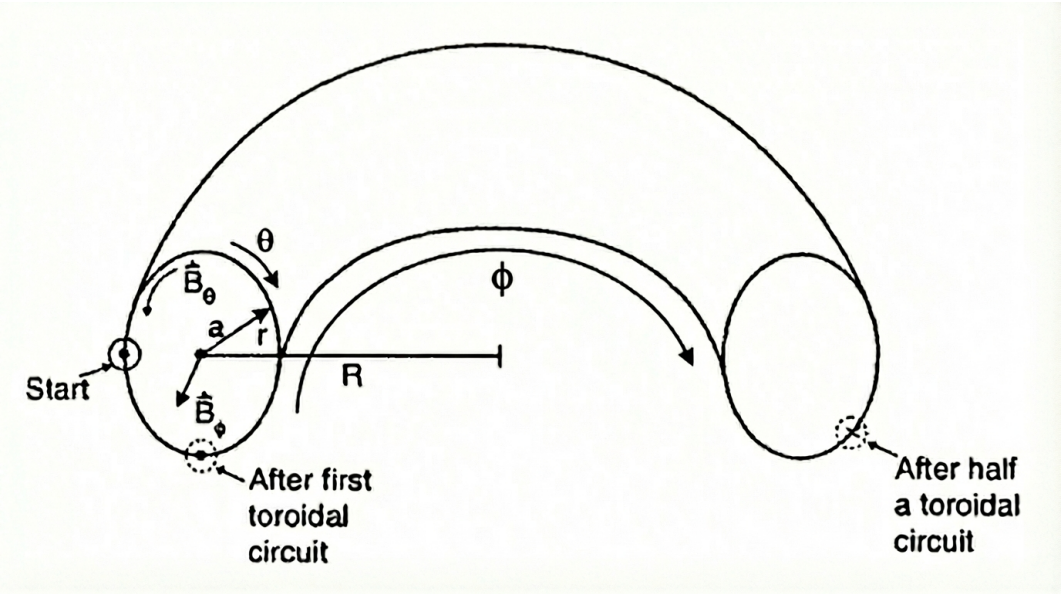

Figure 1.4: Schematic of a toroidal flux surface on which a particle is confined. Arrows identify the torus coordinates (r, ϑ, φ) [20].

Magnetic confinement exploits the Lorentz force that a charged particle experiences when subject to a magnetic field. The particles spiral around the magnetic field lines along helical trajectories, so called gyro-motion. The particles are hence confined perpendicular to the field. Parallel to the field they are free to move and would be lost very quickly. This is why fusion configurations are bent to form a torus and a so called toroidal magnetic field constraints the particles into an equilibrium at a first approximation.

To describe these confinement geometries, we utilize standard torus coordinates (r, ϑ, φ), as illustrated in Fig. 1.4. The macroscopic shape of the torus is defined by

its major radius R and minor radius a. Any local point within the plasma is identified by its radial distance r from the center of the minor cross-section ($0 \leq r \leq a$), the poloidal angle ϑ wrapping the short way around the torus, and the toroidal angle φ traveling the long way around the major axis. The magnetic field components along these angular directions are the poloidal field B_ϑ and the toroidal field B_φ, respectively.

In MCF designs, generating a confining magnetic field structure requires closing the magnetic field onto itself to prevent end losses caused by plasma flowing out along unconfined field lines [13]. Consequently, a toroidal geometry is selected, where magnetic field lines wrap around a torus. This topology forms continuously nested *flux surfaces*. A flux surface is a 2D surface spanned entirely by a single, ergodically traversing magnetic field line, such that the magnetic field vector is everywhere tangential to the surface. Charged particles, before considering cross-field drifts and collective plasma effects, are therefore confined as they stream rapidly along these closed, nested surfaces within the toroidal volume. Along the magnetic field particles thus stay confined on the same torus, without escaping radially.

However, in a purely toroidal magnetic field, the curvature and gradient of the magnetic field, $\nabla\mathbf{B}$, causes ions and electrons to drift vertically in opposite directions. This charge separation generates a strong vertical electric field, $\mathbf{E}$. This induced electric field, interacting with the background magnetic field ,$\mathbf{B}$, drives a severe outward radial $\mathbf{E} \times \mathbf{B}$ drift, effectively pushing the plasma toward the vessel walls and destroying confinement. Macroscopic diamagnetic drifts similarly contribute to this destabilizing potential build-up in a simple toroidal geometry.

A helical magnetic field structure is therefore required to counteract this radial particle motion. By adding a poloidal magnetic field component, B_ϑ, the field lines are forced to twist helically around the torus. A finite field-line twist allows electrons to flow continuously along the field lines, effectively shorting out the potential build-up caused by these diamagnetic drifts.

This required helical twist is quantified by the rotational transform, ι, which measures the average poloidal rotation of a magnetic field line per single toroidal transit. Assuming the existence of toroidally nested magnetic flux surfaces, the rotational transform on such a surface can be defined as:

$$\imath = \frac{\iota}{2\pi} = \frac{d\chi}{d\psi} \tag{1.7}$$

Where $\imath$ is the reduced rotational transform, χ is the poloidal magnetic flux, and ψ the toroidal magnetic flux. The latter two are expressed in Weber, Wb. Depending on the value of $\imath$, a flux surface exhibits fundamentally different topological properties. If $\imath$ is an irrational number, a single field line will never close on itself, instead ergodically covering the entire two-dimensional surface over infinitely many transits. Conversely, if $\imath$ is a rational fraction such that $\imath = \frac{n}{m} \in \mathbb{Q}$, the surface is termed a

rational flux surface. Here, m and n represent the integer poloidal and toroidal mode numbers, respectively. On a rational surface, a magnetic field line closes perfectly upon itself after exactly m toroidal and n poloidal transits.

Rational surfaces hold special physical significance for plasma stability. Because the field lines are periodic and closed, rational surfaces are highly susceptible to resonant magnetic perturbations. If a localized plasma perturbation shares the same m and n mode numbers, it resonates perfectly with the rational surface. This resonance breaks the ideal magnetic topology, causing the nested flux surfaces to tear and reconnect. This magnetic reconnection forms localized, tube-like helical structures called magnetic islands, Fig. 1.6.

The way in which the poloidal magnetic field is obtained is what differentiates the two main approaches to MCF: the tokamak and the stellarator Fig. 1.3. In a tokamak, the poloidal component of the magnetic field is generated by a large toroidal current flowing directly through the plasma. The plasma acts as the secondary winding of a transformer; this current is driven by an induced toroidal electric field, which is created by continuously ramping the magnetic flux within a central solenoid.

Once the maximum solenoid current is reached, the induced voltage vanishes and the plasma current resistively decays. This inductive current drive makes traditional tokamak operation inherently pulsed. For example, ITER is expected to mantain a fusion pulse for a duration of 300 to 500 seconds [21]. However, relying on the internal plasma current to generate the poloidal field provides a significant engineering advantage: the external magnetic coil system can be fully axisymmetric. Consequently, the toroidal field coils can be designed as simple, identical planar loops evenly distributed around the torus.

In a stellarator only external field coils are used to produce the poloidal field, either with optimized modular field coils [22, 23, 24] or by helical coils [25]. This generates a three-dimensional (3D) non-axisymmetric configuration, without an externally driven plasma current. The plasma current in a tokamak provides a source of 'free' energy and can lead to current-driven instabilities including violent plasma termination in so-call disruptions. [26].

1.3 Power exhaust in magnetized plasmas

As introduced with the energy confinement time and Eq. 1.2, particles and energy stored inside the core plasma continuously diffuse outwards with a characteristic time scale τ_e. In MCF, the core plasma is confined within a region of closed magnetic field lines. The particle and energy fluxes eventually exit the closed magnetic confinement and meet a solid wall at the plasma boundary. In this region, called the Scrape-Off Layer (SOL), magnetic field lines become open by intersecting the solid surface. The confined region is separated from the SOL by the Last Closed Flux Surface (LCFS) [27]. These open field lines guide particle and energy fluxes toward the plasma-facing components (PFM) of the solid wall. In contact with the plasma, the solid wall

becomes a sink for the charged particles. Eventually, electrons and ions recombine on the surface and re-enter the plasma as neutral particles. Neutrals in the plasma are subsequently ionized, reaching back the solid wall in a recycling fashion [28].

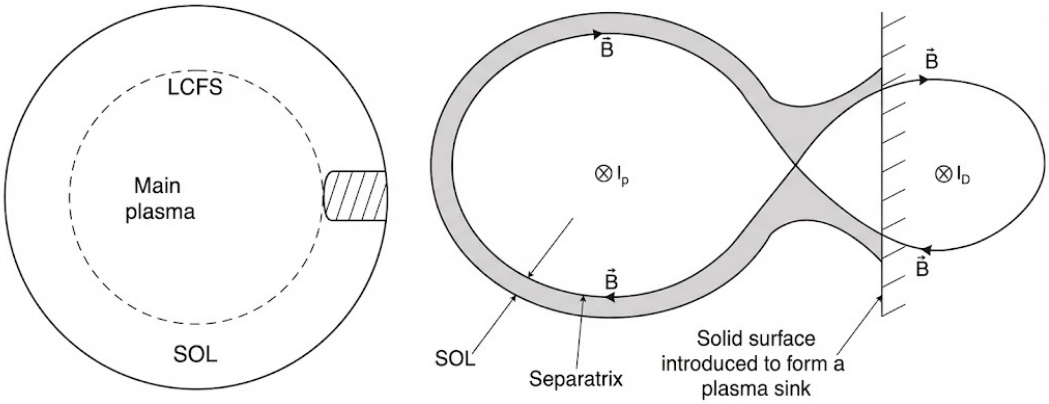

Figure 1.5: Left: Poloidal cross section of a limiter configuration. The toroidal limiter (shaded area) creates a LCFS [28]. Right: Poloidal cross section of a divertor configuration. An external current creates an X-point and the relative separatrix and SOL (in grey) [28].

Two different configurations have been conceptualized to manage the particle and power fluxes exiting the LCFS and entering the SOL during plasma operation: the limiter and the divertor [20].

In the limiter configuration, Fig. 1.5, the plasma's LCFS is determined by the intersection of field lines by a material object, usually a solid material either toroidally or poloidally symmetric. A limiter is, by definition, in direct contact with the plasma. Because of this, neutrals recycled from the material surface and impurities released via sputtering and outgassing [30] tend to pollute the main plasma, causing radiation losses that lead to performance and energy confinement degradation, while also potentially triggering a plasma collapse [13, 31]. Furthermore, limiters tend to produce a very thin SOL, resulting in highly concentrated power loads. These heat flux densities can exceed the technological threshold of $10 - 15\ MW/m^2$ [32], thus severely damaging the PFM.

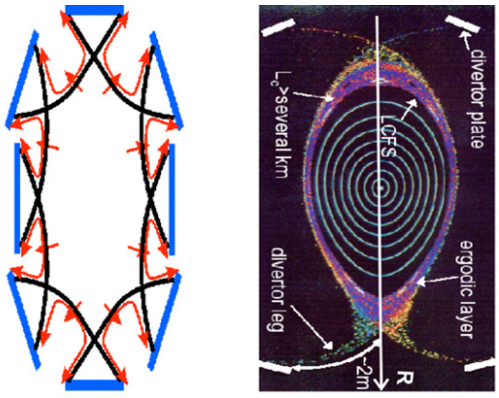

Figure 1.6: Schematics for the island divertor (left) and the Helical Divertor. The Island divertor has a single island chain, while the stochastic layer of the Helical Divertor consists of multiple low-order island chains [29].

In the divertor configuration, direct contact between the confined plasma and the

material surface is avoided by creating or using the magnetic topology to introduce a separatrix. [33]. The requirements for a divertor are [34]:

- Guarantee of plasma confinement.
- Acceptable heat flux on the PFC.
- Sufficient neutral pressure for pumping out helium ash.
- Impurity control for core integrity.

In tokamaks, poloidal divertors have been the main design choice for present and future reactors [35], to their ability to significantly increase both plasma and divertor performance. In this type of divertor, shown in Fig. 1.5, the LCFS is created by adding external current-carrying coils that alter the poloidal magnetic field. This creates a poloidal field null, known as an X-point, and establishes a magnetic separatrix. As a result, the SOL field lines are diverted towards a localized material surface (the divertor targets), creating an isolated region where neutrals can recycle far away from the core plasma. This spatial separation enhances impurity screening and pumping efficiency [34], while simultaneously enabling an easier access to the High-Confinement Mode (H-mode) [36]. Ultimately, divertor geometry and magnetic topology play a fundamental role in determining the exhaust performance of the divertor [37]. Correctly assessing these parameters is therefore an essential step in any divertor design.

In stellarators, the 3D non-axisymmetric magnetic field and first wall structure generate an inherently three-dimensional SOL. Optimizing the divertor geometry is uniquely challenging, as the targets must accommodate the complex magnetic topology of the plasma boundary. Stellarator edge configurations feature helical magnetic structures that interact locally with 3D-shaped divertor plates. Helical SOLs in stellarators are therefore fully three-dimensional.

In stellarators, different MCF devices and thus different divertor configurations are being currently investigated.

- the island divertor of the low-shear stellarators of the Wendelstein family, Fig. 1.6, utilize intrinsic magnetic islands to manage power and particle exhaust.[38, 39, 40]. The targets are created by cutting the edge magnetic islands with divertor plates.
- the helical divertor, Fig. 1.6, developed for high shear machines with overlapping multiple island chains is implemented in the Large Helical Device (LHD) [41]. This design utilizes large helical coils to create a diverting field [42].
- the non-resonant divertor [43] is produced by using magnetic chaos features in the region of sharp edges on the flux surface [44]. This approach leverages sharp "ridges" on the plasma boundary [45] to channel the heat and particle flux. Full experimental and modeling evaluations of the exhaust performance of this divertor are still pending [46].

1.4 Detachment

As outlined in the preceding section, successfully managing the intense heat and particle fluxes exhausted from MCF plasmas remains an essential challenge for future reactor operation. To ensure the longevity and integrity of PFCs, several stringent target requirements must be met. Specifically, the heat loads must be maintained below the material limits of $10-15\ MW/m^2$ to avoid melting, and the target electron temperature must be limited ($T_{e,t} < 5\ eV$) to suppress physical sputtering by keeping incident ion energies below the material's work function. Furthermore, an effective exhaust solution requires strong radiative capabilities to dissipate the thermal energy reaching the target plates volumetrically, alongside high downstream neutral densities for efficient particle pumping. The so-called divertor 'detachment' plasma regime is highly desirable precisely because it fulfills these demanding criteria [28].

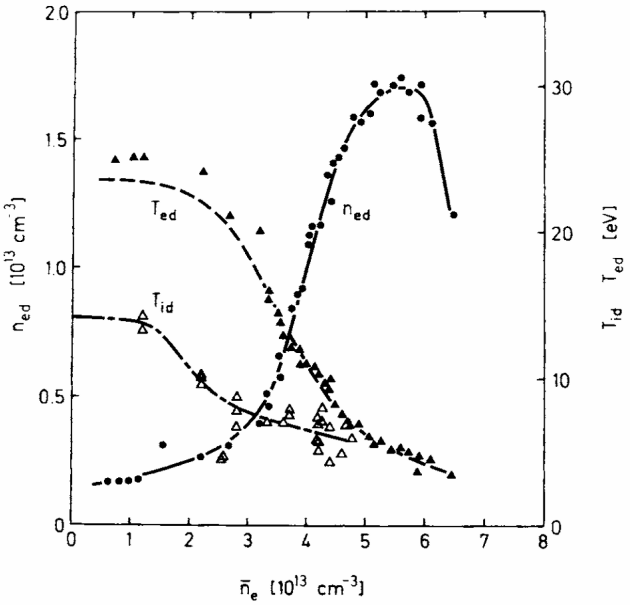

Figure 1.7: Figure demonstrating the density "roll-over" associated with the SOL transition into detachment in ASDEX [47].

Divertor detachment signifies a state in the edge plasma where a large fraction of the thermal power is dissipated via volume radiation, typically from low-Z impurities, concurrent with a significant reduction in both heat (power detachment) and particle (particle detachment) fluxes to the divertor targets.

Fig. 1.7 is used to describe how a plasma achieves detachment. The figure shows Langmuir probe measurements in ASDEX. On the y-axis, electron density n_{ed} at the downstream region of the divertor and target electron and ion temperatures $T_{(e,i),d}$ are showed as functions of the line averaged core density $\overline{n_e}$, (x-axis), which is a main parameter of the fusion triple product, Section 1.1. Following the curves, the divertor is at first in a low-recycling (sheath-limited) regime, where target density n_d increases linearly with upstream density n_u. As $\overline{n_e}$ increases, the divertor transitions to a high-recycling (conduction-limited) regime, where n_{ed} increases rapidly, at least

quadratically, with $\overline{n_e}$ and $T_e d$ drops. Up to the detached phase, the pressure is still conserved on a flux tube, and increasing density (A) implies a drop in the temperature. Finally, local pressure losses decrease the pressure close to the target and the plasma detaches from the material surfaces. As the divertor enters this detached regime, further increases in $\overline{n_e}$ lead to a saturation and subsequent decrease in n_{ed}, called density *rollover*.

While the description above of detachment applies for tokamaks, for stellarators, the 3D magnetic topology of the stellarator SOL fundamentally alters the access to, and characteristics of, the detached regime. Historically, reaching the high-recycling regime in stellarators has been impeded by the complex 3D SOL structure. Achieving detachment in stellarator configurations critically depends on driving the plasma to sufficiently high densities. In typical W7-X island divertor experiments, the detachment sequence is initiated by continuously raising the plasma density via gas puffing. This density ramp drives a necessary increase in the radiated power fraction, which effectively mitigates the thermal heat loads on the divertor targets. Notably, full particle detachment, which is characterized by a rapid and substantial drop in the target particle flux, is only triggered later in the discharge, once the density and corresponding radiation reach a critical threshold [48].

Although full detachment has been successfully demonstrated in the W7-X island divertor [49], current experiments remain underpowered, presenting significant challenges for a viable extrapolation to reactor-relevant conditions. Essential divertor functions, specifically efficient particle exhaust and robust radiative power dissipation, scale strongly with the local divertor density. Because the inherent 3D SOL structure hinders the high-recycling regime, the downstream divertor densities obtained thus far in W7-X are significantly lower than those typically observed in comparable tokamak discharges. Consequently, facilitating a strong, localized density build-up in the divertor region is of paramount importance for accessing, sustaining, and scaling the highly desirable detached regime within the island divertor concept.

1.5 Stellarator present and future perspectives

Tokamaks initially led and still are the main focus of magnetic confinement fusion (MCF) research [10]. However, because stellarators break the continuous 2D toroidal symmetry of tokamaks, their fully 3D magnetic geometry provides a vastly larger number of free parameters for designing the plasma boundary and the shapes of the external magnetic coils. This immense design flexibility could theoretically lead to an optimized configuration with distinct operational advantages—specifically, the ability to operate in a steady state without requiring an inductively driven plasma current, thereby eliminating the risk of major current-driven disruptions.

Despite this theoretical promise, early, unoptimized classical stellarator designs suffered from severe confinement degradation [50]. The fundamental issue was excessive neoclassical transport driven by particles becoming trapped in the localized

ripples of the 3D magnetic field. This lack of optimization led to unacceptable thermal energy losses [51], the rapid radial drift and loss of energetic fast ions before they could transfer their heat to the bulk plasma, and an inward radial electric field that caused highly charged impurities to dangerously accumulate in the plasma core [52]. Furthermore, during the early decades of fusion research, there was insufficient computational power to adequately explore the massive 3D configuration space to find the exact magnetic geometries required to overcome these inherent transport issues [53].

In the last three decades, devices like Wendelstein 7-X (W7X) were successfully designed and built. W7-X proved that it was possible to minimize neoclassical transport losses in a stellarator device [54], and demonstrated high-performance plasma operation in stellarators [55]. Despite this, stellarators are roughly a generations behind its tokamak counterpart and still face some challenges that will need to be resolved [56]:

- Confinement of fusion-born helium particles [57]; even in highly optimized configurations such as Wendelstein 7-X, approximately 5% of alpha particles are lost, leading to localized overloading of the plasma-facing components (PFCs).
- Particle and Energy exhaust: At the plasma boundary, the hot plasma unavoidably interacts with the Plasma Facing Components (PFCs). If left unmitigated, this interaction is mutually detrimental to both the confinement and the machine's structural integrity. High unmitigated particle and heat fluxes can easily exceed the thermal and material limits of the PFCs, causing severe localized melting, sputtering, and macroscopic erosion. Conversely, this wall erosion releases high-Z (high atomic number) solid impurities into the plasma. If these heavy ions penetrate the hot plasma core, they cause massive energy dissipation through radiative cooling (such as bremsstrahlung and line radiation), which drastically reduces fusion performance.
- Particle transport: At the high densities required for optimal fusion performance, stellarators frequently exhibit a strong inward accumulation of impurities, which can ultimately lead to radiative collapse. As predicted by neoclassical theory, this behavior arises because, in the absence of continuous magnetic symmetry and at low collisionalities, a strong inward-pointing radial electric field must develop to maintain ambipolar particle fluxes. This negative electric field drives highly charged impurity ions directly into the plasma core, causing them to accumulate [52].
- Divertor feasibility; it is still not understood whether all the requirements of a divertor (guarantee of plasma confinement, acceptable heat flux, sufficient neutral pressure for pumping out helium ash, impurity control for core integrity) can simultaneously be met in a reactor-relevant stellarator. Several divertor

concepts are being considered, including the helical divertor in LHD [42], the island divertor in W7-X [40], and a general 'non-resonant' (non-island) divertor [58].

Ongoing experimental and theoretical efforts are now focused on improving stellarator performance and resolving remaining limitations, with the aim of establishing their competitiveness for reactor applications [59]. Progress in these areas will be decisive in determining the role of stellarators in future fusion power plants and in guiding the design of next-generation devices.

1.6 Thesis Outline

This thesis focuses on the challenge of power and particle exhaust in stellarators, specifically on the island divertor concept. Because a comprehensive understanding of the complex 3D magnetic topology and the associated SOL physics is required first, the formal motivation and objectives of this work will be detailed at the end of Chapter 2.

The outline of this work is as follows: in Chapter 2 an introduction to the concepts of Scrape-off Layer (SOL) physics, 3D magnetic topologies, and the principles of the island divertor is given. This chapter also details the computational tools used for the simulations. Chapter 3 shows the results of the simulations performed in this thesis and discusses them. Chapter 4 introduces a deeper analysis of some of the relevant physics identified in the data. Finally, Chapter 5 summarizes and concludes the work, suggesting possible directions for future research.

Chapter 2

Scrape Off Layer Physics (SOL) and Modelling Tools

As this thesis is focused on analyzing the performance of the island divertor, the next sections will focus on the formation of magnetic islands in stellarators on resonant surfaces, island divertor physics and the underlying design concepts as well as the computational tools used to explore the 3D geometry and physics.

2.1 Magnetic Field Line Hamiltonian

2.1.1 The Hamiltonian formulation

The field lines of a magnetic field, $\mathbf{B}$, given its divergence free property, $\nabla \cdot \mathbf{B} = 0$, are trajectories of a Hamiltonian system [60]. The Hamiltonian $H(q, p, t)$ for a given magnetic field $\mathbf{B}$ is the poloidal magnetic flux $\chi(\theta, \psi, \phi)$; where the poloidal angle θ is the canonical position, the toroidal magnetic flux ψ is the canonical momentum and the toroidal angle ϕ is time.

The vector potential, $\mathbf{A}$, can be expressed in the (r, θ, ϕ), where r labels toroidal nested surfaces, as

$$\mathbf{A}\left(r, \theta, \phi\right) = \psi\left(r, \theta, \phi\right) \nabla\theta - \chi\left(r, \theta, \phi\right) \nabla\phi \tag{2.1}$$

The magnetic field, defined by the curl of the vector potential, $\nabla \times \mathbf{A}$, can thus be described as

$$2\pi\mathbf{B} = \nabla\psi \times \nabla\theta + \nabla\phi \times \nabla\chi \tag{2.2}$$

Hamilton's equations for the field line trajectory can thus be expressed as

$$\frac{d\theta}{d\phi} = \frac{\partial\chi(\theta, \psi, \phi)}{\partial\psi}, \frac{d\psi}{d\phi} = \frac{\partial\chi(\theta, \psi, \phi)}{\partial\theta} \tag{2.3}$$

In the case of axisymmetry, χ does not depend explicitly on ϕ. Then, from Eq. 2.3 and Hamiltonian dynamics, it means that the Hamiltonian is autonomous and the canonical energy, χ, is a conserved quantity. These are defined as 1D

integrable Hamiltonians. This means that the solutions of the system can be found by evaluating integrals of known functions from a given set of initial conditions and only one constant of motion is required to guarantee integrability [61].

Thus, in this type of systems, field lines are confined to surfaces of constant χ and magnetic surfaces exist. In particular, being χ the Hamiltonian of the system, field line trajectories will lie on concentric tori, yielding nested flux surfaces. Axisymmetric devices like tokamaks do guarantee, from a field line flow point of view, confinement of charged particles.

2.1.2 KAM theory

In 3D devices, like stellarators, the Hamiltonian system becomes non-autonomous, since $\frac{d\chi}{d\phi} \neq 0$. This is commonly referred as a 1.5D Hamiltonian [62]. This means that integrability is no longer guaranteed in these systems and thus also confinement on flux surfaces. If a system is not integrable, some trajectories of the Hamiltonian are ergodic, meaning they may eventually fill out a finite volume of phase space rather than being confined to surfaces.

However, the results of Kolmogorov [63], Arnold [64] and Moser [65], also known as KAM theorem, proved that a 1.5D Hamiltonian can be described as nearly integrable if it is obtained by applying a non-axisymmetric perturbation series about an autonomous integrable Hamiltonian H_0 [66], given that the perturbation parameter $\epsilon \ll 1$.

$$H\left(q,p,t\right) = H_0(p) + \sum_{i=1}^{\infty} \epsilon^i H_i\left(q,p,t\right) \tag{2.4}$$

The KAM theorem implies that for a non-autonomous Hamiltonian sufficiently close to integrability, the resulting non-axisymmetric magnetic field has flux surfaces that occupy a non-zero volume in phase space. As the perturbation from integrability, ϵ increases, these invariant surfaces may break up and form magnetic islands where $\iota = \frac{n}{m} \in \mathbb{Q}$, remembering that n is the toroidal mode number and m the poloidal mode number. This important fact shows that also non-axisymmetric 3D magnetic geometries, such as stellarators, can confine charged particles; at least from the magnetic field line flow point of view.

2.2 The Island Divertor

2.2.1 Magnetic islands in stellarators

In Section 2.1, it has been shown how 3D magnetic geometries provide the possibility for magnetic island formation in the neighborhood of rational surfaces, $\iota = \frac{n}{m}$, as the non-axisymmetric magnetic perturbation increases. These islands usually form chains that wind helically around the main plasma core region of stellarator devices like W7-X, Fig. 2.1.

An island is defined by its radial width, r_i, and its poloidal width, the ratio of which establishes the island's aspect ratio. The island O-point is the local magnetic axis, while the two X-points divides the island from the others. An individual island in a chain is bounded by a separatrix, the flux surface contour that connects one X-point to the other. The fieldlines inside the island rotate around the O-point due to a internal field-line pitch Θ, which is the the internal rotational transform of the island. The formation, size, and topology of these islands are primarily governed by two factors: the local magnetic shear, $\iota' = \frac{d\iota}{dr}\Big|_{r_a}$, which describes the radial gradient of the rotational transform at the location of the resonant surface, r_a, and the amplitude of the resonant magnetic perturbation field, b_{rm}, applied at that specific rational surface. These two parameters determine the island radial width, r_i, and the field line pitch Θ. r_i can be described as [68]:

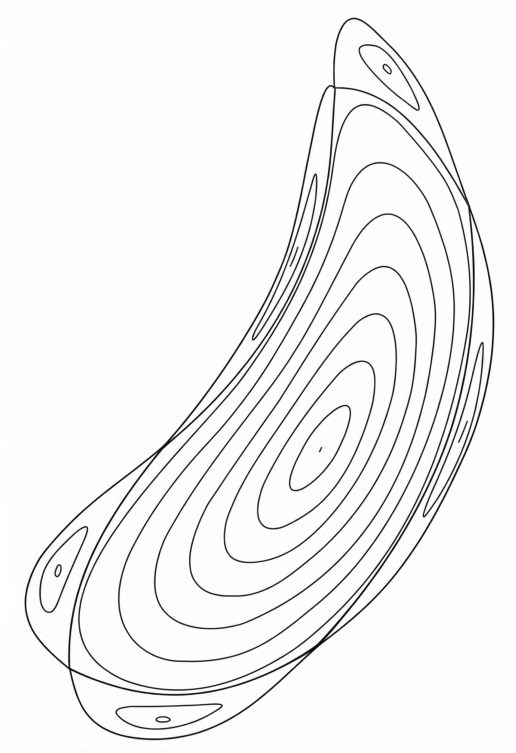

Figure 2.1: Magnetic bean-shaped cross-section of W7-X, adapted from [67]. The five-island chain surrounding the core is clearly visible, showcasing the typical island geometry.

$$r_i = 2\sqrt{\frac{Rb_{rm}}{\iota' m}} \tag{2.5}$$

Where R is the torus major radius. Θ can be described as [68]:

$$\Theta = 2a\sqrt{\frac{\iota' b_{rm}}{Rm}} \tag{2.6}$$

Where a is the torus minor radius. As it will be seen in Section 2.2.2, r_i and Θ significantly affect transport in the island. Usually, b_{rm} is used to increase island size, $r_i \propto b_{rm}$, and field line pitch, $\Theta \propto b_{rm}$ [69]. However, the perturbation field consists of a broad spectrum of different b_{rm}. This broadband magnetic spectrum simultaneously excites multiple discrete resonances at various rational surfaces across the plasma edge. When different neighboring resonances are excited, the resulting islands overlap and formation of chaos in the magnetic field occurs [70]. Extensive stochasticity degrades the well-defined, structured exhaust channels of the island divertor. It generates complex magnetic lobe structures [71] that allow escaping plasma to strike the PFC at unpredicted locations, creating unwanted and potentially damaging hot spots [72].

The Chirikov criterion [73] is used to assess the level of resonance-overlap for the loss of the last KAM surface and the subsequent stochastization of the magnetic field. In reality, the last KAM surface vanishes before this overlap, due to the nonlinearly produced secondary islands. However, the criterion still provides a good estimate of for stochastization.

$$\sigma_{CHIR} = \left(\frac{r_{i,m_1,n_1} + r_{i,m_2,n_2}}{2\left|r_1 - r_2\right|} \right)^2 \geq 1 \tag{2.7}$$

Where r_{i,m_a,n_a} is the width of the island generated at the $a-th$ resonance and r_a the location of its center. Given Eq. 2.5, we note that $r_{i,m,n} \propto \frac{1}{\sqrt{\iota'}}$. In addition to that, by expanding the rotational transform at the center of the island, one gets [68]:

$$\iota\left(r\right) = \frac{n}{m} + \iota'\big|_{r_a}\left(r - r_a\right) \tag{2.8}$$

Which leads to $r_a \propto \frac{1}{\iota'}$, thus making the Chirikov parameter dependant on magnetic shear [74]:

$$\sigma_{CHIR} \propto \left(\frac{\iota'}{\sqrt{\iota'}} \right)^2 = \iota' \tag{2.9}$$

This means that for low shear devices, different resonant islands are further apart. Additionally, the onset of stochasticity occurs at a higher perturbation amplitude for low shear devices, which allows larger islands, i.e. larger internal field line pitch, before the field becomes chaotic.

In fact, in low shear stellarator devices, such as the Wendelstein-7AS (W7-AS) and Wendelstein-7X (W7-X), it is possible to have a large intrinsic single magnetic island chain. Typically, the lowest-order resonance islands are the largest and appear at the edge of the plasma volume. These islands are bounded by a separatrix that divides them from the core region, Fig. 2.1.

From Eq. 2.5, The Chirikov parameter poses a limit also on the radial amplitude of each perturbation, $\sigma_{CHIR} \propto b_{rm_1} + b_{rm_2}$. For a given magnetic spectrum, this imposes a upper limit on the b_{rm} of the resonant surface utilized for the divertor. Furthermore, by substituting Eq. 2.6 in Eq. 2.5, the Chirikov parameter returns $\sigma_{CHIR} \propto \Theta^2$. For a given spectral cleanliness and local magnetic shear, achieving a sufficiently high internal pitch for efficient power exhaust, without violating the stochastic limit, requires a delicate optimization of these parameters.

Magnetic islands are ideal for the exhaust concept of the island divertor. To form the divertor, they are intersected with toroidally segmented targets, Fig. 2.6, that cut open their field lines, creating a SOL and setting up a divertor volume in a stellarator. The divertor plate is discontinuous for technical reasons explained in Section 2.2.5 and follows the magnetic island toroidally. The concept of the island divertor has also been applied to high shear stellarators, such as LHD [75], even though edge islands are generated by field perturbation coils.

2.2.2 SOL plasma physics

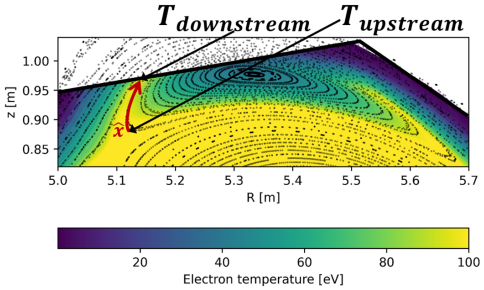

Figure 2.2: 2D electron temperature distribution in the island divertor of W7-X and binormal direction. Figure taken from [76].

The physics of the island divertor SOL involves a complex interplay of competing transport mechanisms. Functionally, it shares the primary objective of the tokamak poloidal divertor: utilizing a magnetic separatrix to decouple the confined plasma core from the vessel wall and channel exhaust fluxes to localized target plates. The magnetic islands forming the boundary of a stellarator are topologically closed, nested flux tubes. these islands must be intersected by solid target plates; this geometric intersection generates the open field lines that define the SOL. The open field-lines inside the islands guide the power and particles entering the islands across the island inner separatrix (last closed flux surface) towards the targets positioned at the island outer separatrix [29]. The islands form an intermediate SOL between the confined core and the plasma–surface interaction region, spatially separating the core plasma from a direct exposure to the recycling neutrals and the sputtered impurities. Large differences in the respective magnetic and divertor geometries exist between tokamaks and stellarators, including three-dimensional (3D) effects [77], which influence the plasma, neutral and impurity transport in the SOL.

A general overview of SOL physics is given, before diving into the specific models developed to study specifically the island divertor. In the SOL, the transport of energy and particles along the magnetic field lines is governed by the Braginskii [78] fluid equations. The parallel heat flux is described as a combination of conductive and convective channels for both electrons and ions. The electron parallel heat flux, $q_{\parallel,e}$, is often dominated by thermal conduction due to the high thermal conductivity of electrons, $\kappa_{0,e}$. Conversely, the ion heat flux, $q_{\parallel,i}$, is primarily convective, as the ion thermal conductivity is significantly lower ($\kappa_{0,e} \gg \kappa_{0,i}$) and the flow velocities satisfy $u_e \approx u_i$ due to the ambipolarity of the flux. The heat fluxes are expressed as [28]:

$$q_{\parallel,e} = \frac{5}{2} T_e n_e u_e - \kappa_{0,e} T_e^{\frac{5}{2}} \frac{dT_e}{ds} \tag{2.10}$$

$$q_{\parallel,i} = \left(\frac{1}{2} m_i u_i^2 + \frac{5}{2} T_i \right) n_i u_i - \kappa_{0,i} T_i^{\frac{5}{2}} \frac{dT_i}{ds} \tag{2.11}$$

where s is the coordinate along the field line, and kinetic energy is included for ions but neglected for the electron mean flow due to the mass ratio $m_i/m_e \gg 1$.

The SOL is characterized by two types of transport: rapid parallel transport along

field lines and slower perpendicular cross-field transport. Cross-field perpendicular transport becomes a leading-order physics effect within the SOL when the ∥-transport time to travel along the field lines becomes comparable to the ⊥-transport time required to bridge the poloidal displacement of this fieldline after one toroidal revolution [77]. Locally the ratio of perpendicular to parallel transport is set by the field line pitch Θ, which measures the poloidal displacement for displacement along the fieldline.

Power enters the SOL at last closed flux surface (upstream region). From there, it travels along the field line toward the material targets (downstream region). The distance a particle travels along a magnetic field line from the upstream to downstream point is defined as connection length L_c, Fig. 2.9. The connection length is related to the pitch as $L_c \propto \frac{1}{\Theta}$. At equal device geometry, the lower the pitch, the higher the connection length and hence the more perpendicular transport will become comparable to parallel transport. In low shear stellarators magnetic islands, the field line pitch is approximately $\Theta \approx 0.001$ [79]. This creates very long connection lengths in the island divertor SOL, thus making ⊥ transport comparable to ∥ transport.

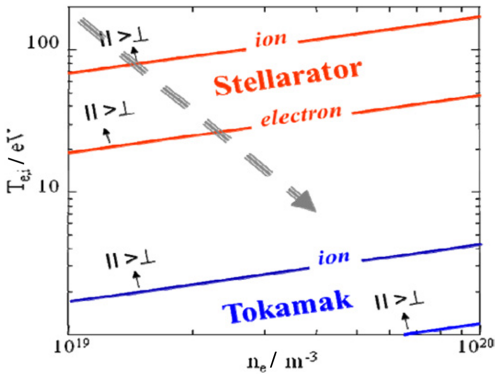

Figure 2.3: Ratio of ∥ to ⊥ conductive heat fluxes of ions and electrons in typical SOL parameter ranges for stellarators and tokamaks. The dashed arrow indicates a typical path of SOL plasma with increasing n_e. Figure taken from [29].

The competition between these transport channels can be formally quantified by evaluating the ratio of the effective parallel heat conduction (projected onto the transverse plane) to the perpendicular heat diffusion. Following the basic idea behind the Two-Point Model (TPM) for tokamaks [80, 34], a 1D energy transport model is made [29], taking into account ∥ and ⊥ transport. The structure of the magnetic island, characterized by an O-point and two X-points, is simplified and the equations are projected on the bi-normal direction x, Fig. 2.2, which is defined as the direction perpendicular to the toroidal direction and the perpendicular to flux surface direction. This implicitly assumes toroidal symmetry at the target and a correspondence of bi-normal and parallel transport across different field lines. A spatially constant field-line pitch in the island SOL is also assumed.

$$\Theta \frac{d}{dx}\left(-\kappa_{e,i} T_{e,i}^{5/2} \Theta \frac{dT_{e,i}}{dx}\right) + \frac{d}{dx}\left(-\chi_{e,i} n \frac{dT_{e,i}}{dx}\right) = 0 \tag{2.12}$$

The ratio of the parallel to the perpendicular conductive heat flux is then given by:

$$\frac{q_{\parallel,e,i}}{q_{\perp,e,i}} = \frac{\kappa_{e,i} T_{e,i}^{5/2} \Theta^2}{\chi_{e,i} n} \tag{2.13}$$

The ratio of parallel to perpendicular transport in the island SOL scales as $\sim \Theta^2$. In tokamaks, $\Theta \approx 0.1$ and in most of the SOL parameter domain, $\| \ / \ \perp \gg 1$ holds in tokamaks, especially for electrons, Fig. 2.3. On the other hand, in stellarators SOL $\Theta \approx 0.001$ and perpendicular and parallel transport are much more comparable. By setting the transport ratio in Equation 2.13 to unity, we can define a critical threshold temperature, T_{diff}, at which the perpendicular cross-field diffusion overtakes parallel conduction ($q_\perp \geq q_\parallel$). When the plasma temperature drops below this T_{diff} threshold, the SOL transitions into a fundamentally diffusion-dominated regime, which will be detailed in Section 2.2.3.

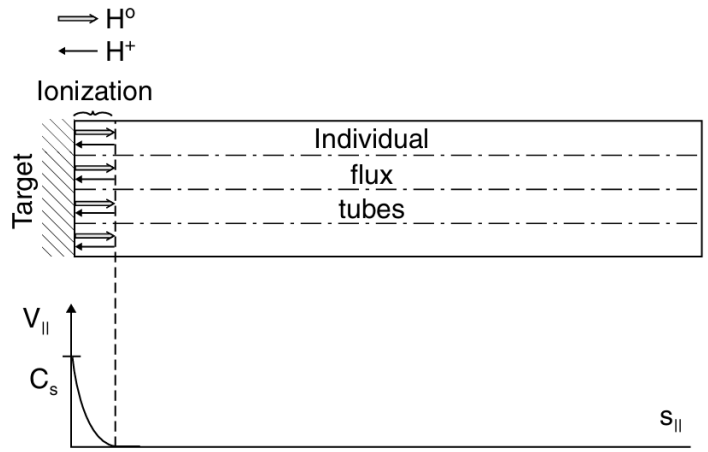

Figure 2.4: Sketch of the conceptually simplest SOL situation, where the neutrals recycling from each element of target surface are entirely ionized within the flux tube terminated by that element. Consequently, particle balance occurs for each flux tube individually. The ionization region is assumed to exist very near the target, resulting in a stagnant plasma over most of the length of the SOL. Figure taken from [28].

While the energy equations describe the temperature profile, the local plasma density is fundamentally governed by particle transport and parallel momentum conservation. In the basic TPM, particle balance assumes that recycling neutrals are ionized in a highly localized, thin layer immediately in front of the target. Consequently, parallel plasma flow is negligible throughout the bulk of the SOL, accelerating from zero to the sound speed only within this narrow ionization zone.

In the absence of volumetric momentum sinks such as friction or viscosity, parallel momentum conservation dictates that the total pressure along a flux tube remains constant: $p + nm_i v^2 = \text{constant}$. Assuming equilibrated temperatures ($T_e = T_i = T$), the static plasma pressure is $p = 2nkT$. Upstream of the ionization zone, the flow velocity is effectively zero, making the total pressure purely static ($2n_u kT_u$). At the target, the flow reaches the sound speed ($v_t = c_{st}$), and the dynamic pressure equals the static pressure, resulting in a total pressure of $4n_t kT_t$. Equating these upstream and target states yields the strict pressure balance relation:

$$n_u T_u = 2n_t T_t \tag{2.14}$$

This momentum conservation fundamentally couples energy and particle transport along the field line. A parallel temperature gradient, established by finite heat conductivity and energy losses, necessitates a corresponding inverse density gradient. As the temperature decreases along the flux tube toward the target, the plasma density must increase proportionately to conserve momentum. Therefore, within this pressure-conserved framework, describing the heat transport across the SOL inherently defines the characteristic density gradient in the region.

While standard 1D SOL models assume strict parallel momentum conservation, the complex magnetic topology of stellarator islands introduces significant momentum sinks. The substantial $\perp$ transport inherent to stellarator islands leads to modifications in the pressure equation, Eq. 2.14, as it will be explain in Section 2.2.3. Furthermore, for a vector quantity, such as momentum transport, the direction of the flow and the field line connection to the divertor plates is also important. When flow fields within adjacent flux tubes possess toroidally opposite streaming directions, they strongly interact due to the proximity of these counter-connecting field lines. Consequently, the plasma loses $\parallel$-momentum via dissipation driven by the $\perp$-viscosity operating across the tubes [81, 82]. In extended models, this dissipation is typically parameterized by a momentum loss factor ($f_{mom} \leq 1$), which reduces the total pressure achievable at the target.

At the plasma-wall interface, the quasi-neutrality of the bulk plasma breaks down. Because electrons have a much higher mobility than ions ($\propto \sqrt{m_i/m_e}$), they initially flow to the target surface at a much higher rate. To preserve the ambipolarity of the particle flux (where $\Gamma_e = \Gamma_i$), a potential drop in front of the target is formed. This results in the formation of a thin boundary layer known as the sheath, which has a characteristic width on the order of the Debye length, $\lambda_D = \sqrt{\varepsilon_0 T_e / e^2 n_e}$. Within this layer, the potential drop accelerates the ions towards the target.

For a stable sheath to form, the ions must enter the sheath region with a sufficiently high velocity. This requirement is known as the Bohm criterion [83], which states that the ion flow velocity at the sheath entrance, u_i, must exceed the local ion sound speed, c_s:

$$u_i \geq c_s \tag{2.15}$$

To achieve this velocity, ions are pre-accelerated in a quasi-neutral region known as the magnetic presheath, that is of dimension of the ion gyro radius, r_g.

The total power deposited onto the target is determined by the particle flux transmitted through the sheath and the power per particle. This is characterized by the sheath heat transmission factor, γ_{sh}. The heat flux density at the target, q_t, is given by:

$$q_t = \gamma_{sh} n_{e,t} c_s T_{e,t} \tag{2.16}$$

The coefficient typically takes a value of $\gamma_{sh} \approx 8$ [84] for hydrogenic plasmas.

This factor accounts for the thermal energy of electrons and ions, the acceleration of ions through the sheath potential, and the surface recombination energy released when ions neutralize at the wall.

2.2.3 Stellarator Two Point Model

The Stellarator Two Point Model (STPM) has been developed to study most of the island divertor physics [85, 86]. The STPM, while giving a useful model to understand part of the stellarator SOL physics, still has many limitations. Heat convection (parallel and binormal) is not included in the model. Momentum losses, while included, lack a proper scaling that aligns with experiment and/or modeling. A relation of the model quantities with the (radial) island size, r_i, is lacking. While the model includes an energy and momentum conservation equations, it lacks a particle conservation one. In its equations it does not include transport $\perp$ to the flux surface. This transport, which is observed to push power and particles from the power-carrying layer (PCL) (see Sec. 3.2.2 and Fig. 3.5) radially to the island O-point, must be artificially parameterized into the model's loss functions. Despite this, the STPM captures the role of cross-field transport compared to parallel transport and the loss of pressure conservation along the field line due to viscous dissipation in counter streaming flows.

In the tokamak TPM [80, 34], proposed mainly for tokamak SOLs, only parallel transport is considered and total pressure is conserved along the fieldline. However, due to the reasons mentioned above, the TPM needs to be expanded to correctly consider the island divertor physics. Under this constraints, the radial one-dimensional (1D) transport equations from energy and momentum read as:

$$\Theta \frac{d}{dx}\left(-\kappa_{e,i} T_{e,i}^{5/2} \Theta \frac{dT_{e,i}}{dx}\right) + \frac{d}{dx}\left(-\chi_{e,i} n \frac{dT_{e,i}}{dx}\right) = 0 \tag{2.17}$$

$$\Theta \frac{d}{dx}\left(n v_{i\parallel}^2 + \frac{p}{m_i}\right) = S_{mom} \tag{2.18}$$

$$q_\parallel = \gamma n_d c_{sd} T_d \tag{2.19}$$

In Eq. 2.17, the first term is the Spitzer-Harm [87] conduction projected on the bi-normal direction. The second term is the heat diffusion in the bi-normal direction. In Eq. 2.18 the first term is the projected total parallel pressure gradient, while S_m is a momentum loss parameter. Eq. 2.19 is the Bohm boundary condition. Integrating this system at the downstream and upstream location gives:

$$T_u^{7/2} = T_d^{7/2} + \frac{7 q_\parallel L_C}{2\kappa_e} - \frac{7\chi(n_u + n_d)}{4\kappa_e \Theta^2}(T_u - T_d) \tag{2.20}$$

$$p_u = 2 p_d \cdot (1 + f_m) \tag{2.21}$$

$$q_{\parallel} = \gamma n_d c_{sd} T_d \tag{2.22}$$

Perpendicular transport within the flux surface is taken into account in the STPM by the last term of Eq. 2.20. f_{mom} is a momentum loss factor, that takes into account the loss of pressure conservation along the fieldline.

2.2.3.1 Sheath limited regime

The sheath-limited regime occurs at low upstream densities and collisionalities, resulting in minimal neutral ionization (low recycling) within the divertor. In this state, particles and power primarily enter the SOL upstream via cross-field transport from the confined core. From this upstream stagnation point, the plasma flows downstream and accelerates to the local sound speed to satisfy the Bohm criterion at the target plate. Recycled neutrals are assumed to ionize mainly in the core.

Throughout this process, the SOL plasma remains essentially isothermal ($T_u \approx T_t$). Because the parallel temperature gradient is negligible, heat conduction becomes physically negligible to the overall power balance, leaving energy exhaust dominated by parallel convection. Consequently, the heat flux through the SOL to the target is limited solely by the ability of the sheath to transmit power, Eq. 2.16.

2.2.3.2 Conduction limited regime

As the upstream density increases, collisionality increases and the neutrals are retained inside the divertor. Ionization of the recycling neutrals in the divertor becomes the dominant particle source. Because recycling neutrals are ionized locally downstream, the parallel particle flux and convective heat transport are concentrated near the target plates.The heat transport in the rest of the SOL changes from convective to conductive dominated. A significant temperature gradient develops along the field line to drive the necessary heat flux and target temperatures of $\approx 10\,eV$ can be reached. The dominant term in the right hand side of the energy equation is $T_u^{7/2} \approx \frac{7 q_{\parallel} L_C}{2\kappa_e}$. The upstream temperature is relatively insensitive to external change and remains more or less constant.

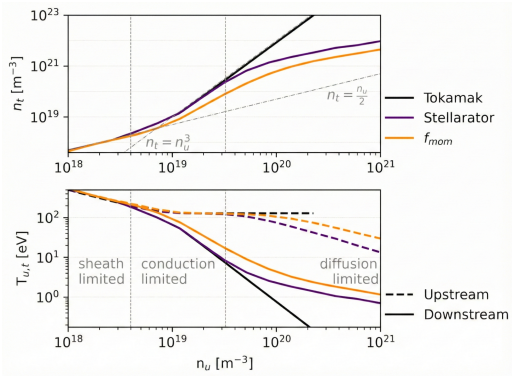

Figure 2.5: Comparison between the tokamak TPM, the STPM and the STPM with f_{mom}. The different regimes are highlighted. Figure taken from [76].

The ionization of the recycling neutrals in the divertor is the dominant particle source in the SOL and would yield very high densities at the target, $n_t \propto n_u^3$. At even higher densities cross-field diffusive transport and additional volumetric effects due to plasma-neutral and plasma-impurity interactions become significant. However, the presence of convection, f_{conv}, momentum losses, f_{mom}, and the bi-normal transport

hinders density buildup in the conduction limited regime of the island divertor, with $n_u < n_t < n_u^3$.

2.2.3.3 Diffusion limited regime

As the divertor density increases to a threshold, cross-field transport starts to dominate particle and power transport across the SOL. The dominant term in the right hand side of the energy equation is $T_u^{7/2} \approx \frac{7\chi(n_u+n_d)}{4\kappa_e\Theta^2}(T_u - T_d)$. Bi-normal transport is dominant and the drop in target temperature T_d becomes less steep and T_u starts to decrease. This drop in upstream temperature directly implies a saturation of the upstream plasma pressure, which fundamentally degrades confinement performance inside the separatrix.

Because the target pressure ($p_t \propto n_t T_t$) is fixed by the sheath heat flux, the reduced temperature drop of T_t limits the increase of density at the target, n_t. Cross-field transport hinders density build-up, described as the n_t obtainable for a given n_u. This is denominated diffusion limited regime [76].

In a tokamak poloidal divertor, since $\Theta_{tokamak} \approx 100\Theta_{stellarator}$ and counter-streaming flows are negligible, the SOL plasma usually shows a strong conduction limited regime, denoted "high recycling", with $n_t \propto n_u^3$ and $T_t \propto n_u^{-2}$. It also shows no diffusion limited regime at relevant plasma parameters.

2.2.4 Consequences on divertor performance and Role of geometric parameters

Due to the observed transition to diffusion limited regime at relevant plasma parameters, Fig. 2.5, divertor density build-up is hindered in stellarators. The direct transition, observed in tokamaks [88], from the high recycling regime to detachment is not attainable in stellarator divertors. Achieving a steep increase in target density, n_d, alongside a substantial drop in target temperature, T_d, is a fundamental requirement for optimal divertor performance and the transition to the detached regime. In particular, radiative power dissipation is strongly driven by density build-up, as volumetric radiation scales with the square of the density $P_{rad} \propto n_d^2$ [89]. A high-density environment is essential to retain recycled and sputtered neutral particles near the plasma-facing components, allowing low-Z impurities to effectively radiate away heating power and screen the core plasma [68]. Impurity retention depends on build-up via the drag force, $F_D \propto n_d$.

Additionally, high neutral compression in the divertor is essential for a fusion reactor to efficiently pump out helium ash and prevent core dilution [90]. Neutral compression is defined as the ratio of divertor and main chamber neutral pressures, $c = \frac{p_{n,div}}{p_{n,chamber}}$. The island divertor of W7-X currently yields compression ratios approximately two orders of magnitude lower, $p_{n,div} = 0.18\ Pa$ [91], than the ones required for ITER, $p_{n,div} = 10\ Pa$ [35]. Neutral pressure at the divertor also depends on density build-up via the recycling flux, $\Gamma_{rec} \propto n_d$.

Finely tuning the magnetic island geometric parameters has turned out to have a strong impact on island divertor transport. Increasing the internal island field line pitch, Θ, has been observed to significantly improve both the radiation pattern and detachment performance [92]. Similarly, expanding the island width (r_i) enhances the divertor's ability to screen neutrals and maintain stable detachment [68]. In Wendelstein 7-X, control coils [69] are utilized to tune Θ primarily by modifying the resonant radial magnetic perturbation, b_{rm}, a process that inherently alters the island size simultaneously: $\Theta \propto \sqrt{b_{rm}\iota'}$, $r_i \propto \sqrt{b_{rm}/\iota'}$. Understanding the specific role of each of these geometric parameters is a central point of this thesis.

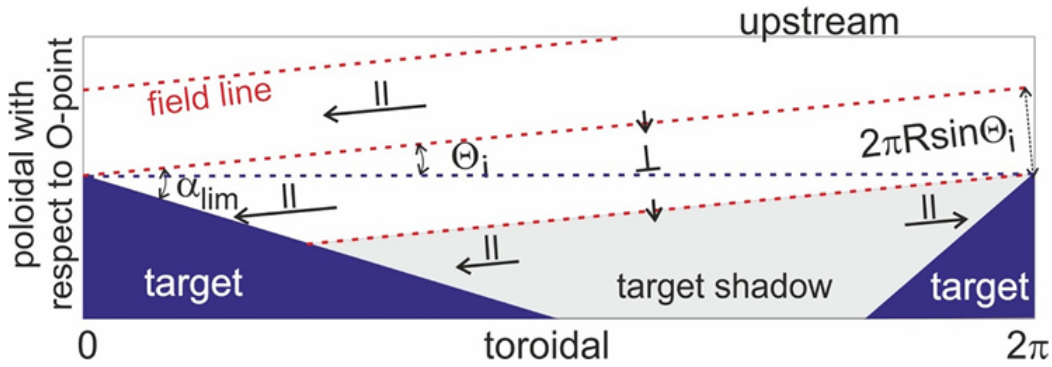

Figure 2.6: Sketch of a portion of an island surface in a island divertor. Figure taken from [68].

2.2.5 Target Shadow Region

Compared to tokamaks an additional phenomenon intrinsic to the island divertor is the appearance of an additional topological region in the SOL, the target shadow region (TSR). To meet the engineering requirement for target alignment the magnetic field incidence angle to the target surface is limited to about 1-3 degrees [93]. As a consequence of the low field line pitch in the island divertor, the continuous target plate must be toroidally inclined . This leads to segmented targets with fieldlines that are 'trapped' between them, that is, shadowed from the main SOL by the target, see Fig. 2.6. Because of the field line pitch of the island, Θ, the plasma is able to reach via $\parallel$ transport only the top part of the inclined target, with width $2\pi R \sin\Theta$ [68]. The rest of the target will be inaccessible for the plasma travelling parallel along field lines. This region, called the Target Shadow Region (TSR), is only accessible via cross-field transport, see Fig. 2.9. It is important to note that, for a given configuration, the size of the shadowed portion of the island, Fig. 3.6 and, consequently, the surface of the target plate that is not wetted by the plasma because of the TSR, Fig. 3.20, increase with decreasing Θ.

Within the TSR, the magnetic field lines are typically characterized by two distinct length scales. The first is the total toroidal circumference of the machine, scaling as $2\pi R$ (approximately 35 m in W7-X) [68]. The second is the effective target-to-target connection length, which is determined by the discrete toroidal placement of the

divertor modules. In W7-X, this physical strike-to-strike distance is typically around $\frac{2}{5}2\pi R$, though the exact value varies depending on the chosen magnetic configuration and the resulting strike line locations, Section **??**. Because of these extended parallel connection lengths, the TSR acts as a significant additional momentum sink for the boundary plasma. The shape and placement of the target plates can affect the TSR, the area of the target wetted by the plasma and the resulting heat flux on the plates.

2.3 Edge Plasma Modelling: EMC3-EIRENE

Computational edge plasma models have been developed in order to understand the underlying processes in the plasma edge, in order to understand and design power exhaust machines.

The magnetic structure and the discontinuous target plates in stellarators introduce a three-dimensional plasma boundary. This implies that 3D effects of plasma, neutral and impurity transport have to be taken into account by fully 3D, self-consistent transport codes. In the present thesis, for the modeling of 3D Scrape-Off Layers (SOL) and complex magnetic topologies, the EMC3-EIRENE code will be used. The code package is a coupled system comprising two Monte Carlo modules: EMC3 (Edge Monte Carlo 3D) for the plasma, and EIRENE, for neutral particles.

2.3.1 EMC3

EMC3 [94, 95] is a fully 3D self-consistent Monte Carlo code that applies a fluid model for the edge plasma based on Braginskii's equations [78] with free model parameters for anomalous cross-field tranport.

The Braginskii's equations are a system of two-fluid transport equations derived from the first three moments of the kinetic Boltzmann equation, that respectively give the conservation equations for particles, momentum and energy. The system is closed using the Chapman-Enskog expansion method [96], which assumes the plasma is in a regime of high collisionality $\frac{\lambda}{L} \ll 1$ and strong magnetization $\frac{\rho}{L} \ll 1$, where λ is the mean-free path, ρ is the Larmor radius and L is the characteristic length of the system. The model assumes quasi-neutrality for a simple plasma consisting of electrons and one single ion species, $n_e = n_i$. The impact of impurities is not included in this work.

In the code, the plasma transport is described by a simplifed time-independent version of the Braginskii's fluid equations [97]:

$$\nabla_\parallel \cdot (nV_\parallel) + \nabla_\perp \cdot (-D\nabla_\perp n) = S_p \tag{2.23}$$

$$\begin{aligned} &\nabla_\parallel \cdot (mnV_\parallel V_\parallel - \eta_\parallel \nabla_\parallel V_\parallel) \\ &+\nabla_\perp \cdot (-m_i V_\parallel D\nabla_\perp n - \eta_\perp \nabla_\perp V_\parallel) = -\nabla_\parallel P + S_m \end{aligned} \tag{2.24}$$

$$\begin{aligned}\nabla_{\parallel}\cdot\left(-\kappa_i\nabla_{\parallel}T_i+\frac{5}{2}nT_iV_{\parallel}\right)\\ +\nabla_{\perp}\cdot\left(-\chi_i n\nabla_{\perp}T_i-\frac{5}{2}T_iD\nabla_{\perp}n\right)=k(T_e-T_i)+S_{ei}\end{aligned}\tag{2.25}$$

$$\begin{aligned}\nabla_{\parallel}\cdot\left(-\kappa_e\nabla_{\parallel}T_e+\frac{5}{2}nT_eV_{\parallel}\right)\\ +\nabla_{\perp}\cdot\left(-\chi_e n\nabla_{\perp}T_e-\frac{5}{2}T_eD\nabla_{\perp}n\right)=-k(T_e-T_i)+S_{ee}\end{aligned}\tag{2.26}$$

where $p = n\,(T_i + T_e)$ and $\eta_{\perp} = m_i n D$. The signs $\parallel$ and $\perp$ denote the components parallel and perpendicular to the magnetic field. The parallel transport $\eta_{\parallel}$, κ_i, κ_e are considered to be classical, while the cross-B transports are usually assumed to be anomalous with D, χ_i and χ_e being determined from experiments. S_p and S_m are the ionization source and momentum loss via charge exchange with neutrals. S_{ee} and S_{ei} represent the energy loss or gain of electrons and ions due to the neutrals. All the volume sources due to neutrals are provided by the EIRENE code.

2.3.2 EIRENE

In the SOL and divertor regions, the mean free path of neutral particles (atoms & molecules) is often comparable to the system size, rendering the fluid approximation invalid.

Therefore, the EIRENE code [98] is employed to solve the stationary linear kinetic transport equation within a given host medium. EIRENE solves the integral form of this equation using Monte Carlo methods, simulating the trajectories of test particles in the 3D geometry and interpreting the transport as a Markovian jump process defined by a transition kernel decomposed into collision and transport parts. The code includes a comprehensive set of atomic and molecular processes, including electron-impact ionization and charge exchange. EIRENE calculates the source terms S_p, S_m, S_{ee}, S_{ei} on the RHS of the EMC3 fluid equations by integrating over the collision events.

$$\mathbf{v}\cdot\nabla f(\mathbf{r},\mathbf{v}) = \underbrace{-f(\mathbf{r},\mathbf{v})\Sigma_t\,|\mathbf{v}|}_{\text{Loss}} + \underbrace{Q(\mathbf{r},\mathbf{v})}_{\text{Primary Source}} + \underbrace{\int f(\mathbf{r},\mathbf{v}')C(\mathbf{r};\mathbf{v}'\to\mathbf{v})\,d\mathbf{v}'}_{\text{Scattering}}\tag{2.27}$$

Atomic and molecular data are taken from the AMJUEL [99], HYDEL [100] and ADAS [101] libraries.

2.3.3 EMC3-Eirene

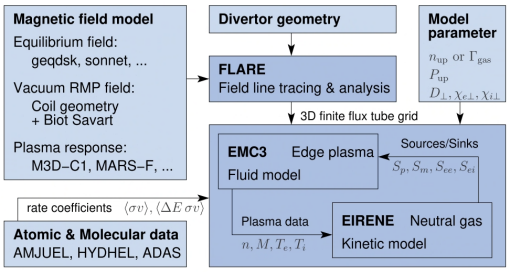

Figure 2.7: Workflow of the EMC3-EIRENE plasma edge model. Figure taken from [102].

To achieve a self-consistent steady-state solution, the code package employs an iterative coupling scheme. In this loop, EMC3 supplies the 3D plasma background profiles necessary for the EIRENE neutral transport simulation; conversely, EIRENE calculates and feeds back the resulting volumetric source terms for particle, momentum, and energy balances [102]. Computationally, this interaction relies on a computational mesh of 3D finite flux tubes, which must be generated in a pre-processing step (FLARE [103]), given the magnetic field model as input. This grid structure utilizes a generalized reversible field line mapping algorithm, enabling the rapid and accurate reconstruction of complex 3D magnetic field lines. Free parameters for cross-field transport $D_\perp$, $\chi_{e\perp}$ and $\chi_{i\perp}$ have to be provided.

2.4 HaGrids

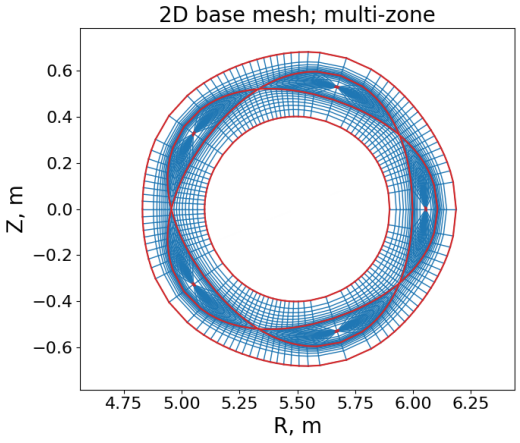

Figure 2.8: Multi-zone 2D base mesh. The inner, outer, O-point, and inter zone boundaries are highlighted in red [104].

Stellarator design deals with complex magnetic geometries, that show separatrix deformation, island rotation and deformation, ellipticity, magnetic flux compression/expansion and toroidally discontinuous targets. This makes studying the island divertor performance in general hard and computationally expensive. Understanding stellarator geometry like the one of W7-AS or W7-X requires the dissection of the convoluted effects.

In order to study the impact of single island geometry parameters on the performance of the island divertor, a novel code package, Hamiltonian Grids (HaGrids) has been developed [104]. It is able to construct a simplified geometry for the island divertor, which does not correspond to a real MHD equilibrium but respects the divergence-freeness of the physical magnetic field, is axisymmetric, satisfies Ampere's law and conserves the fundamental island geometry.

HaGrids is based on the Hamiltonian formulation, Eq. 2.2, of the magnetic field to generate a synthetic model with circular flux surfaces and island structures generated on arbitrary resonances. The Hamiltonian of Eq. 2.2 and Eq. 2.3 is used

in the following form:

$$\chi(\psi,\theta,\phi) = \chi_0(\psi) + \chi_1(\psi)\cos\left[m_1\left(\theta - \iota_1^{res}\phi\right)\right] + \sum_{l=2}^{n_{pert}} \chi_l(\psi)\cos\left[m_l\left(\theta - \iota_l^{res}\phi\right)\right] \quad (2.28)$$

Where an unperturbed Hamiltonian $\chi(\psi,\theta,\phi) = \chi_0(\psi)$ generates nested flux surfaces characterized by the rotational transform $\iota(\psi) = d\chi_0/d\psi$. An arbitrary number of perturbations can be added to excite specific resonant surfaces and form different island chains. To form a magnetic island chain, one can introduce a perturbation $\chi_1(\psi)$ with poloidal number m_1. The rotational transform at the resonance then satisfies $\iota_1^{res} = n_1/m_1$. This allows for selecting the perturbation spectrum and generate island geometries with dedicate geometric properties without incurring in magnetic field chaos (MFC) and requiring detailed coil optimization/design. At present, HaGrids can only generate geometries with a circular cross section, Fig. 2.8. Since stellarator geometries typically exhibit a certain degree of ellipticity, it is highly desirable to implement elliptic magnetic geometries in the code package. In Appendix A, the magnetic calculations carried out in [104] for the circular geometry are extended to elliptical magnetic coordinates. This derivation should help in the implementation of elliptical grid geometries within the HaGrids code.

A crucial step in running EMC3-EIRENE simulations is the generation of a magnetic field-aligned computational grid. HaGrids is used in the first three of the five grid generation stages [103]: it constructs a 2D base poloidal mesh, Fig. 2.8, it determines the inner and outer boundaries and traces the field line segments from the base mesh across the toroidal domain. Field lines are traced by numerically integrating the Hamiltonian system. The results are then mapped to real space using a coordinate transformation. For the remaining steps respectively, in this work, the construction of divertor targets is handled by Python routines, Fig. 2.10, while the approximation of the divertor target geometry and grid finalization are performed using the FLARE framework [103].

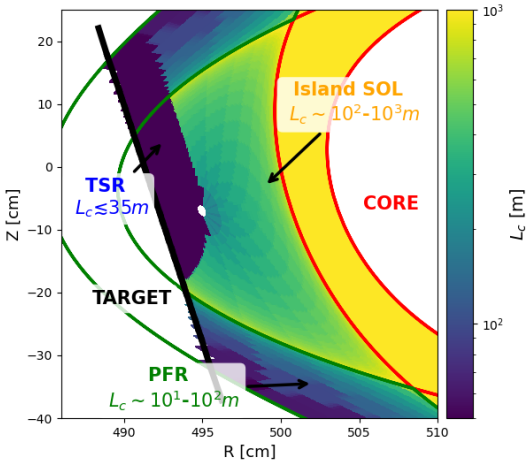

Figure 2.9: Connection length L_c distribution at $\phi = 8°$ in the region near the target of a simplified geometry configuration, highlighting the different topological regions and their characteristic L_c.

The 2D mesh is generated with a multi-zone approach [105], considering the core, private flux region (PFR) and single magnetic islands individually, Fig. 2.8. This allows better resolution of the island X-points and separatrix, reducing discretization error and Monte Carlo noise when considering parallel and perpendicular transport.

In Fig. 2.10 the resulting toroidal geometry of a $\iota^{res} = 5/5$ configuration obtained by using HaGrids and subsequently generating a target is shown. The 5/5 island chain helically rotates around the core torus. It can be observed how the simplified geometry retains the main topological regions of the island divertor, which are highlighted in Fig. 2.9. The finite target creates a TSR and the magnitude and distribution of L_c depend on the $\Theta \approx 0.001$ chosen. More details on the target and geometry used in these figures is given in Section 3.1.

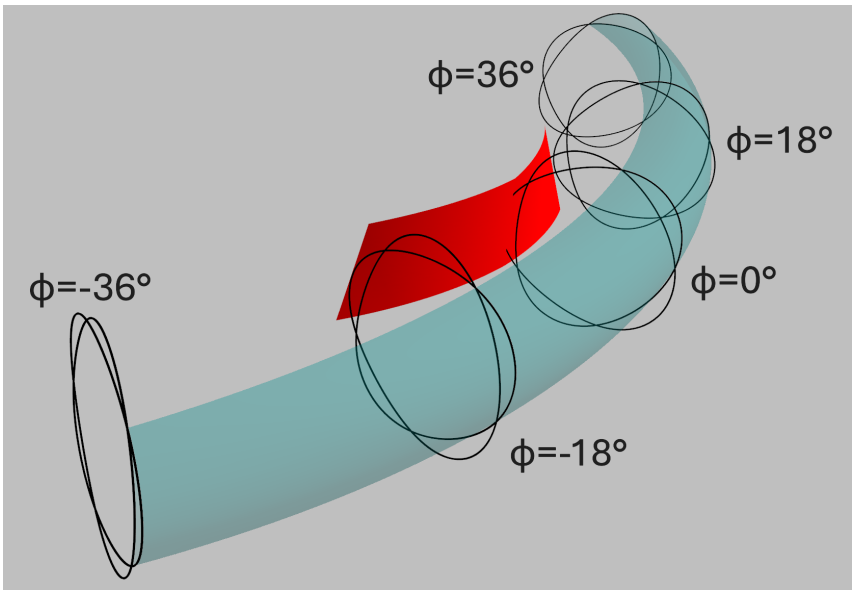

Figure 2.10: 3D sketch of the simplified geometry used in this thesis. A single island chain that helically rotates around the core region (blue) and a segmented target (red) that intercepts one island are highlighted.

2.5 Scope of the Thesis

The management of the strong particle and energy fluxes at the boundary of a confined fusion plasma remains a critical challenge towards commercial power plants, Sec. 1.3. To address this, the island divertor has emerged as a leading power exhaust solution in stellarators [106]. A divertor should be able to provide power dissipation, neutral particle exhaust, reduction of impurity production and impurity screening. While stable detachment has been successfully achieved in present day devices like Wendelstein 7-X (W7-X) [49], extrapolating these scenarios to a reactor-scale stellarator requires substantially higher divertor densities, which remains a primary operational challenge for current island divertors [86].

Many divertor capabilities such as particle exhaust or radiative power dissipation scale with downstream density, Sec. 2.2.4. However, the previous sections showed how diffusion limited regime limits the maximum obtainable downstream densities n_d in the island divertor, Sec. 2.2.3.3. Island geometric parameters, such as island width r_i, field line pitch Θ and target placement have been found to have a strong

impact on island divertor transport, although many of their effects have not been explored yet, Sec. 2.2.4 & 2.2.5. Studying the impact of each parameter in a 3D stellarator geometry like the one of W7-AS or W7-X requires the dissection of the many convoluted geometric effects, making it a complex and computationally expensive task. For the island divertor concept to become fully reactor-relevant and for performance improvement of present and future stellarators, these coupled geometric effects must be carefully disentangled.

Therefore, the central aim of this thesis is to isolate and investigate how these geometric parameters: Θ, r_i and target placement, singularly impact target density build-up, with the goal of collecting the individual physical effects for present and future divertor studies.

In this context, firstly, the HaGrids simplified magnetic geometry framework (Sec. 2.4) is exploited to generate, starting from a reference configuration made with the same characteristics of W7-X, multiple configurations with selected values of r_i and Θ. These configurations are then used to perform an extensive computational analysis using the fully 3D self-consistent edge plasma and neutral transport code EMC3-EIRENE (Sec. 2.3).

Secondly, the simplified geometry framework is used to also assess the impact of target placement on divertor performance. In the current W7-X 5/5 island chain there are three possible stellarator-symmetric target locations around the symmetry plane: inboard, top/bottom and outboard. These configurations are constructed and simulated using EMC3-EIRENE.

The structure of the thesis is a it follows: in Chapter 3, the simulations set-up criteria is explained step by step and the obtained results discussed both for the r_i, Θ scans (Sec. 3.2) and for the target placement scans (Sec. 3.3 & 3.3.1). In Chapter 4, the impact of r_i and Θ on transport is analyzed with the tools of the Stellarator Two Point model (STPM) (Sec. 4.1) and, for the first time, the predictive capabilities of a STPM Onion-Skin model (OSM) are tested on the simulations results of the r_i and Θ scans (Sec. 4.2). In the end, Chapter 5 summarizes the obtained results and concludes the work.

Chapter 3

Simulations and Results

3.1 Configuration Setup

3.1.1 Design Space

Using the code package HaGrids, different simplified magnetic configurations with different island characteristics are created and used for EMC3-EIRENE simulations. The starting geometry in this thesis is designed to approximate the W7-X geometry. The major radius is $R = 5.5\ m$, the minor radius $a \approx 0.5\ m$, the island width $w \approx 0.1\ m$ and a resonant surface at $\iota = \frac{n}{m} = \frac{5}{5}$. The geometry possesses thus a five fold symmetry.

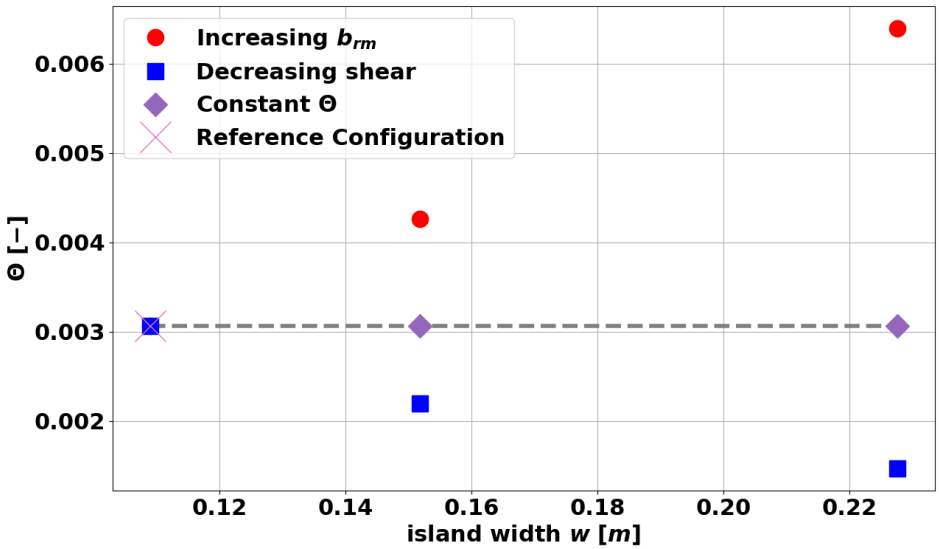

Figure 3.1: Points in the $r_i - \Theta$ design space from which the different magnetic configurations are created.

In HaGrids, the rotational transform is approximated using a quadratic radial profile:

$$\iota\,(r) = a_\iota \pi r^2 B_0 + b_\iota \tag{3.1}$$

Where a_ι, b_ι and the strength of the magnetic field at the center B_0 are input parameters in the code. The resulting island magnetic shear, $\frac{d\iota}{dr}\Big|_{r_a}$, can be changed by changing the parameter a_ι. The dependence between the two in the code is expressed by:

$$\iota' = 2\pi a B_0 a_\iota \tag{3.2}$$

In order to have a reference configuration that resembles W7-X standard configuration ι profile [107], Fig. 3.2, the input parameters are set to $b_\iota = 0.84557$ and $a_\iota = 0.065$.

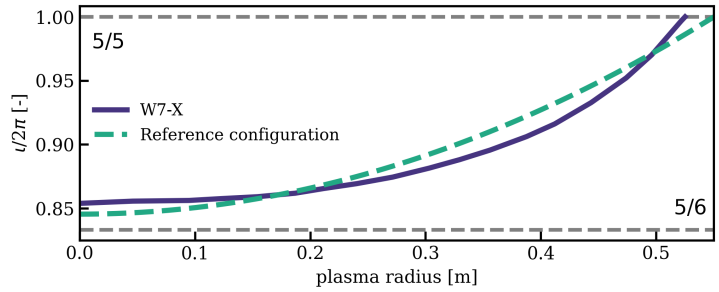

Figure 3.2: $\iota(r)$ radial profile for W7-X standard configuration (adapted from [107]) and the approximation used in HaGrid for the reference configuration.

In HaGrids, a perturbation of $\iota^{res} = n/m = 5/5$ is selected, the same of W7-X standard configuration. This excites the corresponding resonant surface, generating a five island chain in the neighborhood of $\iota(\psi) = 1$. In the case of this single perturbation, the Hamiltonian of Eq. 2.28 becomes:

$$\chi(\psi, \theta, \phi) = \chi_0(\psi) + \chi_1(\psi) \cos\left[m\left(\theta - \phi\right)\right] \tag{3.3}$$

A linear profile is used for the perturbation $\chi_1(\psi)$. Details can be found in [104]. In the code, $\chi_1(\psi)$ is proportional to the perturbation amplitude $\chi_1(\psi) \propto A_1$, with A_1 being an input parameter, expressed in $[Wb]$. In HaGrids, b_{rm} can be varied by changing the perturbation amplitude A_1. The relationship can be derived to be:

$$b_{rm} = \frac{A_1 m_1}{2\pi R a B_0} \tag{3.4}$$

A value of $A_1 = -0.0036\ Wb$ is chosen, so that an island width of $r_i \approx 10.9\ cm$ is obtained, see Fig. 3.5. The nominal island width in W7-X standard configuration, using a controlled control coil current $I_{cc} = 2.5\ kA$ is $w_{W7-X} \approx 10\ cm$ [92].

Starting from this reference geometry, other configurations are explored. This study focuses on a parametric scan on the island geometric parameters: magnetic island radius, r_i, and field line pitch, Θ. Given their relationship with ι' and b_{rm}, $r_i \propto \frac{b_{rm}}{\iota'}$ and $\Theta \propto b_{rm}\iota'$; it is possible to create different geometries in the design space, starting from the reference one, by only varying A_1, a_ι and b_ι in the code.

We aim to simulate configurations with three different island widths: $r_i \approx 10.9\,cm$, $r_i \approx 15.2\,cm$, $r_i \approx 22.8\,cm$. Starting from the reference case, with $r_i \approx 10.9\,cm$, it is possible to obtain the latter two island sizes in three different ways. Each way returns a different island configuration, while also always remaining below the low-shear limit. In the context of this thesis, this limit is defined as the interval where the entire rotational transform profile, $\iota(r)$ in Eq. 3.1, remains strictly bounded between the adjacent primary resonances, $\iota^{res} = 5/6$ and $\iota^{res} = 5/5$, Fig. 3.2 & 3.3. By achieving the same island size with the three different approaches, it is possible to also compare same-size island configurations that are otherwise very different in ι', b_{rm} and Θ.

Table 3.1: Summary of the magnetic configurations generated for the parametric scan. The Case ID indicates the perturbation flux amplitude A_1 (e.g., A36 = 3.6×10^{-3} Wb) and the shear parameter a_ι (e.g., a65 = 6.5×10^{-2}).

Case ID	b_{rm} [$\times 10^{-4}$]	ι' [$\frac{1}{m}$]	w [cm]	Θ [$\times 10^{-3}$]
Reference Configuration				
A36a65	3.79	0.562	10.9	3.06
Decreasing ι'				
A36a34	3.79	0.289	15.2	2.20
A36a15	3.79	0.129	22.8	1.46
Constant Θ				
A50a47	5.29	0.403	15.2	3.06
A75a31	7.92	0.269	22.8	3.06
Increasing b_{rm}				
A70a65	7.36	0.562	15.2	4.26
A157a65	16.54	0.562	22.8	6.40

To do so, starting from the reference case, one can either: a) only increase b_{rm}, thus increasing both Θ and r_i; b) only decrease ι', thus decreasing Θ while increasing r_i; c) increase b_{rm} and decrease ι' accordingly to keep Θ constant with varying r_i.

Once the desired r_i is set for each case, the choice of the parameters value is based on Eq. 3.2 and Eq. 3.4, paired with Eq. 2.6 and Eq. 2.5. In case a), we obtain b_{rm} value from Eq. 2.5 and the corresponding A_1 from Eq. 3.4. In case b), we obtain ι' from Eq. 2.5 and the corresponding a_ι from Eq. 3.2. In case c) a system of equations based on Eq. 2.5 and Eq. 2.6 is created, to obtain the respective b_{rm} and ι' values. Since Θ is the same of the reference configuration, it is possible to obtain the new b_{rm} from:

$$b_{rm} = \frac{m\Theta r_i}{4a} \tag{3.5}$$

And the corresponding ι' from:

$$\iota' = \left(\frac{2}{r_i}\right)^2 \frac{R b_{rm}}{m} \tag{3.6}$$

Then the corresponding A_1 and a_ι are obtained still from Eq. 3.2 and Eq. 3.4. In the end, we obtain points in the design space like Fig. 3.1. The method above, based mainly on the analytical relations obtained in [68], is a efficient method to obtain comparable magnetic configurations with different characteristics. The

values expected from analytical relations are successfully obtained in the resulting magnetic geometries, where island widths and field line pitch are found to be as expected, see Figs. 3.5 & 3.6. In Fig. 3.5 the three island sizes obtained for this work are shown. Three different kinds each of the $r_i \approx 15.2\ cm$ and $r_i \approx 22.8\ cm$ geometries are obtained, each with a different value of Θ. Because of this, even between configurations with the same island size, there are differences in terms of divertor transport due to geometric effects, Fig. 3.6.

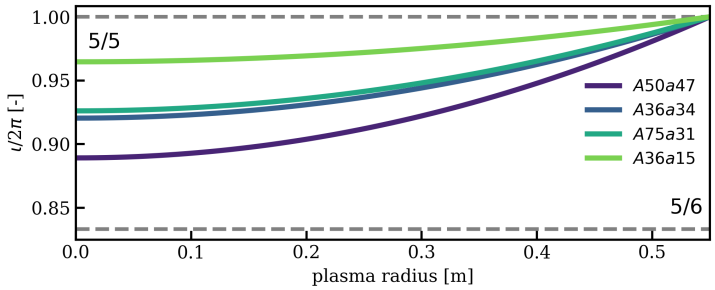

Figure 3.3: $\iota(r)$ radial profile for the other four configurations created in this work. The remaining A70a65 and A157a65 have the same $\iota(r)$ profile of the reference configuration.

3.1.2 Grid and Target generation

The grids are generated exploiting the five-fold symmetry of the magnetic geometry. The computational domain used is one fifth of the full torus, $\phi \in [0°, 72°]$. The total toroidal resolution is of 101 cells. Grid refinement is performed for both the radial and poloidal direction, while the toroidal grid is uniform. Radially, the core, islands and PFR grids are finer towards the separatrix 3.5. Poloidally, the grid is finer towards the X-points. The five magnetic islands are the regions with higher radial and poloidal refinement out of the seven zones, with 10^5 cells per island per toroidal slice.

One discontinuous target per island is created. The target plates are placed at the inboard location of the island in the symmetry plane. The target, Fig. 2.10, reaches the point of radial deepest penetration into the island at $\phi = 0°$. Here it is positioned slightly above the

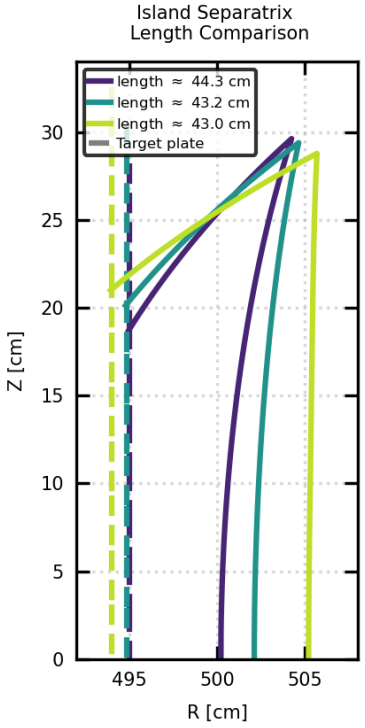

Figure 3.4: Separatrices poloidal length displayed for the three island sizes used in this work.

island O-point to prevent a confined region inside the island. From there the target plate moves radially away from the magnetic axis, while helically following the main island chain. With the current magnetic field incidence angle of $\approx 3°$, the target extends toroidally to $\phi < 36°$ to cover the full island domain and end in the PFR. This ensures that the target intercepts the majority of the power leaving the confined region, with power deposition beyond the target remaining negligible. The target is designed such that it casts a shadow onto itself after one full toroidal turn. The second target plate retraces this path symmetrically in the second half of the computational domain, on a different magnetic island with respect to the first, starting outside the island somewhere in the second half of the computational domain $\phi > 36°$ and reaching its point of deepest penetration at $\phi = 72°$. Because of the domain symmetry, each island will have a single resulting target entering and exiting the island, Fig. 2.10.

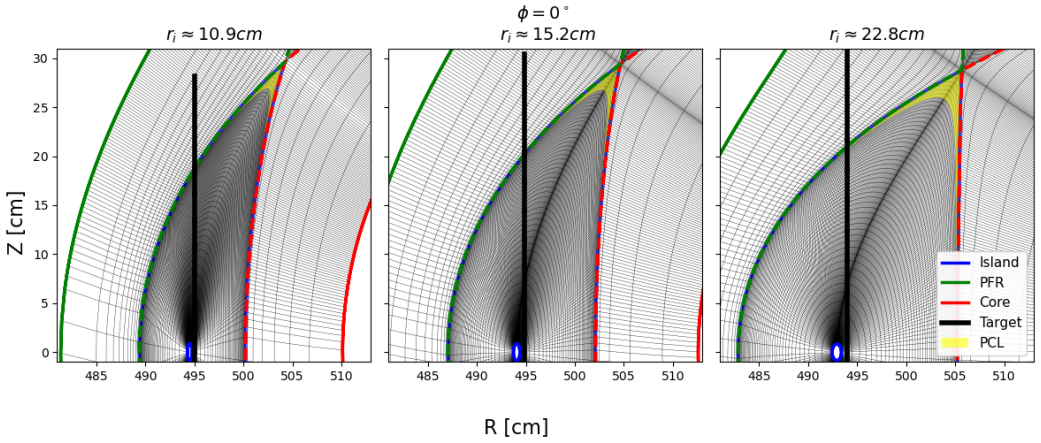

Figure 3.5: Slices on the R-Z plane at $\phi = 0°$ of the generated grids for the different island sizes with the open target plate (black). The core (red), PFR (green) and island (blue) inner and outer boundaries are highlighted.

For the base configuration, the domain of the divertor is $\phi \in [0°, 18°], [54°, 72°]$. For the configurations with a bigger island size, the target length is increased up to $\phi \in [0°, 26.64°], [45.36°, 72°]$, in order to maintain the same magnetic field incidence angle across the different configurations while ensuring the target plates cover the full island.

In the different configurations, connection length, $L_c \propto \frac{1}{\Theta}$, is modified via the field line pitch and to a lesser extent the island width: In the base configuration we have $L_c \sim 200 - 1000m$. In the configuration with the lowest field line pitch $L_c \sim 500 - 3000m$; while in the highest field line pitch configuration $L_c \sim 100 - 600m$ 3.6. For configurations with the same Θ, the L_c profile, both quantitatively and qualitatively, is the same. Although the island radial width differs, the poloidal length of each flux surface is the same, because smaller islands are more curved and stretched, see Fig. 3.4.

From Fig. 2.6, for $\Theta \ll 1$, the toroidally wetted fraction of the target plate that is in direct contact with the plasma is $\propto \Theta$. This means that changes in field line

pitch also affect the toroidal extend of the target as well as the extent of the TSR. In the highest Θ case, the target is in contact with the plasma until the plate exits the magnetic island, $\phi \in [0°, 24°], [48°, 72°]$. In contrast, in the lowest Θ case, the target plates are in contact with the plasma only in $\phi \in [0°, 7°], [65°, 72°]$, while the rest is completely shadowed from the plasma. This effect can be also seen in Fig. 3.6 by the different poloidal extend of the TSR region. Because of this, a difference of the same order of magnitude in strikeline length is expected in the EMC3-EIRENE simulations.

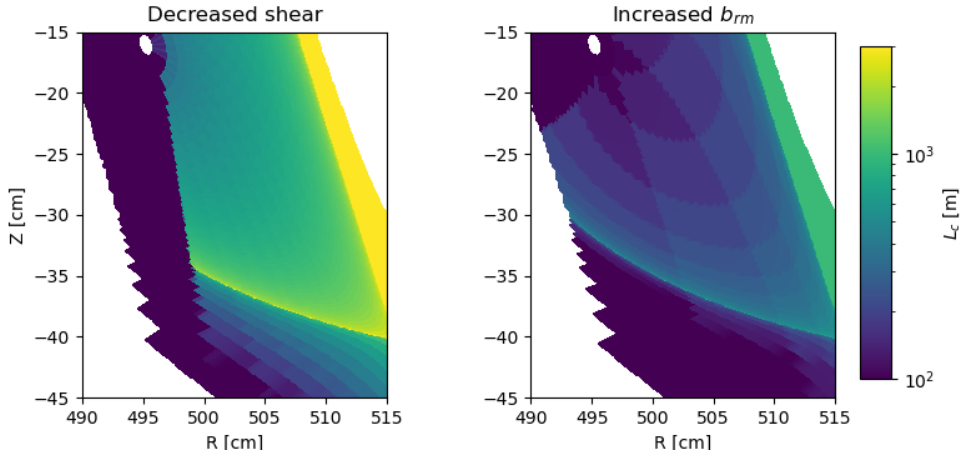

Figure 3.6: Slices of the R-Z plane at $\phi = 18°$ of two distinct configurations with $r_i \approx 22.8\ cm$. The decreased ι' one (left) has a lower Θ, while the increased b_{rm} one has a higher Θ. The target shadow region (TSR) is significantly different between the two.

3.2 EMC3-EIRENE simulations

3.2.1 Simulation setup

Using the generated geometries, EMC3-EIRENE simulations are performed. Pure hydrogen plasmas without impurities are simulated. Anomalous transport coefficients $D_\perp = 0.2\, m^2 s^{-1}$ and $\chi_e = \chi_i = \chi_\perp = 1.5\, m^2 s^{-1}$ are used. For all simulations, the power entering the SOL is set to $P_{in} = 5\, MW$. For each configuration, a density scan is implemented with several simulations at different values of inner core boundary density n_{ibd}. Simulations for each configuration are started at a low upstream density $n_{ibd} = 10^{19}\, m^{-3}$. Each simulation is iterated until convergence and the resulting steady-state solution is obtained. The solution is then used as a starting point for another simulation at higher n_{ibd}. This ordered progression is required as solutions for configurations that show a certain mode, discussed in Sec. 3.2.2.1, are hysteretic, in the sense that a different steady-state solution is obtained depending on the initial conditions used.

This process is continued until the pressure-averaged downstream temperature reaches $T_{d,av} \lesssim 5eV$ in the highest n_{ibd} simulation. Below this temperature threshold,

parts of the divertor region reach $T_{d,local} \approx 1\ eV$. The equations used miss part of the relevant physics coming into play (e.g. volumetric recombination) and solutions may diverge if n_{ibd} is increased further.

For $T_{d,av} \lesssim 10eV$ the iteration scheme of EMC3-EIRENE may start to oscillate and not converge. In these cases the electron energy sink from the neutral gas term, S_{ee}, is linearized for all terms (interaction with atoms + molecules + test ions). A density scan set is simulated for seven configurations, see Tab. 3.1, each with its own values of b_{rm} and ϵ', until convergence and the results are compared below. In this work, as the EMC3-EIRENE system is solved by iterating alternatingly its plasma (EMC3) and neutral (EIRENE) modules, the system iteration is stopped and considered converged when the relative change in the solution is typically $\leq 1\%$. Here, the solution parameters chosen to check convergence are a pressure-weighted averaged of the plasma density and of the electron temperature at the target ($n_{d,av}$, $T_{d,av}$).

3.2.2 Results Discussion

In this section, the results of the simulations performed in EMC3-EIRENE on the set of seven configurations are shown and the main observations discussed. The 2D distributions of plasma density and temperature at $\phi = 0°$ are shown. At this toroidal position, the target penetrates deepest into the magnetic island and the steepest gradients with respect to the LCFS conditions are expected.

In this work, the power-carrying layer (PCL) is defined as the radial extent of the SOL located immediately around the inner island separatrix, Fig. 3.5. The flux tubes comprised in this channel act ideally as the primary transport channel. Populated with heat flux coming from the core via cross-field transport, they simultaneously drain the heat flux to the divertor targets along the magnetic field. They are expected to concentrate the majority of the plasma's particle and heat fluxes as they are carried from the core to the divertor targets. However, the containment within this layer and its radial extent is sensitive to the magnetic field line pitch (Θ); as Θ and the ratio of parallel to perpendicular transport ($q_{\parallel}/q_{\perp}$) decrease, power and particles are pushed radially outward from the PCL, radially towards the island O-point, which can degrade overall transport performance. A quantitative view of this power channel can be found in [108].

Firstly, 2D distributions of the reference configuration case are shown, Fig. 3.7, at a low density ($n_{ibd} = 0.6e19\ m^{-3}$) and high density ($n_{ibd} = 2.5e19\ m^{-3}$) cases. The results show a qualitative correspondence with simulations for the standard configuration in W7-X. At low densities, the divertor shows qualitative agreement with the sheath-limited regime, as target density is $\frac{1}{3}n_u \lesssim n_d \lesssim \frac{1}{2}n_u$, temperatures are $T_e > 100\,eV$ throughout the island and ionization mostly happens in the core. Plasma is attached. At higher densities, the divertor shows qualitative agreement with the stellarator conduction-limited regime. The island is no more neutral-transparent,

ionization starts to occur near the target, where plasma starts to cool and density starts to build-up, as density and temperature are associated because of conservation being approximately valid. In the target region, the maximum target density achieved is of the order of $n_d \approx 1e20\ m^{-3}$, while downstream temperature drops to $T_d \lesssim 10\ eV$.

Despite the main strike point being towards the separatrix (in the PCL), the density peaks at the target extend from the strike point (separatrix) towards the O-point of the island, Fig. 3.7. This feature is qualitatively the same in W7-X standard configuration EMC3-EIRENE simulations without impurities.

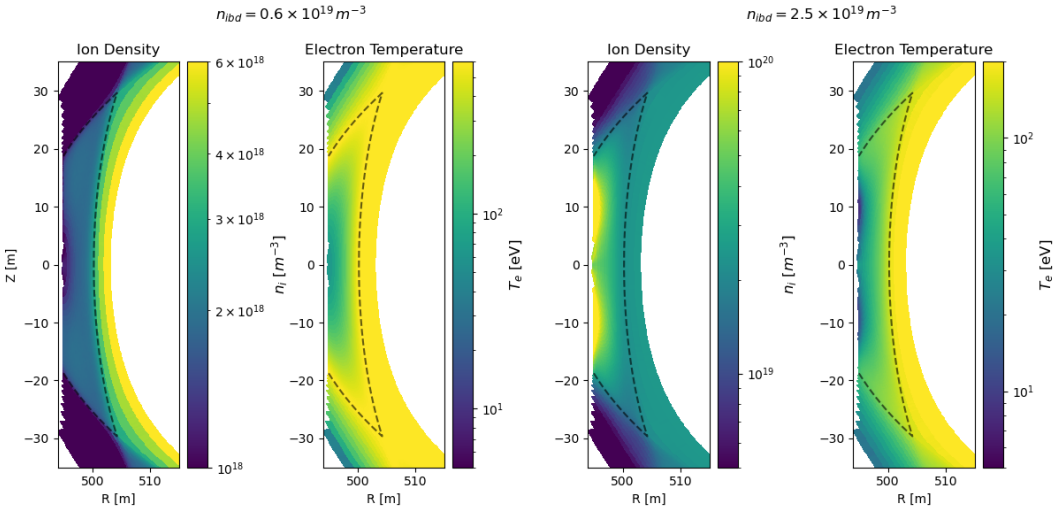

Figure 3.7: 2D distributions of plasma density n and electron temperature T_e at $\phi = 0°$ for the reference configuration.

Secondly, the reference case 2D distributions are compared respectively with: the constant Θ, decreased shear (ι') and increased b_{rm} cases. The differences in density and temperature distribution by increasing r_i and increasing/decreasing Θ are observed and compared. For each comparison, the maximum target density $n_{d,max}$ is taken from each 2D distribution.

Here, the high densities simulations are compared between the reference case and the constant Θ cases with increasing r_i, Fig. 3.8 & 3.9. The cases are compared at simulations with the same upstream density of $n_u \approx 2e19\, m^{-3}$. Throughout this chapter, this is basically the separatrix density, n_{sep}, evaluated as the average core density at the LCFS. As the objective is to maximize build-up, this comparison should show the effects on build-up of only increasing r_i.

In the constant Θ cases, the density peaks tend to shift towards the O-point and density increases with increasing r_i: $n_{d,A36a65} \approx 1.75e20\, m^{-3}$ for the reference case, $n_{d,A50a47} \approx 5e20\, m^{-3}$ for the $r_i \approx 15.2\, cm$ and $n_{d,A75a31} \approx 1e21\, m^{-3}$ for the $r_i \approx 22.8\, cm$. The latter is the case with the maximum downstream densities of this set of simulations. Increasing r_i is observed to significantly increase $n_{d,max}$.

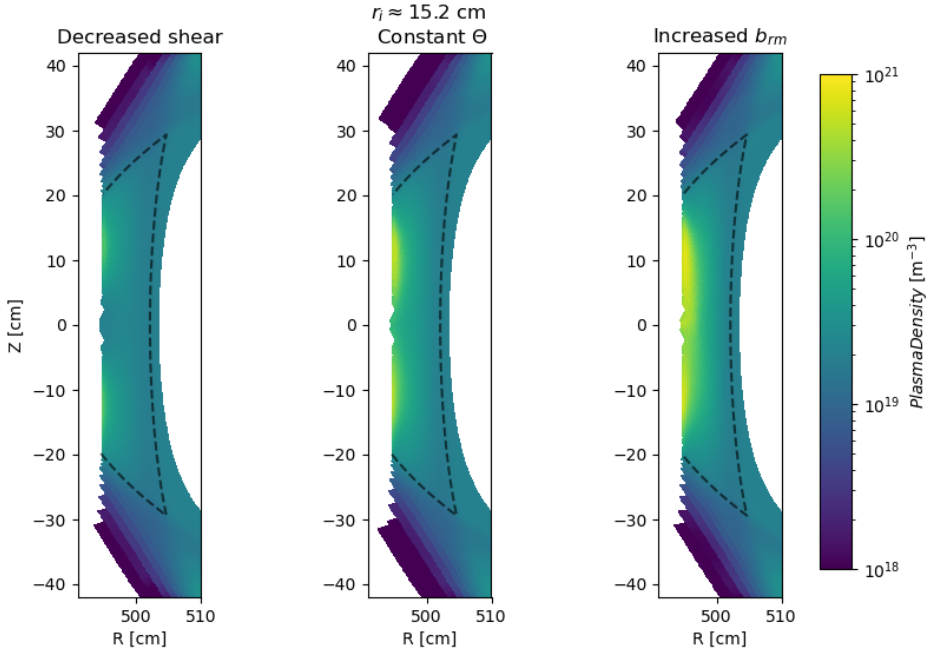

Figure 3.8: 2D distributions of plasma density n at $\phi = 0°$ for the $r_i \approx 15.2$ cm cases.

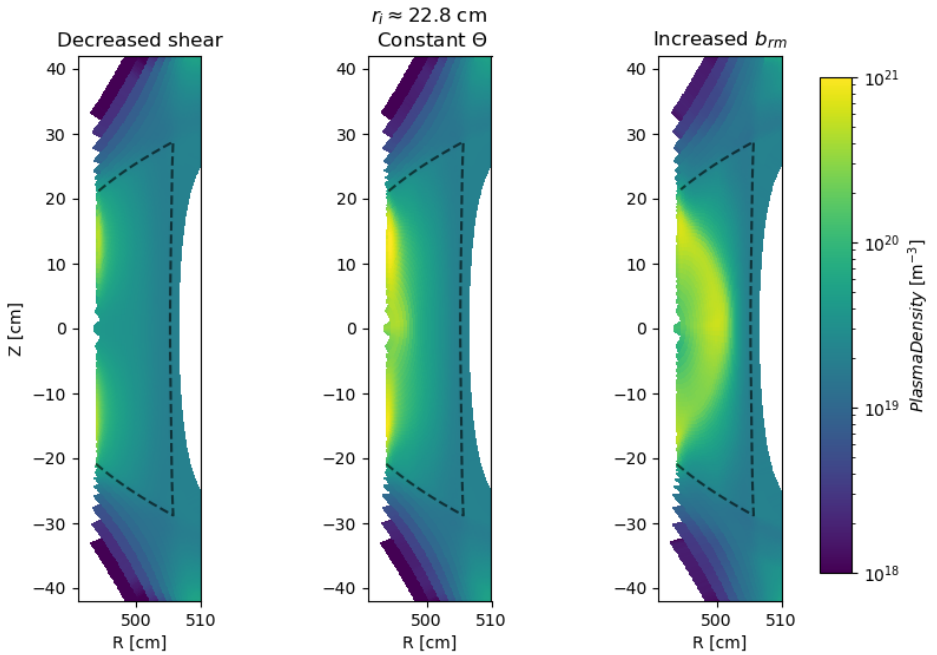

Figure 3.9: 2D distributions of plasma density n at $\phi = 0°$ for the $r_i \approx 22.8$ cm cases.

Next, the high densities simulations (still $n_u \approx 2e19\, m^{-3}$) are compared between the reference case and the decreased ι' cases with increasing r_i. In general, as the objective is to maximize the downstream density n_d, as seen in Chap. 2, decreasing

Θ is expected to hinder density build-up.

In the decreased ι' cases, it is observed how the qualitative W7-X profile is kept while increasing the island size. The density peaks at the target tend to shift from the O-point towards the island separatrix/strikepoint. For the simulations with upstream density $n_u \approx 2e19\,m^{-3}$, the maximum density at the target increases with increasing island size: $n_{d,A36a65} \approx 1.75e20\,m^{-3}$ for the reference case, $n_{d,A36a34} \approx 2e20\,m^{-3}$ for the $r_i \approx 15.2\,cm$ and $n_{d,A36a15} \approx 5e20\,m^{-3}$ for the $r_i \approx 22.8\,cm$, Fig. 3.8 & 3.9. This implies that for decreasing magnetic shear, the advantage in increased island size outperforms the expected disadvantages from a decrease in field line pitch. However, decreased Θ is observed to hinder density build-up, as the cases with a lower Θ have a lower $n_{d,max}$ at the same r_i. Electron temperature near the LCFS is observed to increase as ι' is decreased, Fig. 3.10 & 3.11.

Finally, the high densities simulations (still $n_u \approx 2e19\,m^{-3}$) are compared between the reference case and the increased b_{rm} cases with increasing r_i. In general, increasing Θ is expected to benefit density build-up.

In the increased b_{rm} cases, the density peaks tend to shift towards the O-point. On the density build-up perspective, in the increased b_{rm} cases the maximum density at $n_u \approx 2e19\,m^{-3}$ is: $n_{d,A36a65} \approx 1.75e20\,m^{-3}$ for the reference case, $n_{d,A70a65} \approx 7.3e20\,m^{-3}$ for the $r_i \approx 15.2\,cm$ and $n_{d,A157a65} \approx 6.7e20\,m^{-3}$ for the $r_i \approx 22.8\,cm$. Maximum downstream density does not increase anymore monotonically with island size and tends to saturate. Electron temperature near the LCFS is observed to decrease as b_{rm} is increased, Fig. 3.10 & 3.11. The expected benefit of increased Θ on build-up is only partially observed in the intermediate $r_i \approx 15.2\,cm$ island configuration. However, a novel state of the plasma in the island divertor is noticed here and discussed in the next section.

In simple SOL physics a small region of high particle flow, with $M = 1$, is assumed only close to the target plate, while the rest of the plasma is stagnating. This is a good approximation for the tokamak poloidal divertor, where the $\parallel$ flows away from the target are usually low [28]. On the other hand, the island divertor $\parallel$ flow stagnation region is usually located near the island symmetry midplane, from the LCFS to the O-point. This creates strong $\parallel$ counter streaming flows within the island also far from the target, Fig. 3.13. The counter streaming flow regions can generate strong momentum lossed in the island divertor via viscous transport [29].

To see the qualitative macroscopic effects of geometric parameters on the island particle flow, the 2D distributions of Mach number are shown and compared for varying Θ, Fig. 3.12 and varying r_i, Fig. 3.13. The region of high Mach number is observed to extend from the target, where $M = 1$, further upstream with increasing field line pitch, Fig. 3.12, and to be more contained with increasing island size, Fig. 3.13. Because of this, parallel heat convection and momentum losses should be observed to decrease the most in large islands and low ι' configurations, while expected to increase the most in large islands with increased b_{rm}. Increasing Θ appears not to

be beneficial for momentum losses and to also affect the flow stagnation region.

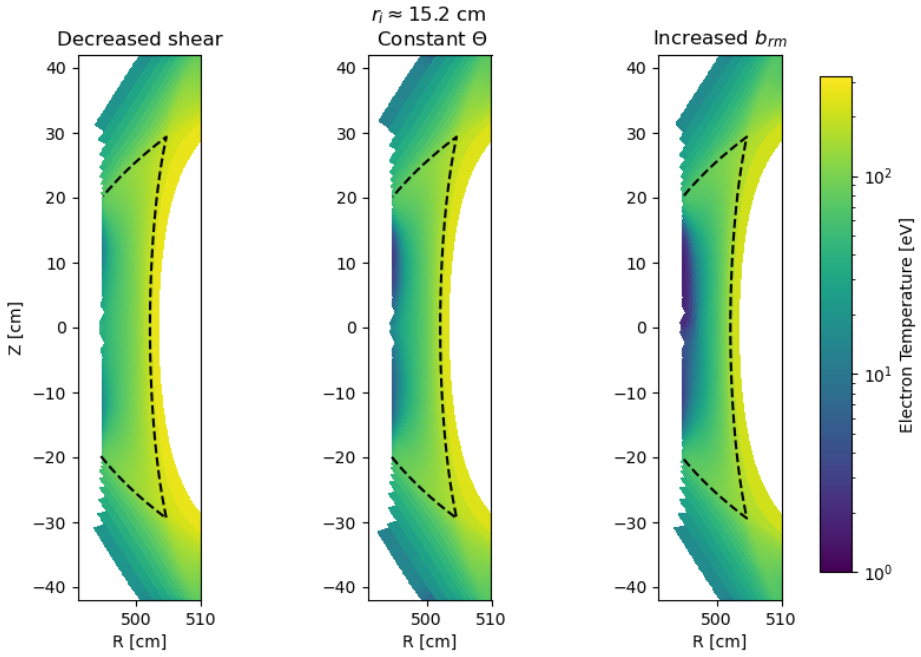

Figure 3.10: 2D distributions of electron temperature T_e at $\phi = 0°$ for the $r_i \approx 15.2$ *cm* cases.

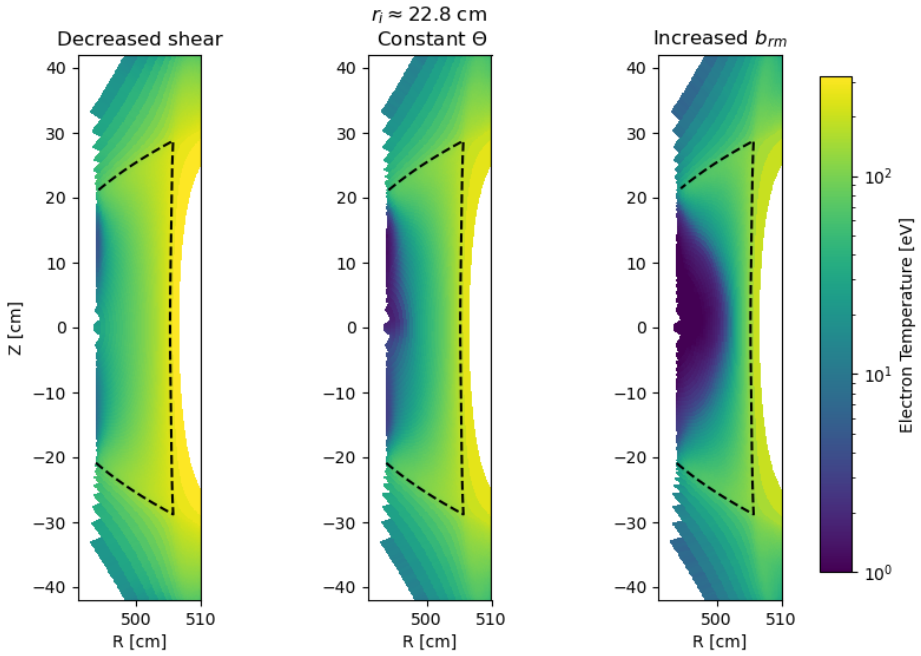

Figure 3.11: 2D distributions of electron temperature T_e at $\phi = 0°$ for the $r_i \approx 22.8$ *cm* cases.

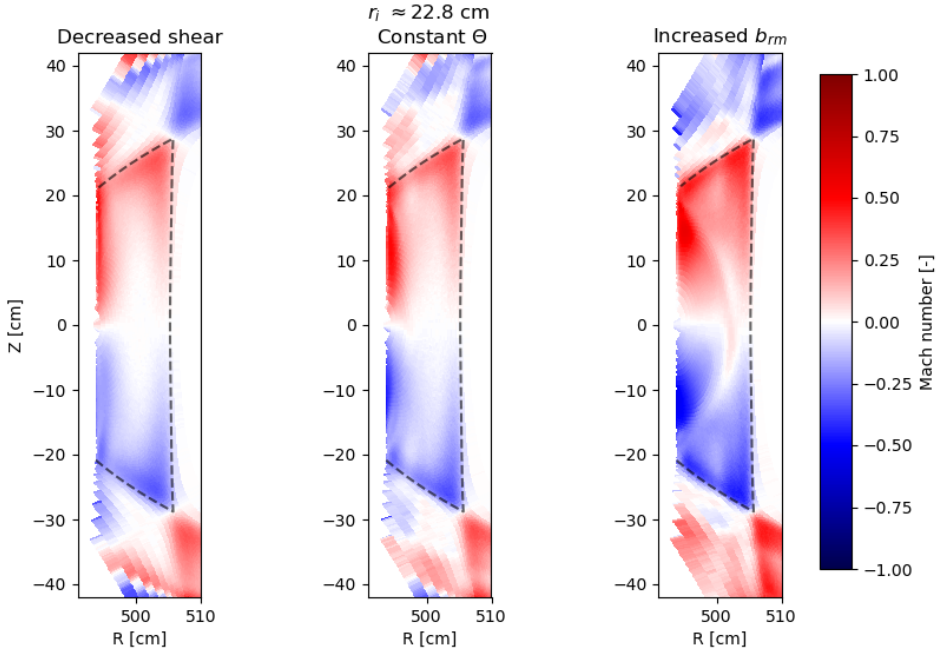

Figure 3.12: 2D distributions of Mach number M at $\phi = 0°$ for the $r_i \approx 22.8$ cm cases.

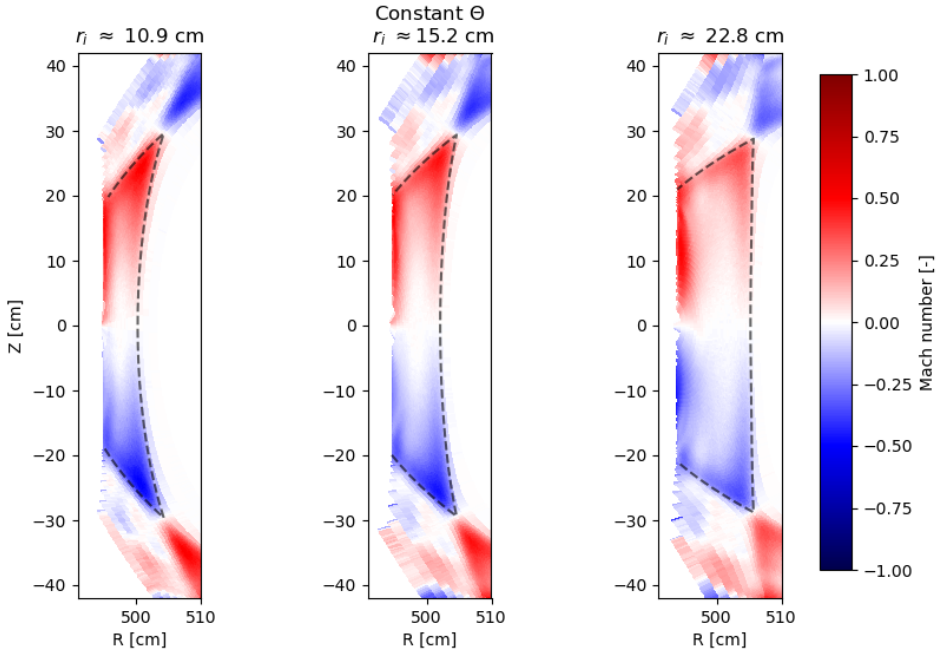

Figure 3.13: 2D distributions of Mach number M at $\phi = 0°$ for the constant Θ configurations.

3.2.2.1 Neutral-transparent O-point regime

In this section, attention is focused on three specific configurations out of this set, where a novel island divertor regime is observed.

In the $r_i \approx 22.8\,cm$, constant Θ case and in the two increased b_{rm} cases, Fig. 3.8 & 3.9 the two density peaks at the target are observed to gradually shift towards the O-point and expand radially, eventually becoming a single high density region surrounding the O-point. In this region, electron temperature is $T_e \lesssim 2eV$, Fig. 3.10 & 3.11. The plasma particle source term S_p, Fig. 3.14 shows where the ionization reactions happen in the geometry. For the other configurations the ionization region is close to the target, while in these cases it gradually shifts away from the O-point, remaining close to the target at the separatrix in a arch shape.

This mode, which in this thesis will be called neutral-transparent O-point regime, seems to be different from what has been already explored in W7-X standard configuration.

What is hypothesized in this thesis is that, by either increasing r_i or Θ, there is a portion of the island, towards the center of the target, that experiences very little plasma density $n_u \lesssim 1e18\,m^{-3}$ and temperature $T_{e,d} \lesssim 10\,eV$. At low separatrix densities, what drives most of the plasma inside the island is $\perp$ transport from the LCFS. Increased island size, r_i, or $\parallel$ / $\perp$ transport ratio ,Θ, both lead to less power/particles reaching the O-point, starving it of power for sustaining a plasma. The low temperatures and absence of plasma make for a very high neutral mean free path in the region with respect to other configurations. Consequently, once the recycled neutrals/impurities can freely travel the region, additional power losses due to radiation and ionization at the interface to the PCL across the full island will exacerbate and stabilize this regime. Hence the name neutral-transparent O-point regime.

It is also observed how as the neutral-transparent O-point volume increases, increased plasma-neutral interaction causes more losses. It is showed here the impact on neutral momentum losses, Fig. 3.15, which could explain why once conduction limited regime is achieved in the increased Θ and r_i cases, density tends to saturate. In general, as the neutral-transparent O-point regime grows in intensity, increase in density build-up reaches a plateau and upstream T_e decreases with respect to the reference case, possibly leading to core confinement degradation. These phenomena, linear density build-up at high upstream densities and decrease in upstream T_e, in the STPM are associated with the diffusion limited regime (decreasing Θ). However, here they strengthen also when increasing Θ, probably due to this regime.

In this W7-X like open divertor configuration, this means that when conduction-limited regime is achieved, recycled neutrals ejected from the plate travel further into the island, in this neutral-transparent volume, and, instead of ionizing near the target plate, they ionize at the border of this volume with the plasma, Fig. 3.14. Finally, in an open configuration, this creates a low temperature, plasma and neutral dense volume surrounding the island O-point.

The influence of both these island parameters in achieving the neutral transparent

O-point can be distinguished also by the qualitative similarity between the $r_i \approx 22.8\,cm$ configuration obtained by only increasing island size and the $r_i \approx 15.2\,cm$ configuration obtained by increasing island size and Θ, Fig. 3.8 & 3.9.

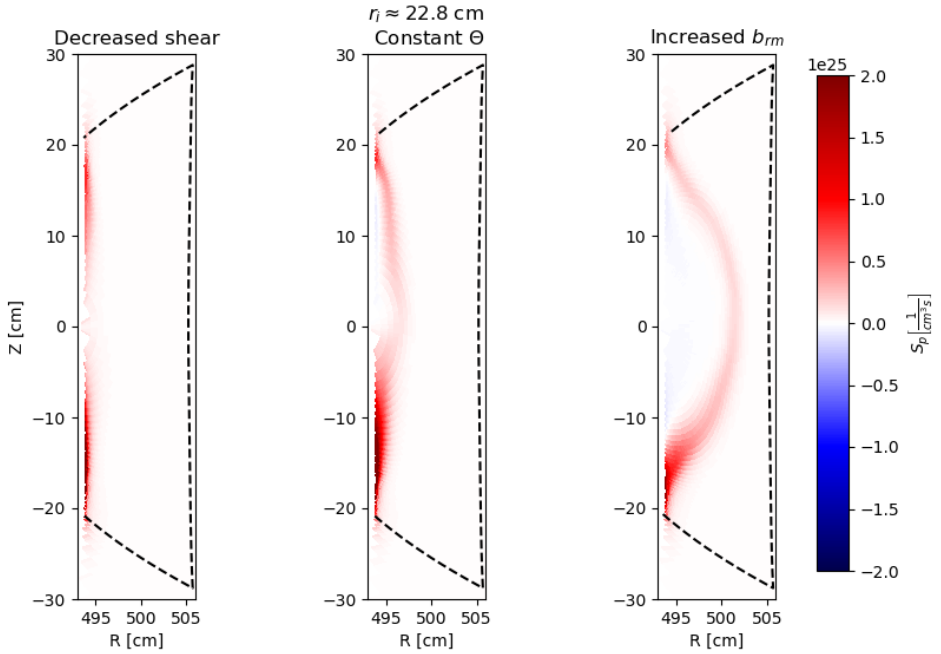

Figure 3.14: 2D distributions of the particle source S_p at $\phi = 0°$ for the $r_i \approx 22.8\ cm$ cases.

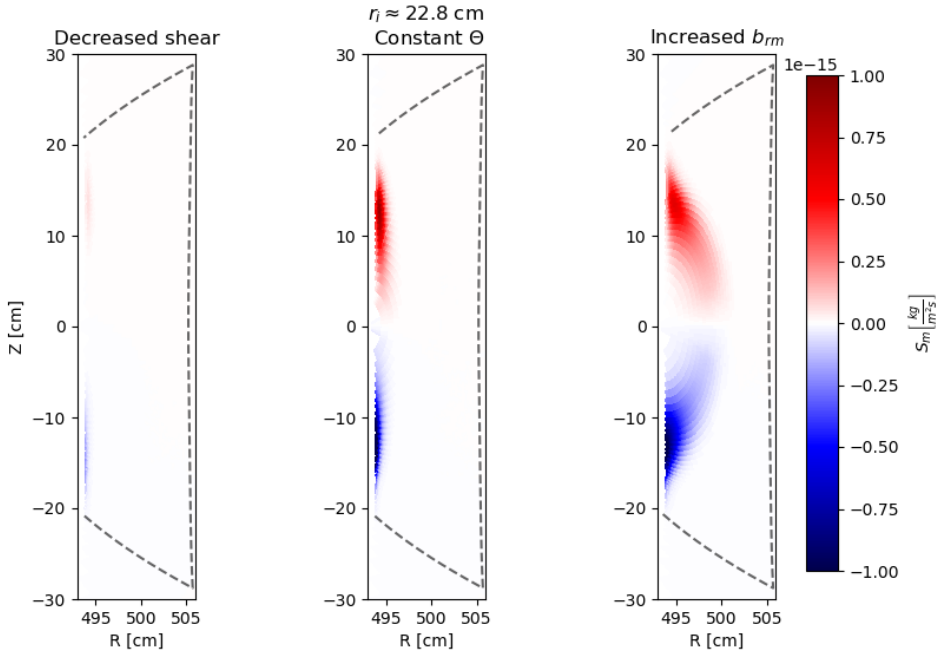

Figure 3.15: 2D distributions of the momentum losses due to plasma-neutral interaction S_m at $\phi = 0°$ for the $r_i \approx 22.8\ cm$ cases.

We give a comparison between W7-X island geometric parameters ranges and the geometric parameters of the configuration with a neutral-transparent O-point closest to W7-X.

In W7-X, using control coils, island size varies in the range of $r_i \sim 5 - 10\ cm$. [92]. The reference configuration of this work has a similar ι' value with respect to W7-X, Fig. 3.2, and a $r_i \approx 10.9\ cm$ a little above W7-X upper limit listed above. This island size is obtained with $b_{rm} \approx 3.8e-4$. The configuration with the closest geometric parameters that showed this novel regime has the same ι' and a $r_i \approx 15.2\ cm \approx 1.5 r_{i,W7-x}$, obtained with a $b_{rm} \approx 7.3e-4$. In real case scenarios, where coils excite a spectrum of resonant perturbations, magnetic island configurations with these magnitudes of r_i and/or Θ may incur in MFC.

However, if this regime is physically achievable in terms of Θ and r_i, the low temperature O-point could be beneficial for the design of a closed island divertor [86]. The low temperature volume could be used to place the divertor. Most of the plasma would be directed to the strikeline, while at the top the divertor would be protected from sputtering and plasma interaction from the $T \lesssim 5\ eV$ region.

On the other hand, in the current open island divertor, this regime could present some issues, as there would be a very large volume where elastic collisions with neutrals/molecules, charge exchange and molecular dynamics are dominant. The ionization zone would be pushed to the boundary of this volume and the effects on stellarator detachment and impurity retention are yet to be analyzed. This regime has proven to be also cumbersome on the computational level, as convergence was hard to achieve and solutions tend to oscillate, mainly due to the increased plasma-neutral interaction. This could be an indication for the occurrence of instabilities in the plasma.

It must be stressed that this regime has been observed in a simplified geometry, where resonant surfaces are artificially selected and can thus be increased in size arbitrarily. However, future improvements in magnetic optimization and chaos suppression could help achieve these parameters in real geometries, without the onset of MFC changing the leading order physics. This regime will then have to be confirmed in the future by studies on more realistic geometries and with experiments.

3.2.2.2 Global build-up

In this section, density build-up in the different simulations is specifically compared. In order to condense the multitude of simulations into a tractable display we show TPM-like density-build up plots (see Fig. 2.5). The downstream parameters in simulations can be evaluated in two different ways. The global approach, showed in this section, uses a pressure-weighted average of the target quantities ($n_d = n_{d,av}$, $T_d = T_{d,av}$) for the downstream parameters, while it uses the average LCFS quantities for the upstream parameters ($n_u = n_{LCFS,av}$, $T_u = T_{LCFS,av}$). The local approach, used in Chapter 4, uses the local quantities of a selected fieldline in the

power carrying layer as upstream and downstream parameters ($n_u = n_{u,fieldline}$, $T_u = T_{u,fieldline}$,$n_d = n_{d,fieldline}$, $T_d = T_{d,fieldline}$).

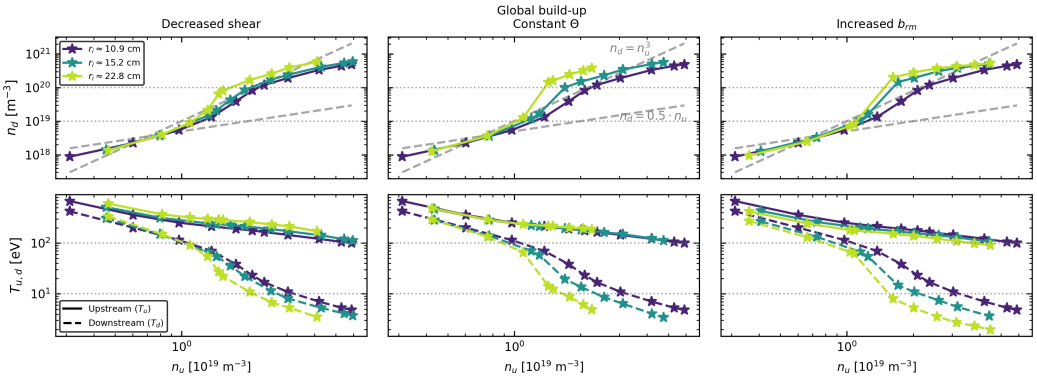

Figure 3.16: Comparison of global density and temperature scalings in the different r_i and Θ cases studied in this section.

First, looking at the density build-up plot of Fig. 3.16,[1] the build-up improves with increasing island radius, r_i, independent of the field line pitch, Θ. However, build-up is improved with increasing field line pitch up to a threshold. The best build-up, both in terms of maximum achievable downstream density ($n_{d,max}$) and maximum downstream density for a given upstream density ($n_{d,av}(n_u)$), is given by the $r_i \approx 22.8\,cm$ configuration with constant Θ, Fig. 3.16. Between the $r_i \approx 15.2\,cm$ island size cases, the higher Θ (increased b_{rm}) configuration has the better build-up. Increasing Θ further tends to cause a saturation in the density build-up, probably because of the neutral-transparent O-point regime, as it has already been observed with the maximum downstream density from the 2D distributions above.

It is hypothesized that in the open divertor configuration, as the one used in this work, the increased $\parallel$ particle flow throughout the island, Fig. 3.12, in addition to the intense plasma momentum and power losses happening due to plasma-neutral interaction in the neutral-transparent O-point region, Fig. 3.15 hinder further plasma build-up once conduction limited regime is achieved. These intense losses could also disrupt the pressure conservation assumption between the upstream and downstream locations. The conservation is approximately valid for the other cases, where a drop in T_d is associated with a proportional increase in n_d, and differences in T_d drops between configurations are associated with qualitatively similar differences in n_d increases, Fig. 3.16.

However, in the increased b_{rm} configurations with $r_i \approx 15.2\ cm$ and $r_i \approx 22.8\ cm$, while the difference in T_d drop between the two persists with increasing n_u, the density build-up eventually reaches the same plateau, indicating more intense pressure losses in the increased b_{rm}, $r_i \approx 22.8\ cm$ case. In general, previous to this results, it

[1]The $r_i \approx 22.8\,cm$ configuration with constant Θ could not be simulated further than $n_u \approx 2.2e19\,m^{-3}$, because of numerical stability reasons, as $T_d \lesssim 1\ eV$.

was foreseen that increasing Θ and r_i would monotonically improve transport and build-up in the open island divertor. However, looking at these results, in order to obtain the best possible density build-up, one has to find a trade-off between island size and field line pitch.

Next, looking at the temperature plots of Fig. 3.16, we notice that, in accordance with the STPM, configurations with the same connection length, $L_c \propto 1/\Theta$,(the constant Θ cases) have the same upstream temperature T_u. Higher L_c cases (the decreased ι' cases) have a higher upstream temperature, while the opposite happens with low L_c cases (the increased b_{rm} cases). The expected increase of connection length with island size for the constant field line pitch cases is absent as changes in the island shape compensate the radial size increase and virtually leave the circumference, and hence connection length, unaltered, Fig. 3.4.

Finally, when simulating the same configuration at different n_{ibd}, to build the $n_d(n_u)$ curve, it was observed that for a small increase in n_{ibd}, a jump in value is observed, both in separatrix (n_u) and pressure-averaged downstream densities (n_d). The magnitude of the jump increases with r_i and Θ, while the increase needed of n_{ibd} decreases accordingly. For example, in the $r_i \approx 22.8$ and high Θ case, a jump from $n_d \approx 8e18\,m^{-3}$ to $n_d \approx 2e20\,m^{-3}$ and from $n_u \approx 1.1e19\,m^{-3}$ to $n_u \approx 1.6e19\,m^{-3}$ is caused by a n_{ibd} change from $\approx 1.55e19\,m^{-3}$ to $\approx 1.65e19\,m^{-3}$. These drops are visible in Fig. 3.16. An associated drop in T_d for every jump of this kind is observed, which makes the pressure conservation assumption still approximately valid. Whether this is due to physics or numerics remains to be investigated. If this phenomenon is found to be physical, it could be beneficial for build-up, given that it is a positive steep increase in downstream density in the $n_d(n_u)$ curve. However, configurations with a steeper jump, such as the increased b_{rm} ones with $r_i \approx 15.2\ cm$ and $r_i \approx 22.8\ cm$, are found to have strongly hysteretic $n_d(n_u)$ curves, where the shape of the curve fundamentally changes if new simulation points are obtained from lower or higher density simulations.

In this section, the influence of island geometric parameters (b_{rm}, ι', r_i, Θ) on build-up have been studied and observed. In the next section, the reference configuration is used to study the influence of target placement on density build-up.

3.3 The Influence of Target Placement

In this section, to assess the impact of target placement in the island divertor, another set of simulations is performed in this simplified circular geometry. In the current 5/5 island chain there are three possible stellarator-symmetric target locations around the symmetry plane. The reference configuration of Section 3.1 is used to assess the impact of target placement on divertor performance. The reference case island geometry is used and three different targets are simulated.

The three implemented target positions are shown in Fig. 3.17. The first is

a configuration where both target plates are at the inboard side of the toroidal geometry. The second is a configuration where one target plate is put at the top of the toroidal geometry and the other plate at the bottom. The last is a configuration where both target plates are at the outboard side of the toroidal geometry.

In the case of the top/bottom island configuration (green in Fig. 3.17), the target plates in the simulations are not on the same/continuous islands (as in W7-X). The strike lines hitting one target plate cannot fully be captured by the other one if the same target shape of the previous section is used, 3.1.2. To make sure that all of the power leaving the plasma domain is deposited onto the target in the simulations, the shape of targets used for this section is changed and mantained the same, for the sake of comparison, in the inboard, top/bottom and outboard cases.

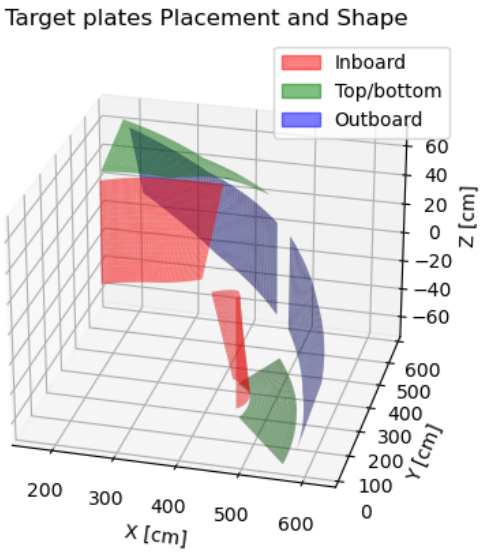

Figure 3.17: 3D visualization of the three target configurations used in this section.

Here, the first target plate is between $\phi \in [3°, 33°]$. The target starts at 3°, reaches its maximum depth in the island at 18° and symmetrically retracts back until 33°. The same is done for the second target at $\phi \in [39°, 71°]$.

The connection length L_c 2D distribution of these three configurations is shown in Fig. 3.18. L_c is the same magnitude, but target shadowing is different for the different targets. The TSR is identical for the Inboard & Outboard targets, where one half of the target is shadowed for 16° out of the total 18° of toroidal target extent, while the other is shadowed only for the final 2° of the target. In this case we expect one single strikeline per target on the side, Fig. 3.20, with a TSR extending only in the last 2°. In the top/bottom case, instead, the target is partially shadowed on both sides of the targets for the same toroidal extent. We expect two symmetrical strikelines in this case.

In Fig. 3.18 it is possible to see how the island in the outboard case is completely shadowed at $\phi = 23°$. The top/bottom island is partially shadowed, while the Inboard island is the least shadowed out of the three. Knowing that at $\phi = 18°$ the target reaches one half of its toroidal extent and its deepest radial penetration into the island, the shadowing at $\phi = 13°$ is specular to the one at $\phi = 23°$. The Inboard island is completely shadowed, the top/bottom has the same degree of shadowing of before, while the Outboard island is the least shadowed out of the three.

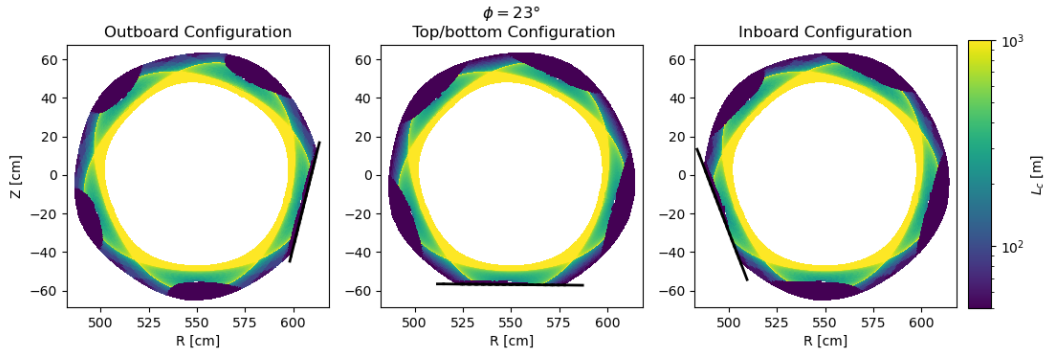

Figure 3.18: 2D distribution of the connection length L_c for the three different target configurations.

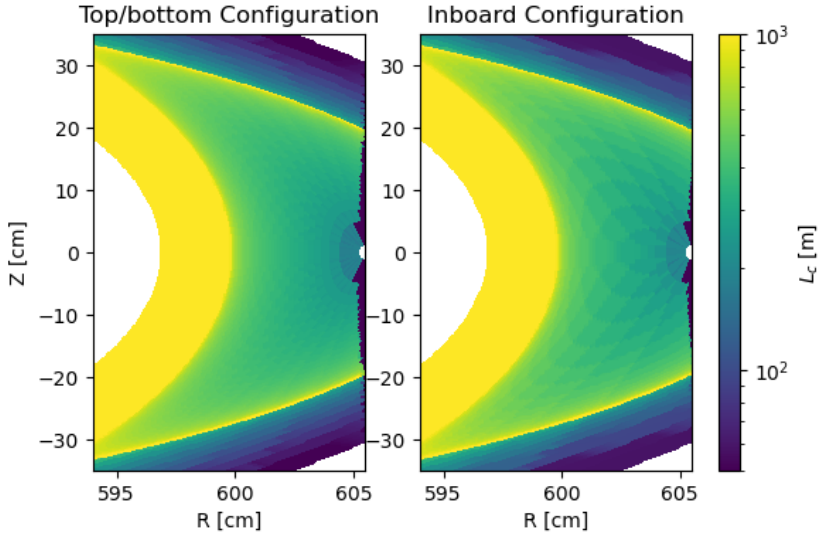

Figure 3.19: 2D distribution of the connection length L_c highlighting the different L_c steps in the top/bottom configuration.

The heat fluxes onto the plates are obtained via post-processing of the plasma simulations for the cases of $n_{sep} \approx 3e19\ m^{-3}$. Fig. 3.20 shows the results for the Inboard and top/bottom case. As expected from the target shadowing, the strike line in the Inboard case is mainly on one side of the two targets and extends for $\approx 11°$ toroidally. On the other hand, the top/bottom case strike line is equally distributed on both sides of the targets, expanding for $\approx 8°$ toroidally on each side. The inboard case has the highest heat flux peak at 4.3 MW/m^2. The Outboard case, not shown here, has a identical qualitative behaviour compared to the Inboard case and a peak heat flux 3.8 MW/m^2. The top/bottom has the lowest peak heat flux of the three at 3.5 MW/m^2.

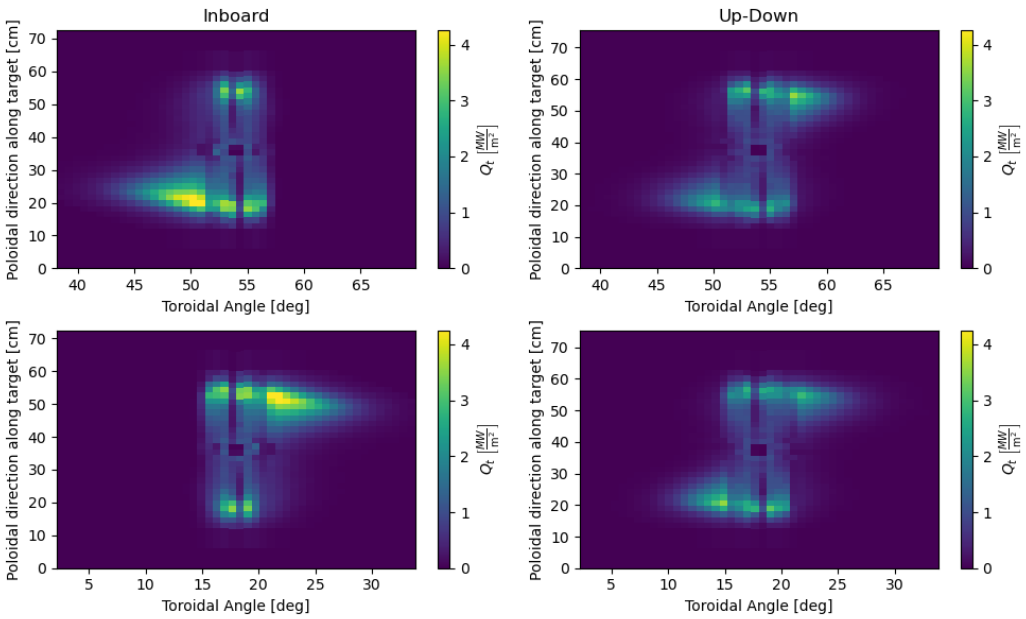

Figure 3.20: Visualization of the target heat flux q_t distribution.

Additionally, Fig. 3.19, the split targets in the top/bottom configuration lead to shorter connection length steps between the two targets compared to the other two configurations, where the targets are a full toroidal turn apart. This is reminiscent of the difference of connection length is Sec. 3.1.2.

EMC3-EIRENE simulations for these different target geometries show more or less a similar behavior, as shown in Fig. 3.21. Inboard and top/bottom target simulations have virtually the same build-up, while the Outboard target simulations shows an improved density build-up and stronger downstream temperature drop for $1e19\ m^{-3} \lesssim n_{up} \lesssim 3e19\ m^{-3}$. For even higher $n_{up} \gtrsim 3e19\ m^{-3}$ the different cases n_d and T_d profiles converge again. The reason for this differences will be analyzed in Sec. 3.3.1.

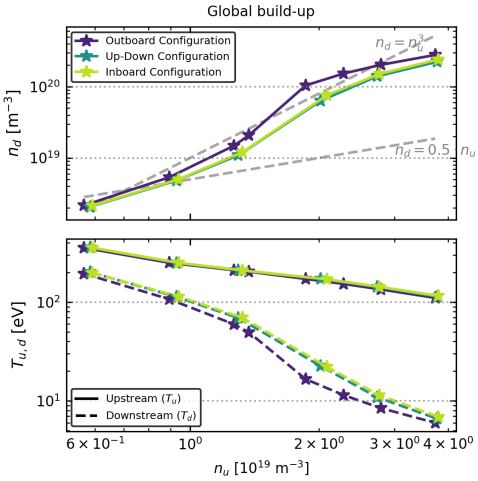

Figure 3.21: Density and temperature scalings in the different target configurations.

3.3.1 The Influence of Target Concavity

In this section four other configurations are made and simulated in EMC3-EIRENE to better understand what drives the differences in density build-up in the configurations with different target placement.

We have two hypotheses for the difference in performance of the outboard target configuration: First,the difference could arise from the toroidal magnetic field

dependence on major radius $B_\phi \sim \frac{1}{R}$.

In the base geometry case magnetic field strength varies between $2.25\ T \lesssim B_\phi \lesssim 2.75\ T$, from outboard to inboard, because of varying R at the target location. The change in total magnetic field strength is connected to different total flux expansion at the outboard and inboard islands, causing differences in the local heat flux density [109]. In addition to that, outboard islands in toroidal geometries tend to maintain the same island radius (radial width), but are stretched poloidally along the LCFS, resulting in a increased poloidal width and a bigger volume occupied. This hypothesis however is not thoroughly considered since, if this would be the main cause of the difference, a difference in build-up between the inboard and top/bottom configuration would also be observed.

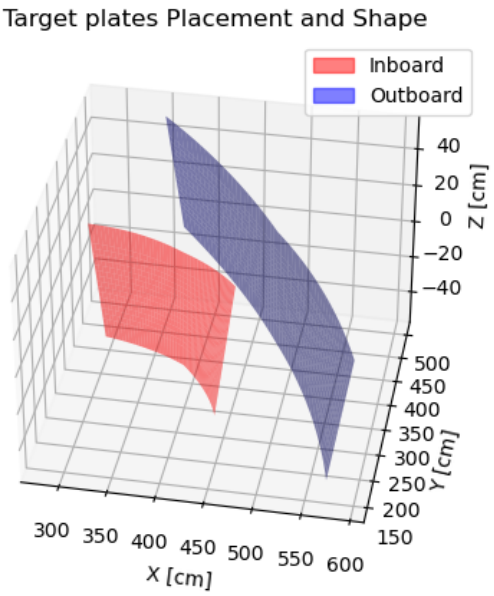

Figure 3.22: 3D visualization of the outboard and inboard target and their concavity/convexity.

The second hypothesis is that target concavity improves neutral accumulation at the toroidal center of the target. Since the target plate helically follows the island while slowly radially entering and exiting the island, the shape of the target is affected from toroidal curvature, Fig. 3.22.

When the target is positioned on the inboard island, it ends up assuming a toroidally convex shape, while the same target becomes toroidally concave if positioned on the outboard island. Neutrals are generally released perpendicular to the target plate [110]. CX-reactions with the plasma additionally provide them with toroidal momentum. Hence, the neutrals are effectively pushed in towards the target for a concave target and diverted away from it for a convex one.

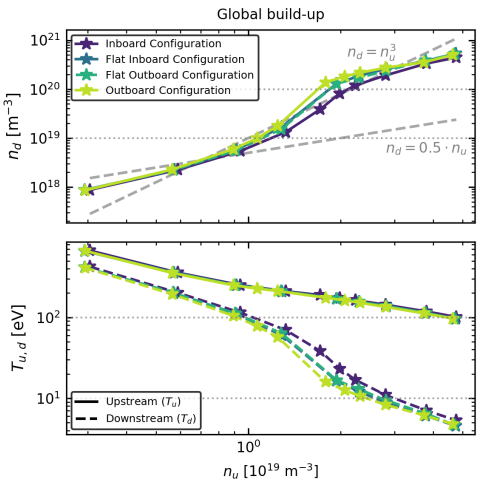

Figure 3.23: Density and temperature scalings for the reference and cylindrical configurations.

In order to explore if the increased density build-up in the outboard target case could be due to these hypotheses, simulations of three different geometries are designed for the reference geometry parameters and compared. The standard target plate generation of Sec. 3.1.2 is used in all cases. Simulations on the in-

board and outboard target are performed for the reference case and a geometry that approximates a cylinder, where targets should remain flat both outboard and inboard.

In order to achieve a cylinder-like configuration with the toroidally flat targets, a new magnetic geometry is created with HaGrids. Starting from the reference case parameters, the major radius R is increased hundred-fold to $R = 550\ m$. To compensate the impact on L_c a corresponding increase in the toroidal mode number is used to preserve the physical helical pitch of the field lines, $\iota = \frac{n}{m} = \frac{500}{5}$. Consequently, the toroidal symmetry period of the device shrinks from 72° to 0.72°. By simulating $\frac{1}{500}$ of the toroidal domain, the domain volume is perfectly preserved. Minor radius $a \approx 0.55\ m$ and magnetic field strength $B_0 = 2.5\ T$ remain the same.

Remembering from Eq. 3.2 that $\iota' \propto a_\iota$ and Eq. 3.4 that $b_{r,m} \propto \frac{A_1}{R}$ and inserting these respectively into Eq. 2.5 and Eq. 2.6:

$$r_i \propto \sqrt{\frac{R b_{r,m}}{\iota'}} \propto \sqrt{\frac{A_1}{a_\iota}} \tag{3.7}$$

$$\Theta \propto \sqrt{\frac{\iota' b_{r,m}}{R}} \propto \sqrt{\frac{a_\iota A_1}{R^2}} \tag{3.8}$$

In a simulation that has a hundred times the major radius R, a_ι and A_1 have to increase by factor ten to keep the same island conditions. Thus, $a_\iota = 6.5$, $b_\iota = 84.565$ and $A_1 = -0.36\ Wb$ are used. The resulting geometry has the same island radius and connection length L_c of the reference configuration. The approximate cylindrical magnetic geometry without significant curvature then yields toroidally flat targets.

Concomitant with the curvature, also differences that can be attributed to the $B_\phi \sim \frac{1}{R}$ dependence disappear, since the magnetic field strength is observed to be $B_\phi \approx 2.5\ T$ throughout the geometry.

As shown in Fig. 3.23, the cylinder-like configuration indeed shows the same density build-up on both the inboard and outboard target. The build-up is in between the inboard and outboard configurations of the reference case. As observed in Section 3.3, the difference between configurations appears at $n_{sep} \gtrsim 1e19\ m^{-3}$ and tends to vanish at $n_{sep} \gtrsim 3e19\ m^{-3}$. The maximum increase in build-up in the reference case from inboard to outboard island target is $\frac{n_{d,Out}}{n_{d,In}} \approx 3.5$ at $n_u \approx 1.75\ m^{-3}$. This strongly support the leading role of the target concavity and/or total flux expansion on the differences in density build-up of the different target geometries.

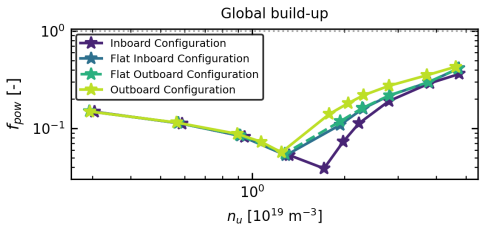

Figure 3.24: Scaling of the global f_{pow} for the reference and cylindrical configurations.

In order to quickly assess the impact of neutrals on power exhaust in the different configurations, the fraction of total power that is dissipated by neutrals is evaluated as $f_{pow} = \frac{P_{ng}}{P_{ng}+P_t}$, where P_{ng} is the total power dissipated by the neutral gas in the full simulation domain (radiation, CX & ionization) and P_t is the total power absorbed by the target. Looking at global f_{pow}, Fig. 3.24, it is observed how the change into a regime where neutrals start to absorb more than 10% of the power coming from the SOL is delayed in the more convex target geometries. The power absorbed by neutrals saturates at higher densities, probably due to target temperatures reaching $T_d \lesssim 10\ eV$ and reaction rate for ionization $\langle\sigma v\rangle_{ion}$ starting to decrease exponentially at these temperatures. The maximum increase in f_{pow} in the reference case from inboard to outboard island target is $\frac{f_{pow,Out}}{f_{pow,In}} \approx 3.5$ at $n_u \approx 1.75\ m^{-3}$. The same value as for the density above.

To elucidate the impact of total flux expansion, we look at the heat flux densities for a field line in the PCL. The fieldline is selected such that it is in the PCL (very close to the separatrix), Fig. 4.1, and it hits the target in its region of deepest penetration (for details, see Sec. 4.1). As $\perp$ transport coefficients are taken to be the same, the observed exponential decrease of $q_{\parallel,up}$ with increasing n_{sep} is likely driven by the density dependence of the flux surface perpendicular transport ($n\chi$). However, the ratio between the inboard and outboard cases for the reference configurations stays similar with $0.85 \lesssim \frac{q_{\parallel,up,In}}{q_{\parallel,up,Out}} \lesssim 1.05$. In contrast, downstream $q_{\parallel}$ is significantly reduced in the outboard cases and the ratio of downstream heat flux is $1.1 \lesssim \frac{q_{\parallel,down,In}}{q_{\parallel,down,Out}} \lesssim 1.45$. The expected $1/R$ reduction is in the order of $\frac{q_{\parallel,down,In}}{q_{\parallel,down,Out}} \propto \frac{R_{out}}{R_{in}} \approx 1.22$, which is close to the actual values. While $q_{\parallel,up}$ is not dominated by flux expansion effects, $q_{\parallel,down}$ is impacted in non negligible part by flux expansion. It is not possible to exclude one of the two hypothesis at the moment and further investigation is required for the future.

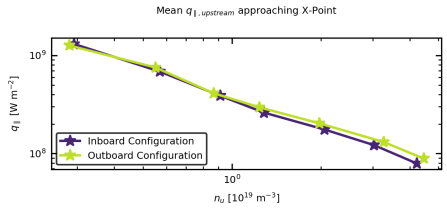

Figure 3.25: Mean upstream heat flux $q_{\parallel,up}$ scaling for the outboard and inboard configurations.

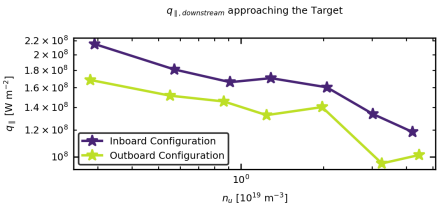

Figure 3.26: Downstream heat flux $q_{\parallel,down}$ scaling for the outboard and inboard configurations.

To observe the relative impact of charge exchange and ionization, the mean volumetric reaction rates in the island as $R_{ion} = nn_H\langle\sigma v\rangle_{ion}$ and $R_{cx} = nn_H\langle\sigma v\rangle_{cx}$ are obtained.The ionization reaction rate remains of the same order of magnitude for the whole density build-up considered and shows a similar qualitative trend of f_{pow}. The difference is that once it reaches the $n_{sep} \gtrsim 1.75e19\ m^{-3}$ threshold it has a plateau for the Outboard case. The Inboard case has a higher reaction rate, even

though their values remain pretty close, with a maximum increase of $\frac{R_{ion,In}}{R_{ion,Out}} \approx 1.5$. At low densities, charge exchange reaction rate is lower than the ionization one and very similar between the two cases until $n_{sep} \gtrsim 1.75e19\ m^{-3}$. After this value of n_{sep}, charge exchange is up to 3.5 higher in the Outboard case, suggesting to be the leading order change in the two configurations. The precise interplay between charge exchange (CX) and ionization remains to be fully elucidated. However, it is hypothesized that a concave target geometry enhances neutral trapping, which drives a pronounced increase in the ionization rate (R_{ion}) as the divertor plasma transitions to a regime opaque to neutrals ($n_{sep} \gtrsim 1.75e19\ m^{-3}$). Furthermore, CX interactions may exacerbate this trapping via toroidal momentum transfer, thereby triggering a positive feedback loop characterized by a coupled increase in local density, ionization, and CX events.

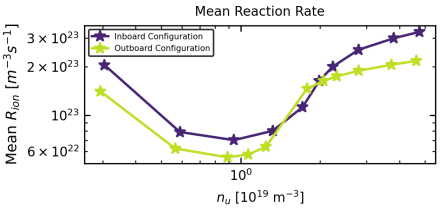

Figure 3.27: Mean island ionization reaction rate R_{ion} scaling for the outboard and inboard configurations.

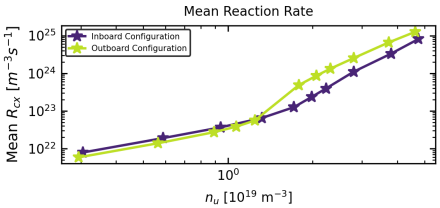

Figure 3.28: Mean island CX reaction rate R_{cx} scaling for the outboard and inboard configurations.

To check if charge exchange and target concavity is what influences the difference in build-up, the outboard and inboard reference cases are simulated again without charge-exchange reactions between neutrals and plasma.

Differences in the build-up still appear without charge exchange but is reduced, with a maximum of $\frac{n_{d,Out}}{n_{d,In}} \approx 1.5$ at $n_{sep} \approx 2.3\ m^{-3}$. However, since they are not the same, charge-exchange is not the only player in this difference, with the remainder being possibly attributed to $1/R$ effects. In line with the statement that CX is important to retain the neutrals for density build-up, we clearly can see that build-up is severely hindered by the absence of charge-exchange, with $\frac{n_{d,reference}}{n_{d,no-cx}} \geq 5$ and $\frac{T_{d,reference}}{T_{d,no-cx}} \leq 0.5$ at $n_{sep} \approx 5e19\ m^{-3}$.

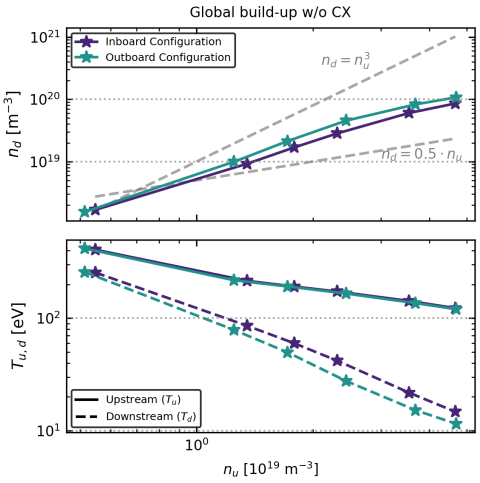

Figure 3.29: Density and temperature scalings for the outboard and inboard configurations without charge-exchange.

Also, in the configuration without charge-exchange, the downstream density and temperature curves do not reconverge at $n_{up} \gtrsim 3e19\ m^{-3}$ like in the previous cases. This is probably because, despite the high separatrix densities, T_d is still

above 10 eV, making the reaction rate for ionization $\langle \sigma v \rangle_{ion}$ still dominant, making the threshold for reconvergence between the outboard and inboard cases based on downstream temperature rather than upstream density. Without charge-exchange, f_{pow} does not reach more than 10% through the whole set of simulations, showing the importance of it in neutral power exhaust and neutral-plasma interaction.

Considering the above results we can reformulate our hypothesis: in sheath-limited regime, neutrals have a mean free path that is greater than the characteristic length of the island and neutrals mainly ionize in the core. Target shape does not affect this regime and values are similar between configurations. As density increases, mean free path of neutrals decreases. Ionization starts to happen near the target. At the same time, charge exchange reaction rate inside the island starts to become greater than the ionization reaction rate.

In a concave geometry, neutrals start to get the tangential speed and direction of the plasma ions, moving parallel towards the target, accumulating. This could lead to a chain reaction, where increasing neutral retention increases power loss and as a consequence plasma density increases, plasma temperature drops at the target, further increasing neutral retention. In a convex target neutral retention would be worse, while no effect on neutral retention would be made by a flat target case. Indeed, some remaining impact from total flux expansion is possible on the different configurations. During conduction-limited regime and diffusion limited regime this causes the difference in build-up between the cases. As downstream temperature starts to approach $T_d \lesssim 10\ eV$, ionization starts to saturate due to low temperatures decreasing the reaction rate. Difference between the cases becomes again negligible.

Chapter 4

Analysis

In this chapter, local density build-up is evaluated on a fieldline for each configuration simulated in Section 3.2.2. The rationale of the STPM is used to analyze the differences in each configuration and provide a possible explanation. Finally, an onion-skin STPM is used to compare the analytical model with the simulation results and assess the validity of the STPM.

4.1 Local density build-up

In order to perform a local analysis, fieldlines are selected. The fieldlines passing through the target points, Fig. 4.1, at $\phi = 70.9°$ are chosen for every configuration. The selected fieldlines hit the target plate at either $\phi = 71.3°$ or $\phi = 72°$. Target downstream conditions are taken in this range, where the the target is at the maximum penetration depth in the island. Here, the peaks in maximum and average plasma density are present and most of the plasma-wall interaction is observed in the simulations.

In this section, density build-up is shown similar to Chapter 3, but here the build-up is obtained considering the local upstream and downstream quantities on a single fieldline, similarly to what is done in the STPM, Section 2.2.3. The local build-up is evaluated on a field-line in the Power-Carrying Layer (PCL) (see Sec. 3.2.2). In every configuration this is the fieldline passing through the target point that is closest to the separatrix, Fig. 4.1. n_u and T_u are taken at the fieldline stagnation point, around the island midplane. The toroidal position of the stagnation point depends

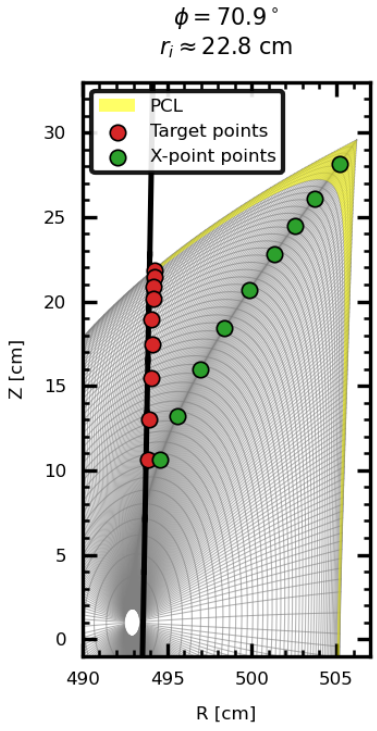

Figure 4.1: Representative cross-section with the points from which the field lines are selected (red dots), with their relative X-points (green dots) and the highlighted PCL (yellow).

on the single fieldline. n_d and T_d are taken at the target location, in the toroidal interval ($\phi \sim 71.3° - 72°$), where the fieldline hits the target.

Fig. 4.2 shows that for this local analysis increasing island size still improves density build-up. When comparing island configurations with the same size, the decreased ι' case (the one with the lower Θ) offers the best performance in terms of density build-up, T_d drop and $T_u - T_d$ difference. Also when comparing islands of the same size, differences in build-up are exacerbated with increasing r_i. However, whether this is due to r_i or to the increasing difference in Θ between bigger configurations is yet to be assessed. Within the investigated parameter range, increasing r_i continuously enhances density build-up without any observed saturation. Future studies should explore even larger island configurations to determine if and when a saturation effect in size eventually occurs.

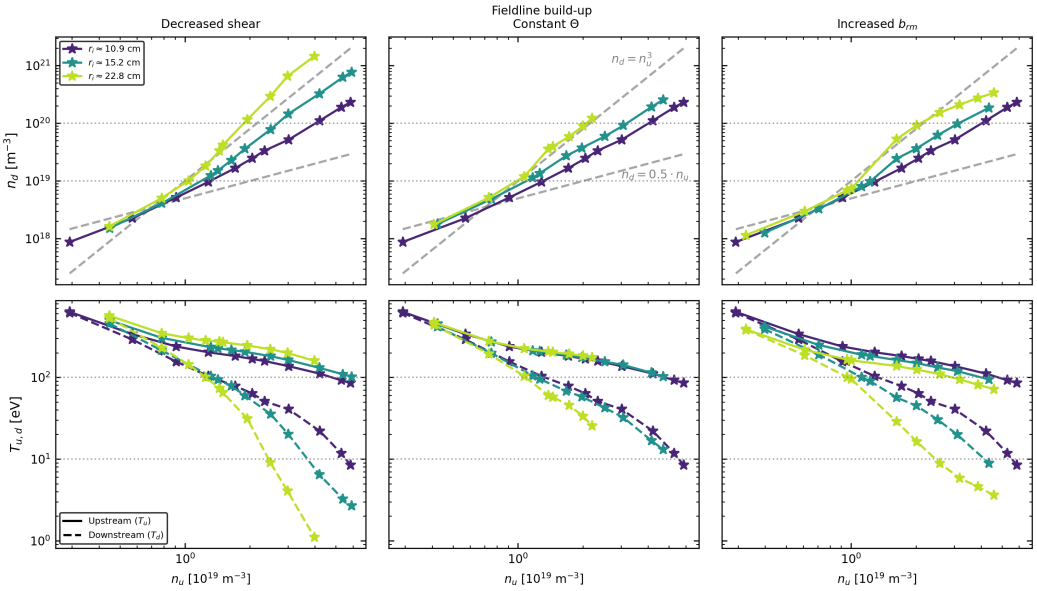

Figure 4.2: Comparison of field line density and temperature scalings in the different r_i and Θ cases.

To understand why the effect of Θ on build-up is different when considering a local fieldline instead of the global island behaviour, the three configurations with $r_i \approx 22.8\,cm$ are compared, while using the STPM framework.

In the STPM, the main input parameters that have an impact on the plasma behaviour upstream and downstream of the field line, for a given upstream density n_u, are: the connection length L_c; the field line pitch Θ; the parallel heat flux along the fieldline $q_\parallel$; the momentum loss factor f_{mom}; the convected power fraction f_{conv}; the target-localized power dissipation fraction f_{pow}. The last two terms are introduced in the STPM in [76], where an extension of the STPM model is done, including these parameters already used by [28] for the tokamak TPM.

In the TPM, f_{mom} is defined using the ratio of total pressures [111]:

$$1 - f_{mom} = \frac{p_d^{tot}}{p_u^{tot}} \tag{4.1}$$

Where p_d^{tot} and p_u^{tot} are to total pressure downstream and upstream of the fieldline respectively.

Using its definition, f_{mom} is obtained in the simulation for each configuration fieldline, Fig. 4.3. For the sake of comparison, as the magnitude of momentum losses is dependent mainly on T_d in f_{mom} parameterizations made for both tokamaks [111] (where f_{mom} is mainly driven by plasma-neutral friction [112]) and stellarators [113] (where f_{mom} is hypothesized to be mainly driven by adjacent counter-streaming flows and cross-field transport), values of f_{mom} computed from the simulations are plotted with respect to T_d instead of the usual n_u.

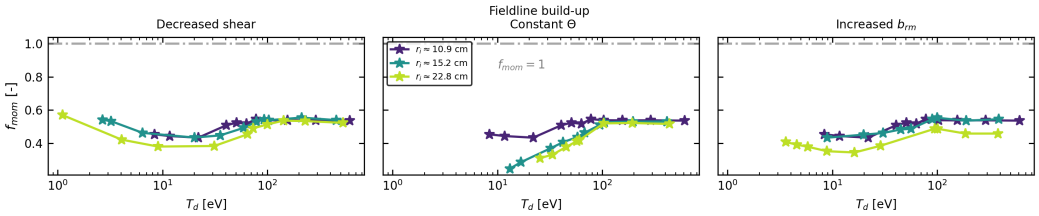

Figure 4.3: momentum loss factor f_{mom} scalings in the different r_i and Θ cases.

When comparing configurations, f_{mom}, does not show significant changes in the different configurations. Increasing Θ slightly reduces f_{mom} in larger islands. f_{mom} is seen to always decrease with increasing island size r_i. This is consistent with the Mach number plots, Fig. 3.13, where the Mach number is seen to diminish with increasing r_i, possibly leading to reduced counter-streaming flows momentum losses. Mach number is observed to decrease with decreasing Θ, Fig. 3.12. However, a more significant drop of $f_{mom} \lesssim 0.3$ in the constant Θ configurations with increasing r_i is observed. For varied field line pitch, both cases (increased b_{rm} & decreased ι') behave similarly.

A hypothesis for this is that f_{mom} is mainly driven by two phenomena: adjacent counter-streaming flows and $\perp$ cross-field transport. In this way, while f_{mom} increases due to stronger counter-streaming flows in the increased b_{rm} case, Fig. 3.12, it also decreases because of $\perp$ cross-field transport. On the contrary, in the decreased ι' case, f_{mom} is reduced due to weaker counter-streaming flows and increases due to higher flux surface

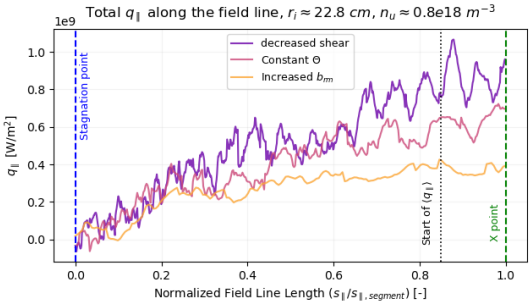

Figure 4.4: heat flux $q_\parallel$ profile along a field line from the stagnation point to the X-point for the three $r_i \approx 22.8$ cm cases.

$\perp$ transport, resulting in the two configurations having a similar final f_{mom}. In [29], counter-streaming flows momentum losses are assumed to have a relationship of $f_{mom} \propto T_d^{-0.5}$ with the downstream temperature. The f_{mom} values computed here do not follow this fit, meaning that, either in EMC3-EIRENE or in this simplified geometric configuration, counter-streaming flows may not be the dominant source of momentum losses for field lines in the PCL. Finally, the computed f_{mom} does not seem to be the driver in the differences in build-up between the different $r_i \approx 22.8\ cm$ configurations.

For the other STPM quantities of interest, it is observed that by varying Θ in these configurations, also $L_c \propto \frac{1}{\Theta}$ and $q_{\parallel}$ vary. In every simulation, $q_{\parallel}$ is at a minimum at the stagnation point of the fieldline. As the fieldline travels along the LCFS, power is deposited via perpendicular transport from the core to the island fieldline in the PCL. Upstream $q_{\parallel}$ is hence evaluated at the X-point. To minimize the influence of numerical noise and change in total flux expansion ($\propto B$) along the fieldline, the reported $q_{\parallel,u}$ values are taken as a spatial average over the final 15% of the field line length approaching the X-point, Fig. 4.4, where the parallel heat flux profile exhibits a plateau.

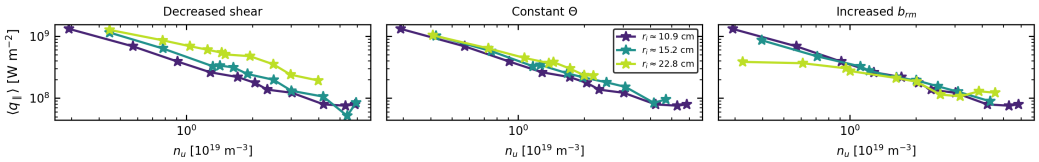

Figure 4.5: upstream heat flux $q_{\parallel,up}$ scalings in the different r_i and Θ cases.

Total heat flux along the fieldline, evaluated in this way as the sum of conducted and convected heat flux, $q_{\parallel} = q_{\parallel,cond} + q_{\parallel,conv}$, is observed to slightly increase with island size and significantly change depending on field line pitch, Fig. 4.5.

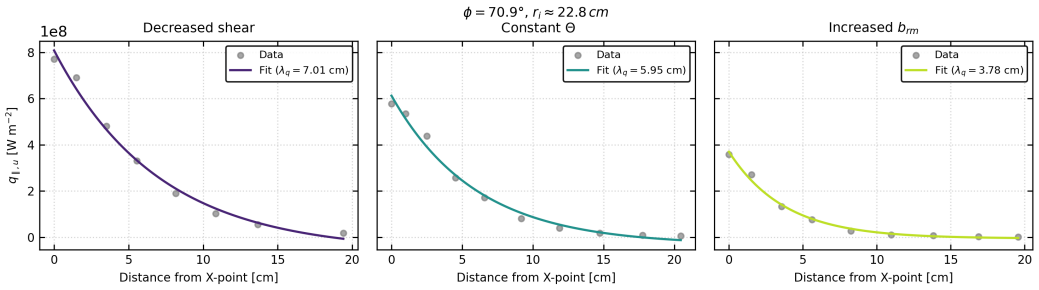

Figure 4.6: Exponential fit of the upstream heat flux profile across island flux surfaces.

This result could be explained from basic SOL physics. When considering a simple 2D SOL, geometrically, the parallel heat flux $q_{\parallel}$ along a field line is related to

the poloidal heat flux, q_{pol}, via the field line pitch Θ, such that $q_{\parallel} \propto q_{pol}/\Theta$. For a constant total heating power entering the SOL, the immediate expectation is that a decrease in Θ should lead to a higher $q_{\parallel}$, as observed. However, this purely geometric scaling is hindered by the effect Θ has on q_{pol} itself. The poloidal heat flux and the power fall-off length λ_q are inversely related, meaning $q_{pol} \cdot \lambda_q \sim$ constant.

In a 2D SOL approximation, λ_q scales with the square root of the parallel transit time $\lambda_q \propto \sqrt{\tau_{\parallel}}$, which depends on the connection length, $\tau_{\parallel} \propto L_c \propto 1/\Theta$. A lower Θ increases the connection length up to the X-point, allowing more time for $\perp$ transport to broaden the upstream heat flux profile inside the island, thereby increasing $\lambda_q \propto 1/\sqrt{\Theta}$ at the X-point. This partially mitigates the expected increase in $q_{\parallel}$, yielding:

$$q_{\parallel} \propto q_{pol}\frac{1}{\Theta} \propto \frac{1}{\sqrt{\Theta}} \tag{4.2}$$

In order to check the dependence of λ_q and $q_{\parallel}$ to field line pitch, a comparison between the three $r_i \approx 22.8\,cm$ island configurations is performed. Firstly, To see if the simple 2D SOL approximation of $\lambda_q \propto \frac{1}{\sqrt{\Theta}}$ is respected in the 3D SOL of these simulations, λ_q is extrapolated and compared. A upstream heat flux profile is obtained by computing $q_{\parallel,u}$ values radially along the island, from X-point to O-point, Fig. 4.6, using the field lines passing through the target points, Fig. 4.1. The profiles are fitted using a standard exponential decay model:

$$q(x) = q_0 \exp\left(-\frac{x}{\lambda_q}\right) \tag{4.3}$$

λ_q is extracted employing a non-linear least squares optimization algorithm (Levenberg-Marquardt) [114]. The relationship of λ_q with Θ is hypothesized to follow a power-law scaling and it is linearized by taking the natural logarithm of both sides:

$$\ln(\lambda_q) = n\ln(\Theta) + \ln(C) \tag{4.4}$$

Where n is the scaling exponent (or power-law index). It represents the slope of the fitted line, Fig. 4.8. C is the proportionality constant of the scaling law. $\ln(C)$ represents the y-intercept, Fig. 4.8. An ordinary least squares (OLS) linear regression [114] is then performed on the log-transformed dataset. Indeed, the power fall-off length shows a dependence on field line pitch of the order $\lambda_q \propto \Theta^{-0.4}$.

To see if also the simple 2D SOL approximation of $q_{\parallel} \propto 1/\sqrt{\Theta}$ is respected in the 3D SOL of these simulations, also $q_{\parallel}$ is compared for the $r_i \approx 22.8\ cm$ island configurations, using the same power-law scaling as above. Indeed, the parallel heat flux shows a dependence on field line pitch of the order $q_{\parallel} \propto \Theta^{-0.5257}$, Fig. 4.7, consistent with Eq. 4.2. The changing Θ in the different same size configurations is observed to change $q_{\parallel}$. This could impact the local build-up, effectively explaining the unexpected performance of the decreased ι' cases.

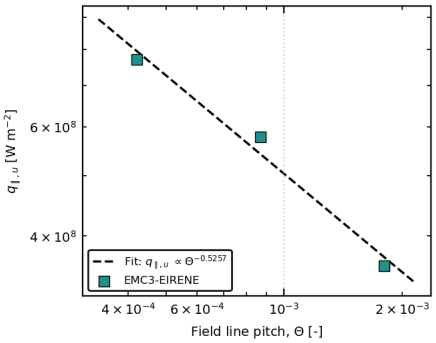

Figure 4.7: $q_{\parallel,up}$ power law scaling with respect to Θ for the $r_i \approx 22.8\ cm$ cases.

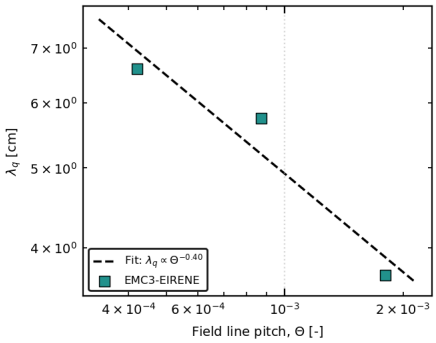

Figure 4.8: λ_q power law scaling with respect to Θ for the $r_i \approx 22.8\ cm$ cases.

Now, the impact of the remaining f_{conv} and f_{pow} input parameters in the different configurations is showed. We take into account the convected fraction of the total parallel heat flux with f_{conv}. The conductive heat flux, relevant for the Spitzer-Härm conduction in the TPM, becomes $q_{\parallel,cond} = (1 - f_{conv})q_{\parallel}$ and Eq. 2.20 becomes:

$$T_u^{7/2} = T_d^{7/2} + \frac{7(1 - f_{conv})q_{\parallel}L_c}{2\kappa_e} - \frac{7\chi(n_u + n_d)}{4\kappa_e\Theta^2}(T_u - T_d) \tag{4.5}$$

Volumetric energy dissipation via radiation and ionization losses close to the target is taken in account with f_{pow}. The heat flux downstream is now reduced to $q_{\parallel,d} = (1 - f_{pow})q_{\parallel}$. Eq. 2.22 becomes:

$$q_{\parallel} = \frac{\gamma n_d c_{sd} T_d}{1 - f_{pow}} \tag{4.6}$$

Taking into account these factors, it is possible to evaluate f_{pow} for each fieldline as:

$$f_{pow} = \frac{\int |S_{ee} + S_{ei}|\ ds}{q_{\parallel,d} + \int |S_{ee} + S_{ei}|\ ds} \tag{4.7}$$

Where $q_{\parallel,d}$ is the total parallel heat flux at the target plate and $\int |S_{ee} + S_{ei}|\ ds$ represent, integrated along the fieldline, the energy loss or gain of electrons and ions due to the neutrals in, respectively, Eq. 2.26 and Eq. 2.25. In particular, S_{ee} mostly represents ionization energy losses, while S_{ei} represent losses due to charge-exchange. It should be noted that this formulation of the power dissipation fraction does not account for the $\perp$ transport losses along the flux tube, which may actually play a relevant role. Since impurities have not been considered in these simulations, and because most of the plasma-neutral interaction happens at the target location towards the O-point, the resulting f_{pow} for the fieldline in the PCL is below 0.1, Fig. 4.9. However, at upstream densities $n_u > 2e19\, m^{-3}$, $f_{pow} > 0.01$ for the decreased ϵ' cases. This may be due to the observation in Chapter 3 that the density peak region shifts towards the separatrix as field line pitch decreases, leading to increased plasma-neutral interaction in the PCL fieldline.

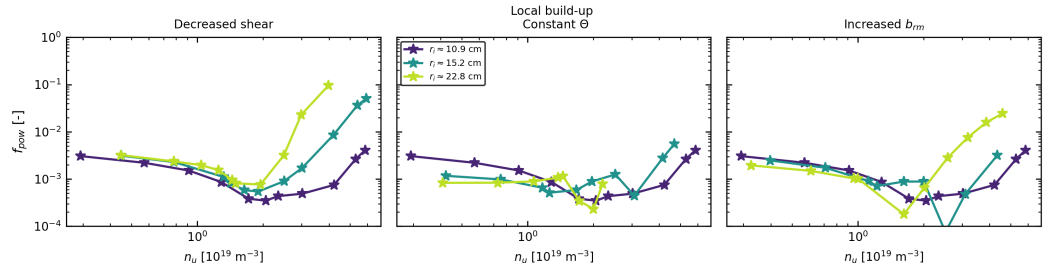

Figure 4.9: Target-localized power dissipation factor f_{pow} scalings in the different r_i and Θ cases.

Last but not least, the convected power fraction is computed as $f_{conv} = \frac{q_{\parallel,conv}}{q_{\parallel,cond}+q_{\parallel,conv}}$ at every point of the field line from the X-point to the target plate. The f_{conv} shown for each configuration, Fig. 4.10, is obtained by taking the average $\langle f_{conv} \rangle_{X-point\,to\,Target}$ of the convected power fraction computed at those points. No significant differences in f_{conv} is found for the different configurations analyzed. This is an unexpected result, given the observed impact of r_i and Θ on the Mach number 2D distributions (Figs. 3.12 & 3.13). With such varying Mach profiles, correspondingly different f_{conv} values were expected, making this a focus for future studies.

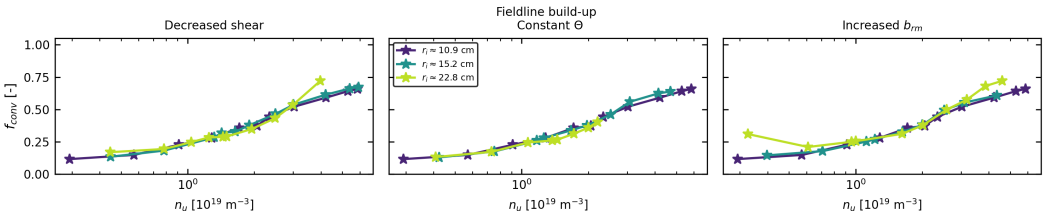

Figure 4.10: Convected power fraction f_{conv} scalings in the different r_i and Θ cases.

So far, the only STPM parameter that shows a significant change between same size configurations is $q_{\parallel}$. It has been shown [76] how increasing $q_{\parallel}$ is beneficial for n_d in the higher n_u density range, while a decrease in Θ and a consequent increase in L_c shifts the transition to the conduction-limited regime to lower n_u. From the STPM point of view, the increase in $q_{\parallel}$ could explain the overall best performance of the low Θ cases.

To confirm this, the STPM system of equations, Eqs. 4.5 & 2.21 & 4.6 is solved for the n_u profile of the local build-up for each of the $r_i \approx 22.8\ cm$ configurations. We start from a basic STPM configuration, with L_c and Θ correctly defined for each configuration, with a $q_{\parallel} = 3e8\ W/m^2$ kept constant between configurations, with a $f_{mom} = \alpha/T^{1/2}$ (in these calculations, $\alpha = 2$ is chosen) parametrization for the momentum loss factor taken from [85] and without volumetric loss factors f_{pow} and f_{conv}.

Afterwards, all of the parameter profiles obtained and discussed above in this

section (f_{mom}, $q_{\parallel}$, f_{pow}, f_{conv}) are added and removed from the equations, in order to see which one impacts in creating the performance difference between configurations.

The STPM correctly replicates the results of same size configurations with different Θ when the downstream heat flux profile $q_{\parallel,down}$ taken from simulations is used as the $q_{\parallel}$ input parameter and the same $f_{mom} = 2/T^{1/2}$ of the basic configuration is used for the momentum loss factor. On a field line level, the changing heat flux with changing Θ explains the differences between the build-up in different configurations.

It is observed that as Θ decreases, heat flux $q_{\parallel}$ and connection length L_c increase, leading to a more favorable conduction limited regime in the n_u upstream density range studied. In addition to that, the STPM correctly predicts the profiles and difference when the downstream heat flux is used, instead of the upstream one. This highlights the need of using a model that takes into consideration the flux surface $\perp$ losses that happen between the upstream and downstream locations, moving heat and particles from the PCL field lines into the PFR and far SOL field lines. This condition will be analyzed further in Sec. 4.2.

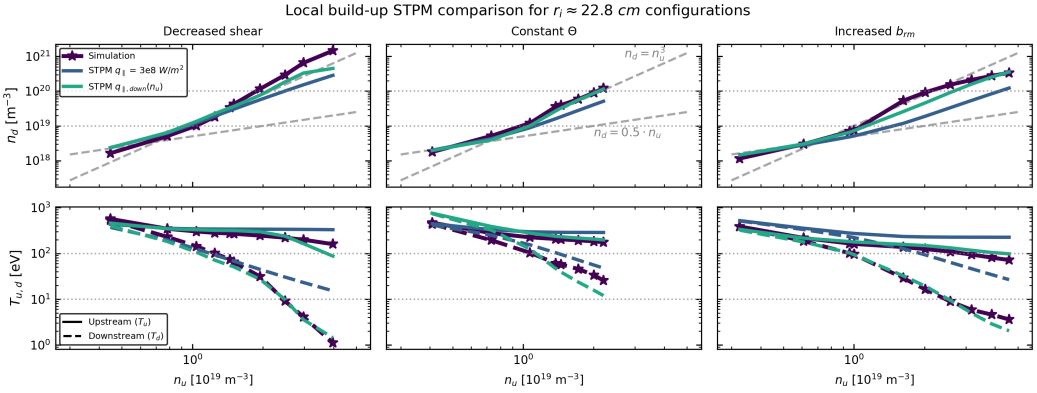

Figure 4.11: Field line density and temperature scalings for the $r_i \approx 22.8$ cm cases and their STPM predictions.

In this section, the local density build-up in the PCL field lines has been analysed using the tools of the STPM. Increased island size r_i always leads to improved density build-up. For the various cases, it is observed how an increased size leads to a reduction of momentum losses f_{mom}, likely due to less intense counter-streaming flows. Increased size also increases target-localized power dissipation f_{pow} at higher upstream densities, $n_u \gtrsim 1e19\ m^{-3}$. By expanding the island width, the divertor's ability to screen neutrals is enhanced, leading to more charge-exchange and ionization reactions inside the island.

When comparing islands with the same size, the ones obtained by decreasing magnetic shear ι' perform better than the others in terms of build-up. This is an unexpected result, in contradiction with the global build-up results of Sec. 3.2 and with the literature [29]. Despite having a lower Θ and higher L_c, which hinder density

build-up in the STPM, a lower Θ has been found to yield a higher $q_{\parallel}$. In addition to that, lower Θ is observed to have its density peaks closer to the separatrix at high densities $n_u \gtrsim 1.5e19\ m^{-3}$. This increases f_{pow} for the field lines in the PCL in the decreased ι' case.

Importantly, $q_{\parallel}$ is found to be the parameter that improves build-up in the decreased ι' configurations (decreasing Θ). A good prediction of the density build-up on $r_i \approx 22.8\ cm$ island size configurations is obtained using the STPM. However, because the results are obtained without a fundamental understanding of the momentum loss f_{mom} scaling and, in general, a proper, self-consistent, treatment of flux surface $\perp$ losses, the model cannot be reliably extrapolated to other configurations.

4.2 STPM Onion skin method

In this section, the capabilities of the Stellarator Two Point Model are tested by estimating the target profile densities and temperatures. An Onion-Skin [115] STPM model is applied and results are compared with simulations.

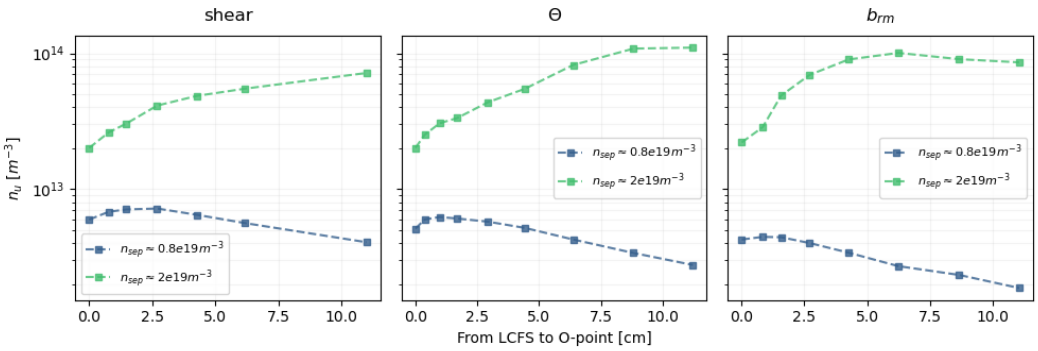

Figure 4.12: Upstream density n_u profiles, used as input for the STPM-OSM.

The integrated STPM model, Eq. 2.20, 2.21, 2.22, is used for each configuration and compared with the computed values. For each configuration, two different values of separatrix density n_{sep} cases are considered. One low density case ($n_u = 0.8e19\ m^{-3}$) and one high density case ($n_u = 2e19\ m^{-3}$) for each configuration. For each field line in Fig. 4.1, values of L_c, Θ, n_u, Fig. 4.12, and $q_{\parallel}$, Fig. 4.13 are taken as input parameters for the STPM model.

At low n_{sep} and in attached conditions, Fig. 4.13, we observe how the downstream heat flux value at the PCL is lower than the upstream one and increased in the field lines far from the separatrix. This is probably due to flux surface perpendicular transport, that directs particles and energy into the PFR and far SOL. As this perpendicular transport is not accounted for in the STPM, we check the potential sensitivity that this additional 'power source' for a far SOL field line could have conservatively by solving the STPM for two different $q_{\parallel}$ profiles. First, the upstream

$q_{\parallel,u}$ evaluated at the X-point is used. Secondly, the downstream $q_{\parallel,d}$ evaluated at the target is used. From the point of view of the upstream temperature T_u, Eq. 4.5, using the downstream heat flux is justified as steeper gradients are expected near the target. From the point of view of the downstream parameters n_d and T_d the same downstream heat flux is justified by using the target boundary conditions, Eq. 4.6. This downstream bias only becomes problematic for evaluating T_u if localized power losses (f_{pow}) at the target are highly significant. Furthermore, f_{pow} is not expected to to have an impact in these simulations, Fig. 4.9, as no impurities were included.

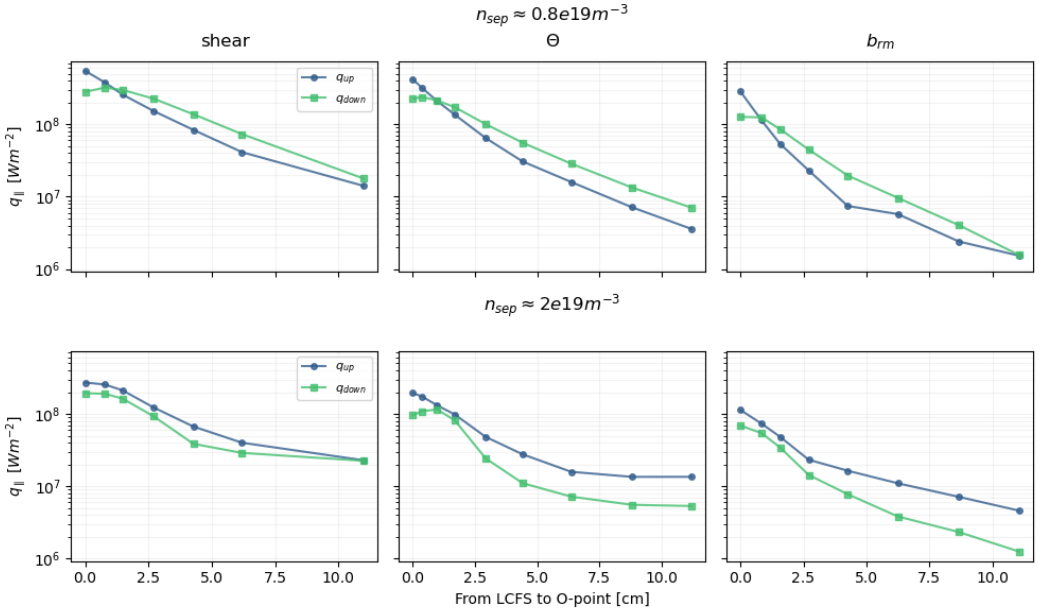

Figure 4.13: Upstream $q_{\parallel,up}$ and downstream $q_{\parallel,down}$ heat flux profiles, used as input for the STPM-OSM.

The STPM system of equations without volumetric correction factors, f_{conv} and f_{pow}, is numerically solved. A parametrization $f_{mom} = \alpha/T_d^{1/2}$ [85] is used for the momentum loss factor, with $\alpha = 2$. For each fieldline $T_{e,u}$, $T_{e,d}$, n_d are obtained. In this way it is possible to obtain an approximation of the conditions along the target by solving each field line individually in a "onion skin" fashion [116]. No cross-field transport is taken into account. The resulting target profile quantities are then compared with the ones from the simulations.

In the $n_{sep} = 0.8e19\ m^{-3}$ case, Fig. 4.14-4.16, the STPM using both $q_{\parallel,u}$ and $q_{\parallel,d}$ overpredicts the simulated upstream temperature, T_u, profile by a factor of $\frac{T_{u,STPM}}{T_u} \approx 2$. In both cases, the decrease in T_u with increasing Θ of the simulations is reproduced by the STPM. Using $q_{\parallel,d}$, the qualitative profile is well reproduced.

The STPM using $q_{\parallel,u}$ overpredicts the downstream temperature T_d towards the separatrix, while underpredicting it towards the O-point, with a maximum difference of $\left.\frac{T_{d,STPM}}{T_d}\right|_{max} \approx 0.5 - 2$.

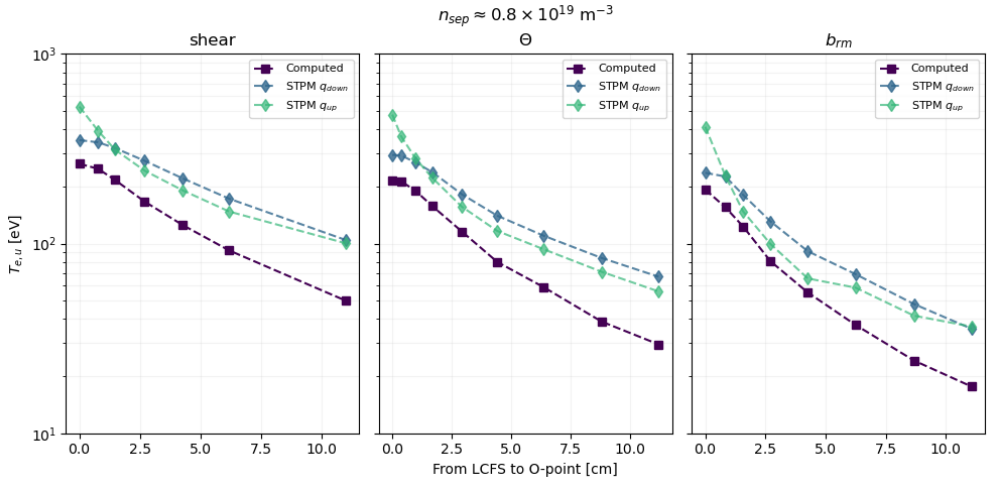

Figure 4.14: T_u profiles and their STPM-OSM predictions (low n_{sep}).

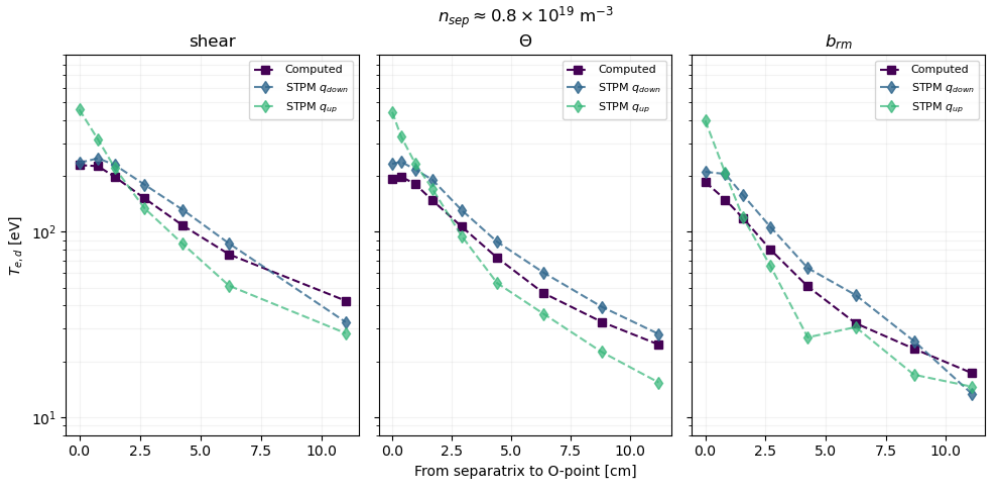

Figure 4.15: T_d target profiles and their STPM-OSM predictions (low n_{sep}).

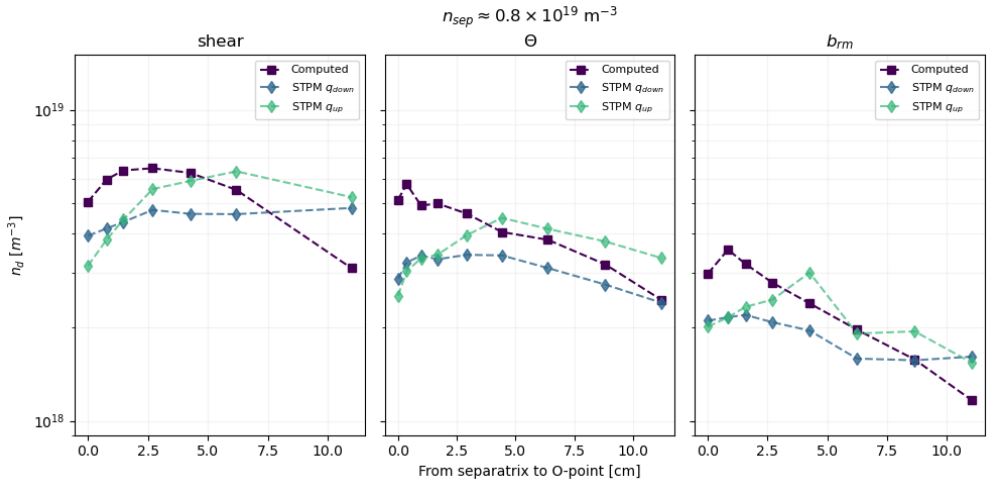

Figure 4.16: n_d target profiles and their STPM-OSM predictions (low n_{sep}).

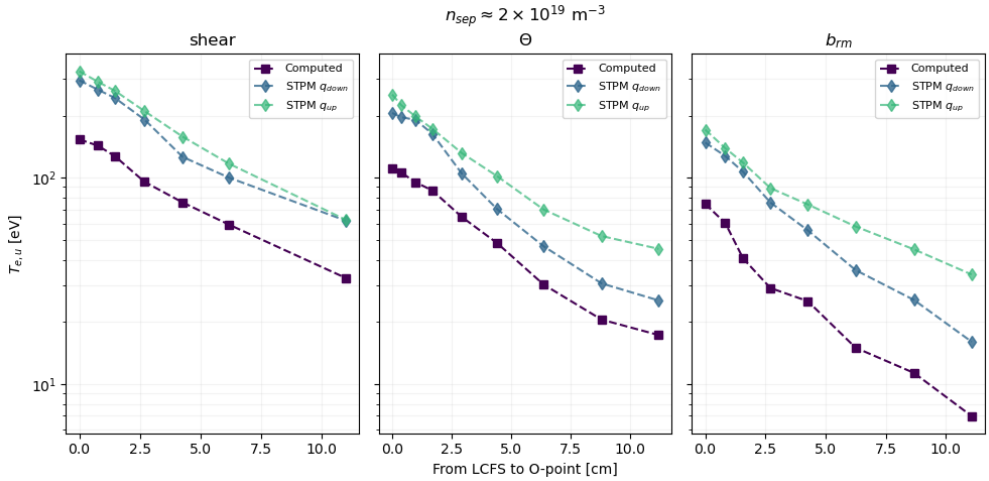

Figure 4.17: T_u profiles and their STPM-OSM predictions (high n_{sep}).

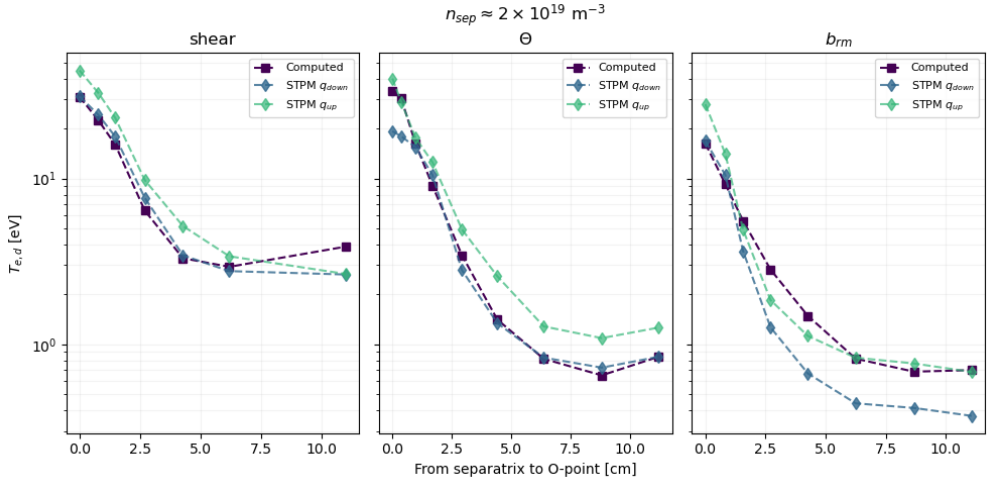

Figure 4.18: T_d target profiles and their STPM-OSM predictions (high n_{sep}).

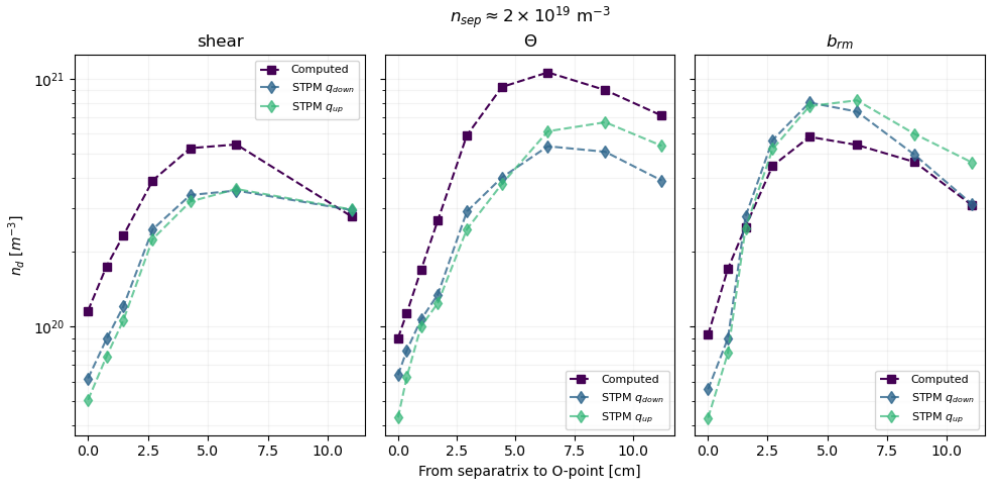

Figure 4.19: n_d target profiles and their STPM-OSM predictions (high n_{sep}).

The STPM using $q_{\parallel,d}$ overpredicts the temperature profile by $\frac{T_{d,STPM}}{T_d} \lesssim 1.5$ throughout the profile. Overall, the qualitative temperature profile is well reproduced when the downstream heat flux is used.

The target density, n_d, profiles shapes are not correctly reproduced in both cases. The overall decrease in target density with increasing Θ is reproduced.

In the $n_{sep} = 2e19\ m^{-3}$ case, Fig. 4.14-4.16, both $q_{\parallel,u}$ and $q_{\parallel,d}$ cases overpredict T_u by a factor of $\frac{T_{u,STPM}}{T_u} \approx 2$. The STPM with $q_{\parallel,d}$ still returns the simulated target profile qualitatively.

T_d is well approximated by the STPM. There is not much difference in this case between using $q_{\parallel,u}$ or $q_{\parallel,d}$, but $q_{\parallel,d}$ approximates the simulated results slightly better, both quantitatively and qualitatively.

n_d is mostly underpredicted, by a factor of $\frac{n_{d,STPM}}{n_d} \approx 0.5$. Density peaks on the target are well predicted by the STPM. $q_{\parallel,d}$ still performs slightly better than $q_{\parallel,u}$. Overall, downstream quantities are well approximated by the model.

The next step in future studies would be to asses which single parameter used in the STPM mainly causes the differences between configurations and the discrepancies with the simulated results.

In conclusion, the STPM onion-skin model used here is able to correctly predict qualitative profiles of density and temperature. The STPM OSM returned these results with a considerable amount of input information: the L_c, Θ, $q_\parallel$ and n_u profiles. The agreement is within a factor of 2 with the simulation, with a tendency to underpredict the target density and overpredict the upstream temperature with the STPM. Using $q_{\parallel,d}$ returns better results than using $q_{\parallel,u}$. This is probably due to the fact that, between the upstream and downstream locations, flux surface $\perp$ transport moves heat and particles from the PCL field lines into the PFR and far SOL field lines.

Since this is not accounted for in the STPM, directly using the upstream $q_{\parallel,u}$ yields higher temperatures and lower densities than expected from simulations. This is more visible at low separatrix densities $n_{sep} = 0.8e19\ m^{-3}$, where the heat flux depends more on the power coming from the LCFS upstream than the sources. At higher densities (e.g. $n_{sep} = 2e19\ m^{-3}$) the difference is less pronounced. The STPM is able to correctly predict the changes in temperature and density due to the different configurations having a different Θ.

The STPM yields good results, also considering that it has been applied to cases with extreme island sizes and two of them being in the neutral-transparent O-point regime. At low densities, the STPM correctly predicts the trend in simulation of a decreasing n_d with increasing Θ. At high densities, the STPM predicts a monotonically increasing target density with increasing Θ. This is not observed in simulations, where the neutral-transparent O-point regime hinders the open divertor performance, with the constant Θ configuration having the best build-up, while the decreased ι' and the increased b_{rm} cases have a similar density build-up, with respectively a

higher T_u and T_d and a lower T_u and T_d.

Finally, flux surface $\perp$ transport, and the significant redistribution of sources and sinks in the neutral-transparent O-Point cases are not taken into account by the STPM model, other than by using $q_{\parallel,up}$ and $q_{\parallel,down}$. The agreement with the STPM is surprisingly good and will have to be understood in the future in more detail. We refrain from clear conclusions on the STPM capability to reliably 'predict' field line quantities within factors of 2. Without a fundamental understanding of the momentum loss f_{mom} scaling and, in general, a proper, self-consistent treatment of volumetric losses (f_{mom},f_{conv},f_{pow}) and flux surface $\perp$ losses, the model cannot be reliably extrapolated to other configurations.

Chapter 5

Conclusion & Outlook

5.1 Conclusion

Stellarator-based fusion reactors offer a compelling pathway to steady-state operation and commercial energy production. However, power exhaust is a challenge for future devices. The management of the intense power and particle fluxes that exit the confined plasma are a prerogative for a fusion reactor, as unmitigated localized heat loads can easily exceed the engineering limits of $10 - 15\ MW/m^2$ of plasma-facing components [32]. To address this, the island divertor has emerged as a leading power exhaust solution [106]. While stable detachment has been successfully achieved in present day devices like Wendelstein 7-X (W7-X), extrapolating these scenarios to a reactor-scale stellarator requires substantially higher divertor densities, which remains a primary operational challenge for current island divertors [86].

Island geometric parameters, such as field line pitch Θ and island radial width r_i have been observed to significantly impact density build-up [29] and detachment performance [68, 92] in the island divertor. Real stellarator devices, like W7-AS or W7-X, are characterized by complex 3D magnetic geometries. Optimizing the island divertor performance in these machines requires the dissection of many convoluted geometric effects.

This thesis set out to understand how the geometric parameters of magnetic islands dictate divertor performance and density build-up. By utilizing the Hamiltonian Grids (HaGrids) code package [104], it was possible to generate simplified magnetic geometries, Fig. 2.8 & 2.10, for the island divertor, where resonant surfaces are artificially selected and the island field line pitch Θ and radius r_i, can be arbitrarily chosen via changing the geometry magnetic shear ι' and resonant magnetic perturbation amplitude b_{rm}. To isolate the impact of these individual variables, we conducted an extensive computational analysis. Starting from a reference configuration, made with the same characteristics of W7-X, seven distinct magnetic configurations are generated, Fig. 3.1, encompassing varying island sizes and field line pitches, Sec. 3.1. These configurations were subsequently simulated using the fully 3D self-consistent

edge plasma and neutral transport code, EMC3-EIRENE, Sec. 3.2. The principal conclusions drawn from this are the following:

- Island size r_i can be increased by either increasing b_{rm}, decreasing magnetic shear ι' or a combination of both. Each method yields different Θ values for the same increase in r_i, Tab. 3.1. The method with which the island size is increased can vastly change the transport dynamics.

- Global density build-up, which is evaluated considering both the maximum and the pressure weighted average downstream density, increases monotonically with island size r_i independent of the field line pitch Θ, Fig. 3.16. The best results in terms of maximum build-up are obtained when Θ is maintained constant, Fig 3.9. As expected [29], decreasing ι' (lower Θ) to increase r_i yields a lower increase in global build-up, because of a decrease in Θ.

- A novel plasma mode in the island divertor, referred to in this thesis neutral-transparent O-point regime, is observed. Increased island size, r_i, or $\parallel$ / $\perp$ transport ratio, i.e. Θ, both lead to less power/particles reaching the O-point, starving it of power for sustaining a plasma. As upstream density increases, the recycled neutrals ejected from the plate travel further into the island and into this neutral-transparent volume. Instead of ionizing near the target plate, they now ionize at the border of this volume with the plasma, Fig. 3.14. In an open divertor configuration, this creates a low temperature plasma and neutral dense volume surrounding the island O-point, Fig. 3.11 & 3.9. After the plasma enters this neutral-transparent O-point regime, increasing Θ and r_i saturates the density build-up at the target. In order to obtain the best possible density build-up, one has to find a trade-off between island size and field line pitch, Fig. 3.16.

Subsequently, the local build-up, obtained considering the local upstream and downstream quantities on a single fieldline in the power carrying layer (PCL), is analyzed for the different r_i and Θ configurations discussed above, Sec. 4.1. The results were the following:

- Increasing island size r_i always leads to a monotonic improvement of density build-up, Fig. 4.2, as in the global one of Sec. 3.2.

- In contradiction with the conclusions of global build-up, decreasing Θ improves local build-up between configurations with the same r_i. The best configuration in terms of build-up $n_d(n_u)$ is the one with the highest r_i and lowest Θ. We find that this is related to higher parallel heatflux density ($\propto 1/\sqrt{\Theta}$) and more favorable high recycling scaling due to higher heat flux and longer connection length.

Thirdly, the simplified geometry is used to observe the impact of target placement on the density build-up, Sec. 3.3 & 3.3.1. In the current W7-X 5/5 island chain there

are three possible stellarator-symmetric target locations around the symmetry plane: inboard, top/bottom and outboard, Fig. 3.17. Configurations with these placements are simulated using EMC3-EIRENE. The principal conclusions were the following:

- The target shadow region (TSR) is qualitatively the same in the inboard and outboard target configurations, Fig. 3.18, where one half of each target is shadowed and the other half is only partially shadowed towards the end of the plate. The top/bottom configuration has a different extent of the TSR, probably because the two target plates are not on the same/continuous island. Both target plates are partially shadowed on both halves.

  Because of this, the heat flux strike line on the targets, Fig. 3.20, in the inboard and outboard cases is mainly on one half of each target and extends for $\approx 11°$ toroidally. On the other hand, the top/bottom case strike line is equally distributed on both sides of the targets, expanding for $\approx 8°$ toroidally on each side. The top/bottom case has the lowest maximum heat flux q_{max} on the target, while the inboard case has the highest q_{max} out of the three.

- By being on two distinct and separate islands, the split targets in the top/bottom configuration lead to shorter connection length L_c steps between the two targets compared to the other two configurations, Fig. 3.19, where the targets are a full toroidal turn apart.

- Density build-up is improved at intermediate densities in the outboard target case, Fig. 3.21. A comparison between a reference configuration and a cylindrical configuration with flat targets, Fig. 3.23, strongly supports the hypothesis that the improvement is primarily attributed to target concavity, which increases neutral retention in the island, Fig. 3.22, and a lesser extent to total flux expansion ($B_\phi \propto 1/R$), Sec. 3.3.1.

Finally, to explore the capabilities of the Stellarator Two Point Model (STPM), an Onion-Skin model (OSM) [115] using the STPM is applied to the results of the three configurations with the larger island ($r_i \approx 22.8\ cm$), Sec. 4.2. The obtained results are:

- The STPM Onion-Skin model predicts the temperature (T_u,T_d) and density (n_d) target profiles within a factor of 2, with a tendency to underpredict the target density n_d and overpredict the upstream temperature T_u, Fig. 4.14 to 4.19. The qualitative profiles of these quantities and the location of the target density peaks at high densities are well-reproduced, Fig. 4.19.

- The saturation of downstream density observed at high n_u densities, as the plasma enters the neutral-transparent O-point regime, is not accounted for by the OSM, which instead predicts a monotonically increasing target density n_d with increasing Θ between configurations, Fig. 4.19.

- Using the downstream heat flux $q_{\parallel,d}$ returns better results than using the upstream heat flux $q_{\parallel,u}$, both qualitatively and quantitatively. This highlights the importance of considering flux surface $\perp$ transport between the upstream and downstream locations, Fig. 4.13. This transport is not automatically accounted for in the STPM model.
- The reliability of the STPM to predict target profiles within a factor of 2 remains uncertain. Consequently, without a fundamental understanding of the momentum loss f_{mom} scaling and, in general, without a self-consistent treatment of volumetric losses (f_{mom}, f_{conv}, f_{pow}) and flux surface $\perp$ losses, extrapolating this model to other configurations is currently unjustified.

5.2 Outlook

Based on the outcomes of this thesis, some key insights can be outlined for future island divertor studies.

It has been pointed out how changing the island size r_i through the resonant magnetic perturbation b_{rm} (via control coils) or through magnetic shear ι' effects leads to different outcomes in terms of divertor transport and should thus be both considered and treated separately in future optimization studies.

The neutral-transparent O-point regime observed in this work, along with the significant positive impact on divertor transport of increased island size r_i, should incentivize coil and magnetic island optimization to access these configurations in a real device, in order to experimentally confirm and achieve these conditions. This novel regime could also considerably aid in the design of a closed island divertor in existing or future machines.

The findings on target concavity highlight the importance of momentum transport to neutrals and neutral transport from a divertor perspective, and how these phenomena can be exploited to improve performance. The overall findings on target placement and flux expansion encourage the exploration of alternative target configurations for future devices, in addition to the consolidated top/bottom one employed in W7-X.

Lastly, if future studies can successfully generalize and validate the results obtained with the Stellarator Two Point model (STPM) Onion-Skin method (OSM), it could be utilized as a fast and efficient tool to provide edge plasma temperature and density distributions to support future divertor design and advanced modelling efforts.

Appendix A

Elliptic magnetic field calculations

Building upon the work of [104], we utilize elliptical toroidal coordinates to derive magnetic field configurations for an elliptical geometry. A primary objective of this work is to aid in the implementation of these geometries within the HaGrids framework (Sec. 2.4). First, we define the coordinate system and its fundamental relations. Next, starting from the general magnetic field formulation in Eq. 2.2, we derive an axisymmetric toroidal magnetic field configuration by specifying an appropriate form for $\theta(\mu, \nu, \varphi)$. Finally, to support drift applications, we obtain a generalized magnetic field expression for this geometry. The derivation procedure is adapted from [104], which provides further mathematical details on this topic.

A.1 Elliptic Toroidal Coordinates

To properly analyze the magnetic field geometry, we define the elliptic toroidal coordinates in terms of the standard Cartesian coordinates (X, Y, Z) as:

$$X = (R_0 + a \sinh \mu \cos \nu) \sin \varphi, \tag{A.1}$$

$$Y = (R_0 + a \sinh \mu \cos \nu) \cos \varphi, \tag{A.2}$$

$$Z = a \cosh \mu \sin \nu, \tag{A.3}$$

where a represents the distance between the center of the ellipse and one of its foci. The major radius R is consequently defined as:

$$R = R_0 + a \sinh \mu \cos \nu. \tag{A.4}$$

Additionally, we define the aspect ratio ε of the configuration as:

$$\varepsilon = \frac{a \sinh \mu}{R_0}. \tag{A.5}$$

The valid ranges for these coordinates are $\mu \in [0, \infty)$, $\nu \in [0, 2\pi]$, and $\varphi \in [0, 2\pi]$.

A.2 Area Element and Magnetic Flux

The poloidal magnetic flux ψ is related to the background magnetic field B_0 and the cross-sectional area of the ellipse. Denoting the minor and major axes of the ellipse as A and B, respectively, the flux is expressed as:

$$\psi = \text{Area} \cdot B_0 = \pi AB B_0 = \pi a^2 \sinh\mu \cosh\mu B_0. \tag{A.6}$$

By applying the double-angle identity for hyperbolic functions, this simplifies to:

$$\psi = \frac{\pi a^2 B_0}{2} \sinh(2\mu). \tag{A.7}$$

A.3 Basis Vectors and Scale Factors

Given the position vector $\vec{r} = (X, Y, Z)$, its derivatives with respect to the spatial coordinates yield the covariant basis vectors:

$$\vec{e}_\mu = \frac{\partial \vec{r}}{\partial \mu} = (a\cosh\mu\cos\nu\sin\varphi,\ a\cosh\mu\cos\nu\cos\varphi,\ a\sinh\mu\sin\nu)\,, \tag{A.8}$$

$$\vec{e}_\nu = \frac{\partial \vec{r}}{\partial \nu} = (-a\sinh\mu\sin\nu\sin\varphi,\ -a\sinh\mu\sin\nu\cos\varphi,\ a\cosh\mu\cos\nu)\,, \tag{A.9}$$

$$\vec{e}_\varphi = \frac{\partial \vec{r}}{\partial \varphi} = (R\cos\varphi,\ -R\sin\varphi,\ 0)\,. \tag{A.10}$$

The corresponding scale factors $h_i = |\vec{e}_i|$ are found to be:

$$h_\mu = a\sqrt{\cosh^2\mu - \sin^2\nu} \equiv S(\mu,\nu), \quad h_\nu = S(\mu,\nu), \quad h_\varphi = R. \tag{A.11}$$

From these, the normalized basis vectors are obtained:

$$\hat{e}_\mu = \frac{\vec{e}_\mu}{h_\mu}, \quad \hat{e}_\nu = \frac{\vec{e}_\nu}{h_\nu}, \quad \hat{e}_\varphi = \frac{\vec{e}_\varphi}{h_\varphi} = (\cos\varphi, -\sin\varphi, 0). \tag{A.12}$$

A.4 Gradient Operator and Jacobian

The gradient of a scalar function g in this coordinate system is formulated as:

$$\nabla g = \sum_{i=1}^{3} \hat{e}_i \frac{1}{h_i}\frac{\partial g}{\partial q_i}, \quad \text{for } q_1, q_2, q_3 = \mu, \nu, \varphi. \tag{A.13}$$

The Jacobian determinant of the transformation is given by the scalar triple product of the covariant basis vectors:

$$J = \det \begin{vmatrix} \vec{e}_\mu \\ \vec{e}_\nu \\ \vec{e}_\varphi \end{vmatrix} = Ra^2 \left(\cosh^2\mu\cos^2\nu + \sinh^2\mu\sin^2\nu\right) = RS^2(\mu,\nu). \tag{A.14}$$

A.5 Transformation to Canonical Coordinates

To interface with the Hamiltonian formulation, we define the relationships between the canonical variables and the toroidal elliptical coordinates as:

$$\phi = \varphi, \quad \theta = \nu + \tilde{\theta}(\mu, \nu, \varphi). \tag{A.15}$$

Evaluating the gradient of the flux ψ yields:

$$\nabla\psi = \pi a^2 B_0 \cosh(2\mu)\nabla\mu. \tag{A.16}$$

Similarly, the gradient of the canonical poloidal angle θ expands to:

$$\nabla\theta = \nabla\nu + \nabla\tilde{\theta} = \nabla\nu + \nabla\mu\partial_\mu\tilde{\theta} + \nabla\nu\partial_\nu\tilde{\theta} + \nabla\varphi\partial_\varphi\tilde{\theta}. \tag{A.17}$$

Using the properties of the basis vectors, the cross product of the gradients of μ and ν is:

$$\nabla\mu \times \nabla\nu = \frac{R}{S^2(\mu,\nu)}\nabla\varphi. \tag{A.18}$$

Substituting these into the general magnetic field representation, the magnetic field equation becomes:

$$2\pi\vec{B} = \pi a^2 B_0 \cosh(2\mu)\frac{R}{S^2}(1+\partial_\nu\tilde{\theta})\nabla\varphi + \pi a^2 B_0 \cosh(2\mu)\frac{R}{S^2}\nabla\mu\times\nabla\varphi\,\partial_\varphi\tilde{\theta} + \nabla\varphi\times\nabla\chi. \tag{A.19}$$

Following the methodology established in [104], we define a function $f(\mu)$ such that:

$$f(\mu) = \pi a^2 B_0 \cosh(2\mu)\frac{R}{S^2}\left(1+\partial_\nu\tilde{\theta}\right). \tag{A.20}$$

is chosen to be a function of μ. Assuming $\partial_\varphi\tilde{\theta} = 0$, we focus on the axisymmetric, φ-independent part of the poloidal angle, with the origins of $\tilde{\theta}$ and ν taken to coincide. Isolating the derivative of the angle perturbation $\tilde{\theta}$, we obtain:

$$\partial_\nu\tilde{\theta} = \frac{f(\mu)S^2(\mu,\nu)}{\pi a^2 B_0 \cosh(2\mu)R} - 1, \tag{A.21}$$

which can be integrated to yield $\tilde{\theta}$:

$$\tilde{\theta} = \int_0^\nu \left[\frac{f(\mu)S^2(\mu,\nu')}{\pi a^2 B_0 \cosh(2\mu)R} - 1\right] d\nu'. \tag{A.22}$$

Enforcing periodicity constraints requires:

$$\frac{1}{\pi a^2 B_0 \cosh(2\mu)}\int_0^{2\pi}\frac{S^2(\mu,\nu')}{R}d\nu' = \frac{1}{\overline{R}(\mu)}. \tag{A.23}$$

We now expand $f(\mu)$ by considering the large aspect ratio limit, where $\varepsilon =$

$\frac{a\sinh\mu}{R_0} \ll 1$:

$$\begin{aligned} f(\mu) = 2\pi\overline{R}(\mu) &= \left(\frac{1}{2\pi^2 B_0 R_0 \cosh(2\mu)} \int_0^{2\pi} \frac{\cosh^2\mu - \sin^2\nu'}{1+\varepsilon\cos\nu'} d\nu'\right)^{-1} \\ &\approx \left(\frac{1}{2\pi^2 B_0 R_0 \cosh(2\mu)} \int_0^{2\pi} (\cosh^2\mu - \sin^2\nu')(1-\varepsilon\cos\nu') d\nu'\right)^{-1} \\ &= \left(\frac{\pi\cosh(2\mu)}{2\pi^2 B_0 R_0 \cosh(2\mu)}\right)^{-1} = 2\pi B_0 R_0. \end{aligned} \tag{A.24}$$

Evaluating the integral for $\tilde{\theta}$ under this approximation gives:

$$\begin{aligned} \tilde{\theta} &= \int_0^{\nu} \left(\frac{2(\cosh^2\mu - \sin^2\nu')}{\cosh(2\mu)(1+\varepsilon\cos\nu')} - 1\right) d\nu' \\ &\approx \int_0^{\nu} \left(\frac{2}{\cosh(2\mu)}(\cosh^2\mu - \sin^2\nu')(1-\varepsilon\cos\nu') - 1\right) d\nu' \\ &= -\frac{1}{3}\mathrm{sech}(2\mu)\sin(\nu)\left[3\varepsilon\cosh(2\mu) + \varepsilon(\cos(2\nu)+2) - 3\cos\nu\right]. \end{aligned} \tag{A.25}$$

Thus, the final expression for the canonical poloidal angle θ is:

$$\theta = \nu + \tilde{\theta} = \nu - \frac{1}{3}\mathrm{sech}(2\mu)\sin(\nu)\left[3\varepsilon\cosh(2\mu) + \varepsilon(\cos(2\nu)+2) - 3\cos\nu\right]. \tag{A.26}$$

A.6 Magnetic Field Components

Differentiating θ with respect to ν yields:

$$\partial_\nu\theta = (1-\varepsilon\cos\nu)\left(\frac{\cos(2\nu)}{\cosh(2\mu)} + 1\right). \tag{A.27}$$

By applying hyperbolic identities, we find a useful relation for the Jacobian term:

$$\frac{\partial_\nu\theta}{S^2(\mu,\nu)} = \frac{2}{a^2}\frac{(1-\varepsilon\cos\nu)}{\cosh(2\mu)}. \tag{A.28}$$

This allows us to construct the contravariant components of the relevant cross-products. For $\nabla\psi\times\nabla\theta$, the components are:

$$(\nabla\psi\times\nabla\theta)^i = \frac{1}{J}\begin{pmatrix} 0 \\ 0 \\ \partial_\mu\psi\,\partial_\nu\theta \end{pmatrix} = \begin{pmatrix} 0 \\ 0 \\ \frac{1}{RS^2}\pi a^2 B_0\cosh(2\mu)\,\partial_\nu\theta \end{pmatrix} = \begin{pmatrix} 0 \\ 0 \\ \frac{2\pi B_0}{R}(1-\varepsilon\cos\nu) \end{pmatrix}. \tag{A.29}$$

Similarly, the components for $\nabla\varphi\times\nabla\chi$ are:

$$(\nabla\varphi\times\nabla\chi)^i = \frac{1}{J}\begin{pmatrix} -\partial_\nu\chi \\ \partial_\mu\chi \\ 0 \end{pmatrix}. \tag{A.30}$$

Expanding these explicit terms:

$$-\frac{1}{J}\partial_\nu\chi = \frac{2}{a^2R\cosh(2\mu)}\chi_1(\psi)m_1\sin\left(m_1(\theta-\iota_1^{\mathrm{res}}\varphi)\right)(1-\varepsilon\cos\nu), \tag{A.31}$$

and:

$$\begin{aligned}\frac{1}{J}\partial_\mu\chi = \frac{1}{S^2R}\Big\{&\tilde{\iota}(\mu)\pi a^2B_0\cosh(2\mu)+\chi_1'(\psi)\cos\left(m_1(\theta-\iota_1^{\mathrm{res}}\varphi)\right)\\ &+\chi_1(\psi)m_1\sin\left(m_1(\iota_1^{\mathrm{res}}\varphi-\theta)\right)\partial_\mu\theta\Big\}.\end{aligned} \tag{A.32}$$

Here, the partial derivative of θ with respect to μ is evaluated as:

$$\partial_\mu\theta = \varepsilon\frac{\sinh(2\mu)}{\cosh^2(2\mu)}\sin\nu\left(\frac{4}{3}+\frac{2}{3}\cos(2\nu)-2\cos\nu\right)-\varepsilon'(\mu)\frac{\sinh\nu}{\cosh(2\mu)}\left(\cosh(2\mu)+\frac{2}{3}+\frac{1}{3}\cos(2\nu)\right). \tag{A.33}$$

Finally, reconstructing the vector field yields the physical components of the magnetic field:

$$\hat{B}_r = \frac{\sqrt{\cosh^2\mu-\sin^2\nu}}{\pi aR\cosh(2\mu)}\chi_1(\psi)m_1\sin\left(m_1(\theta-\iota_1^{\mathrm{res}}\varphi)\right)(1-\varepsilon\cos\nu), \tag{A.34}$$

$$\begin{aligned}\hat{B}_\Theta = \frac{1}{2\pi SR}\Big\{&\tilde{\iota}(\mu)\pi a^2B_0\cosh(2\mu)+\chi_1'(\psi)\cos\left(m_1(\theta-\iota_1^{\mathrm{res}}\varphi)\right)\\ &+\chi_1(\psi)m_1\sin\left(m_1(\iota_1^{\mathrm{res}}\varphi-\theta)\right)\partial_\mu\theta\Big\},\end{aligned} \tag{A.35}$$

$$\hat{B}_\varphi = \frac{R}{2\pi}\frac{2\pi B_0}{R}(1-\varepsilon\cos\nu) = B_0(1-\varepsilon\cos\nu). \tag{A.36}$$

Bibliography

[1] Valavanidis A. and Vlachogianni T. "Homo Sapiens' Energy Dependence and Use Throughout Human History and Evolution". In: *WEBSITE: www.chem-tox-ecotox.org , Science Advances on Environment, Toxicol Ecotoxicology* 1 (Dec. 2013), pp. 1–32 (cit. on p. 1).

[2] Rüdiger Graf. "Energy History and Histories of Energy". In: *Journal of Modern European History* 12.3 (2014), pp. 382–400. DOI: 10.17104/1611-8944_2014_3_382. URL: https://doi.org/10.17104/1611-8944_2014_3_382 (cit. on p. 1).

[3] Frederick Soddy. *Matter and Energy*. Home University Library of Modern Knowledge. Reprinted by Henry Holt and Co., New York. London: Williams and Norgate, 1912 (cit. on p. 1).

[4] IEA. *World Energy Outlook 2024*. Paris, 2024. URL: https://www.iea.org/reports/world-energy-outlook-2024 (cit. on p. 1).

[5] IPCC. *Climate Change 2023: Synthesis Report. Contribution of Working Groups I, II and III to the Sixth Assessment Report of the Intergovernmental Panel on Climate Change*. Technical Report. Core Writing Team, H. Lee and J. Romero (eds.) Geneva, Switzerland: Intergovernmental Panel on Climate Change, 2023. DOI: 10.59327/IPCC/AR6-9789291691647 (cit. on p. 1).

[6] S. M. Mahajan, Y. Kishimoto, and J. Ongena. "Fusion energy: a sustainable pathway to meeting future global energy demands". In: *Reviews of Modern Plasma Physics* 8.1 (2024), pp. 1–42. DOI: 10.1007/s41614-024-00145-z (cit. on p. 1).

[7] Abu-Shawareb et al. "Achievement of Target Gain Larger than Unity in an Inertial Fusion Experiment". In: *Phys. Rev. Lett.* 132 (6 Feb. 2024), p. 065102. DOI: 10.1103/PhysRevLett.132.065102 (cit. on pp. 2, 5).

[8] S. E. Wurzel and S. C. Hsu. "Continuing progress toward fusion energy breakeven and gain as measured against the Lawson criteria". In: *Physics of Plasmas* 32.11 (2025), p. 112106. DOI: 10.1063/5.0297357 (cit. on p. 2).

[9] Elkhan R. S. Z. et al. "Back to the future: Revisiting the perspectives on nuclear fusion and juxtaposition to existing energy sources". In: *Energy* 290 (2024), p. 129150. ISSN: 0360-5442. DOI: https://doi.org/10.1016/j.energy.2023.129150 (cit. on p. 2).

[10] International Atomic Energy Agency. *World Fusion Outlook 2025*. Report. Accessed: 2026-01-22. Vienna, Austria: IAEA, 2025. URL: https://www.iaea.org/publications/world-fusion-outlook-2025 (cit. on pp. 2, 11).

[11] Jeffrey P Freidberg. *Plasma Physics and Fusion Energy*. Cambridge, UK: Cambridge University Press, 2008 (cit. on p. 3).

[12] JD Lawson. "Some criteria of a power producing thermonuclear reactor". In: *Proceedings of the Physical Society. Section B* 70.1 (1957), p. 6 (cit. on p. 4).

[13] John Wesson and David J Campbell. *Tokamaks*. 4th. Vol. 149. Oxford, UK: Oxford University Press, 2011 (cit. on pp. 4, 6, 8).

[14] Shao-yuan et al. Li. "Optimal Tracking for a Divergent-Type Parabolic PDE System in Current Profile Control". In: *Abstract and Applied Analysis* 2014 (2014), pp. 1–8. DOI: 10.1155/2014/170942 (cit. on p. 4).

[15] Max Planck Institute for Plasma Physics. *Wendelstein 7-X*. https://www.ipp.mpg.de/2815232/konzeptentwicklung. Accessed: 2026-01-22. 2024 (cit. on p. 4).

[16] Nuckolls J. et al. "Laser Compression of Matter to Super-High Densities: Thermonuclear (CTR) Applications". In: *Nature* 239.5368 (1972), pp. 139–142. DOI: 10.1038/239139a0 (cit. on p. 5).

[17] E. I. et al. Moses. "Symmetric Inertial Confinement Fusion Implosions at Ultra-High Laser Energies". In: *Physics of Plasmas* 17.5 (2010), p. 056305. DOI: 10.1063/1.3345100 (cit. on p. 5).

[18] Lindl J. "Development of the indirect-drive approach to inertial confinement fusion and the target physics basis for ignition and gain". In: *Physics of Plasmas* 2.11 (Nov. 1995), pp. 3933–4024. ISSN: 1070-664X. DOI: 10.1063/1.871025 (cit. on p. 5).

[19] E. I. et al. Moses. "Ignition on the National Ignition Facility: a path towards inertial fusion energy". In: *Nuclear Fusion* 49.10 (2009), p. 104022. DOI: 10.1088/0029-5515/49/10/104022 (cit. on p. 5).

[20] Stangeby P. C. "A tutorial on some basic aspects of divertor physics". In: *Plasma Physics and Controlled Fusion* 42.12B (Dec. 2000), B271. DOI: 10.1088/0741-3335/42/12B/321 (cit. on pp. 5, 8).

[21] N. et al. Mitchell. "The ITER Magnet System". In: *IEEE Transactions on Applied Superconductivity* 18.2 (2008), pp. 435–440. DOI: 10.1109/TASC.2008.921228 (cit. on p. 7).

[22] Beidler C. et al. "Physics and Engineering Design for Wendelstein VII-X". In: *Fusion Technology* 17.1 (1990), pp. 148–168. DOI: 10.13182/FST90-A29178 (cit. on p. 7).

[23] G. et al. Grieger. "Physics optimization of stellarators". In: *Physics of Fluids B: Plasma Physics* 4.7 (July 1992), pp. 2081–2091. ISSN: 0899-8221. DOI: 10.1063/1.860481 (cit. on p. 7).

[24] J. Nuhrenberg et al. “Overview on Wendelstein 7-X Theory”. In: *Fusion Technology* 27.3T (1995), pp. 71–78. DOI: 10.13182/FST95-A11947048 (cit. on p. 7).

[25] Sagara A. et al. “Optimization activities on design studies of LHD-type reactor FFHR”. In: *Fusion Engineering and Design* 83.10 (2008). Proceedings of the Eight International Symposium of Fusion Nuclear Technology, pp. 1690–1695. ISSN: 0920-3796. DOI: https://doi.org/10.1016/j.fusengdes.2008.07.029 (cit. on p. 7).

[26] Allen H. Boozer. “Theory of tokamak disruptions)”. In: *Physics of Plasmas* 19.5 (Apr. 2012), p. 058101. ISSN: 1070-664X. DOI: 10.1063/1.3703327 (cit. on p. 7).

[27] G. Partesotti. “The three-dimensional radiating structure at W7-X and its consequences for power exhaust”. PhD thesis. Institut für Physik, 2025 (cit. on p. 7).

[28] Peter C. Stangeby. *The Plasma Boundary of Magnetic Fusion Devices*. Series in Plasma Physics. Bristol: Institute of Physics Publishing, 2000. ISBN: 978-0750305594. DOI: 10.1201/9780367801489 (cit. on pp. 8, 10, 18, 20, 41, 58).

[29] Y. et al. Feng. “Comparison between stellarator and tokamak divertor transport”. In: *Plasma Physics and Controlled Fusion* 53.2 (Jan. 2011), p. 024009. DOI: 10.1088/0741-3335/53/2/024009 (cit. on pp. 8, 18, 19, 41, 60, 64, 71, 72).

[30] Federici G. et al. “Plasma-material interactions in current tokamaks and their implications for next step fusion reactors”. In: *Nuclear Fusion* 41.12 (Dec. 2001), pp. 1967–2137. DOI: 10.1088/0029-5515/41/12/218 (cit. on p. 8).

[31] Keilhacker M. et al. “Plasma Boundary Layer in Limiter and Divertor Tokamaks”. In: *Physica Scripta* 1982.T2B (Jan. 1982), p. 443. DOI: 10.1088/0031-8949/1982/T2B/022 (cit. on p. 8).

[32] Merola M. et al. “Engineering design of the ITER divertor”. In: *Fusion Engineering and Design* 85.10-12 (Dec. 2010), pp. 2312–2322. DOI: 10.1016/j.fusengdes.2010.04.041 (cit. on pp. 8, 71).

[33] ITER Physics Expert Group on Divertor, ITER Physics Expert Group on Divertor Modelling, Database, and ITER Physics Basis Editors. “Chapter 4: Power and particle control”. In: *Nuclear Fusion* 39.12 (Dec. 1999), p. 2391. DOI: 10.1088/0029-5515/39/12/304 (cit. on p. 9).

[34] Pitcher C. S. and Stangeby P. C. “Experimental divertor physics”. In: *Plasma Physics and Controlled Fusion* 39.6 (June 1997), pp. 779–930. DOI: 10.1088/0741-3335/39/6/001 (cit. on pp. 9, 19, 22).

[35] Pitts R. A. et al. “Physics basis for the first ITER tungsten divertor”. In: *Nuclear Materials and Energy* 20 (2019), p. 100696. ISSN: 2352-1791. DOI: https://doi.org/10.1016/j.nme.2019.100696 (cit. on pp. 9, 24).

[36] ASDEX Team. “The H-Mode of ASDEX”. In: *Nuclear Fusion* 29.11 (Nov. 1989), p. 1959. DOI: 10.1088/0029-5515/29/11/010 (cit. on p. 9).

[37] Loarte A. “Effects of divertor geometry on tokamak plasmas”. In: *Plasma Physics and Controlled Fusion* 43.6 (May 2001), R183–R224. DOI: 10.1088/0741-3335/43/6/301 (cit. on p. 9).

[38] Grigull P. et al. “First island divertor experiments on the W7-AS stellarator”. In: *Plasma Physics and Controlled Fusion* 43.12A (Nov. 2001), A175. DOI: 10.1088/0741-3335/43/12A/313 (cit. on p. 9).

[39] Strumberger E. “SOL studies for W7-X based on the island divertor concept”. In: *Nuclear Fusion* 36.7 (July 1996), p. 891. DOI: 10.1088/0029-5515/36/7/I06 (cit. on p. 9).

[40] Renner H. et al. “Divertor concept for the W7-X stellarator and mode of operation”. In: *Plasma Physics and Controlled Fusion* 44.6 (May 2002), p. 1005. DOI: 10.1088/0741-3335/44/6/325 (cit. on pp. 9, 13).

[41] K. et al. Ida. “Overview of Large Helical Device experiments of basic plasma physics for solving crucial issues in reaching burning plasma conditions”. In: *Nuclear Fusion* 64.11 (Aug. 2024), p. 112009. DOI: 10.1088/1741-4326/ad3a7a (cit. on p. 9).

[42] Ohyabu N. et al. “The Large Helical Device (LHD) helical divertor”. In: *Nuclear Fusion* 34.3 (Mar. 1994), p. 387. DOI: 10.1088/0029-5515/34/3/I07 (cit. on pp. 9, 13).

[43] K. A. Garcia. “Exploration of Resilient Divertors in Stellarators”. Doctoral dissertation. Madison, WI: University of Wisconsin-Madison, 2025 (cit. on p. 9).

[44] Allen H. Boozer. “Stellarator design”. In: *Journal of Plasma Physics* 81.6 (2015). DOI: 10.1017/S0022377815001373 (cit. on p. 9).

[45] Davies R. et al. “The topology of non-resonant stellarator divertors”. In: *Nuclear Fusion* 65.7 (June 2025), p. 076018. DOI: 10.1088/1741-4326/addb5d (cit. on p. 9).

[46] Boozer A. H. and Punjabi A. “Simulation of stellarator divertors”. In: *Physics of Plasmas* 25.9 (Sept. 2018), p. 092505. DOI: 10.1063/1.5042666 (cit. on p. 9).

[47] Y. et al. Shimomura. “Characteristics of the divertor plasma in neutral-beam-heated ASDEX discharges”. In: *Nuclear Fusion* 23.7 (July 1983), p. 869. DOI: 10.1088/0029-5515/23/7/002 (cit. on p. 10).

[48] Y. et al. Feng. "Understanding detachment of the W7-X island divertor". In: *Nuclear Fusion* 61.8 (June 2021), p. 086012. DOI: 10.1088/1741-4326/ac0772 (cit. on p. 11).

[49] Krychowiak M. et al. "First feedback-controlled divertor detachment in W7-X: Experience from TDU operation and prospects for operation with actively cooled divertor". In: *Nuclear Materials and Energy* 34 (2023), p. 101363. ISSN: 2352-1791. DOI: https://doi.org/10.1016/j.nme.2023.101363 (cit. on pp. 11, 30).

[50] P. Helander. "Theory of plasma confinement in non-axisymmetric magnetic fields". In: *Reports on Progress in Physics* 77.8 (2014), p. 087001. DOI: 10.1088/0034-4885/77/8/087001 (cit. on p. 11).

[51] C. D. et al. Beidler. "Benchmarking of the mono-energetic transport coefficients—results from the International Stellarator/Heliotron Profile Database". In: *Nuclear Fusion* 51.12 (2011), p. 123004. DOI: 10.1088/0029-5515/51/12/123004 (cit. on p. 12).

[52] Burhenn R. et al. "On impurity handling in high performance stellarator/heliotron plasmas". In: *Nuclear Fusion* 49.6 (2009), p. 065005. DOI: 10.1088/0029-5515/49/6/065005 (cit. on p. 12).

[53] Allen H. Boozer. "What is a stellarator?" In: *Physics of Plasmas* 5.5 (1998), pp. 1647–1655. DOI: 10.1063/1.872703 (cit. on p. 12).

[54] C. D et al. Beidler. "Demonstration of reduced neoclassical energy transport in Wendelstein 7-X". In: *Nature* 596.7871 (2021), pp. 221–226. DOI: 10.1038/s41586-021-03687-w (cit. on p. 12).

[55] T. Klinger et al. "Overview of first Wendelstein 7-X high-performance operation". In: *Nuclear Fusion* 59.11 (2019), p. 112004. DOI: 10.1088/1741-4326/ab03a7 (cit. on p. 12).

[56] Landreman M. et al. "Opportunities and priorities for stellarator theory and computation". In: *Journal of Plasma Physics* 84.4 (2018), p. 905840402. DOI: 10.1017/S002237781800067X (cit. on p. 12).

[57] Alan Goodman. "Quasi-isodynamic stellarator optimisation". PhD thesis. Institut für Physik, 2025, p. 248 (cit. on p. 12).

[58] A. et al. Bader. "Divertor design for the Helical Symmetric Experiment". In: *Journal of Plasma Physics* 83.4 (2017), p. 905830403. DOI: 10.1017/S002237781700052X (cit. on p. 13).

[59] Allen H Boozer. "Stellarators as a fast path to fusion". In: *Nuclear Fusion* 60.6 (2020), p. 065001. DOI: 10.1088/1741-4326/ab81bc (cit. on p. 13).

[60] Elsasser K. "Magnetic field line flow as a Hamiltonian problem". In: *Plasma Physics and Controlled Fusion* 28.12A (Dec. 1986), p. 1743. DOI: 10.1088/0741-3335/28/12A/001 (cit. on p. 14).

[61] Lise-Marie Imbert-Gérard, Elizabeth J. Paul, and Adelle M. Wright. *An Introduction to Stellarators: From Magnetic Fields to Symmetries and Optimization.* Philadelphia, PA: Society for Industrial and Applied Mathematics, 2025. ISBN: 978-1-61197-821-6. DOI: 10.1137/1.9781611978223 (cit. on p. 15).

[62] Allen H. Boozer. "Physics of magnetically confined plasmas". In: *Rev. Mod. Phys.* 76 (4 Jan. 2005), pp. 1071–1141. DOI: 10.1103/RevModPhys.76.1071 (cit. on p. 15).

[63] A. N. Kolmogorov. "On conservation of conditionally periodic motions for a small change in Hamilton's function". In: *Proceedings of the USSR Academy of Sciences* 98 (1954). (Doklady Akademii Nauk SSSR), pp. 527–530 (cit. on p. 15).

[64] V. I. Arnold. "Proof of a theorem of A. N. Kolmogorov on the invariance of quasi-periodic motions under small perturbations of the Hamiltonian". In: *Collected Works: Representations of Functions, Celestial Mechanics and KAM Theory, 1957–1965.* Ed. by A. B. Givental, B. A. Khesin, et al. Berlin, Heidelberg: Springer, 2009, pp. 267–294. ISBN: 978-3-642-01742-1. DOI: 10.1007/978-3-642-01742-1_21 (cit. on p. 15).

[65] J. Moser. "On invariant curves of area-preserving mappings of an annulus". In: *Matematika* 6.5 (1962), pp. 51–68 (cit. on p. 15).

[66] Cary J.R. and Littlejohn R.G. "Noncanonical Hamiltonian mechanics and its application to magnetic field line flow". In: *Annals of Physics* 151.1 (1983), pp. 1–34. ISSN: 0003-4916. DOI: https://doi.org/10.1016/0003-4916(83)90313-5 (cit. on p. 15).

[67] Perseo V. *Power and particle exhaust in the W7-X divertor - an introduction and overview.* Slides presented at the E2/E2M meeting. Max-Planck-Institut für Plasmaphysik, April 20, 2023. Apr. 2023 (cit. on p. 16).

[68] Y. Feng and W7-X-team. "Review of magnetic islands from the divertor perspective and a simplified heat transport model for the island divertor". In: *Plasma Physics and Controlled Fusion* 64.12 (Nov. 2022), p. 125012. DOI: 10.1088/1361-6587/ac9ed9 (cit. on pp. 16, 17, 24, 25, 34, 71).

[69] J et al. Geiger. "Physics in the magnetic configuration space of W7-X". In: *Plasma Physics and Controlled Fusion* 57.1 (Nov. 2014), p. 014004. DOI: 10.1088/0741-3335/57/1/014004 (cit. on pp. 16, 25).

[70] G. M. Zaslavskii. "The stochasticity of dynamic systems". In: *Moscow Izdatel Nauka* (Jan. 1984) (cit. on p. 16).

[71] J. D. Meiss. "Thirty years of turnstiles and transport". In: *Chaos: An Interdisciplinary Journal of Nonlinear Science* 25.9 (2015), p. 097602. DOI: 10.1063/1.4915831 (cit. on p. 16).

[72] A. Punjabi and A. H. Boozer. "Magnetic turnstiles in nonresonant stellarator divertor". In: *Physics of Plasmas* 29.1 (2022), p. 012502. DOI: 10.1063/5.0068913 (cit. on p. 16).

[73] B. V. Chirikov. "A universal instability of many-dimensional oscillator systems". In: *Physics Reports* 52.5 (1979), pp. 263–379. DOI: 10.1016/0370-1573(79)90023-1 (cit. on p. 17).

[74] Roscoe B. White. *The Theory of Toroidally Confined Plasmas*. 3rd. London: Imperial College Press, 2013. ISBN: 978-1-84816-983-8. DOI: 10.1142/p901 (cit. on p. 17).

[75] Morisaki T. et al. "Local island divertor experiments on LHD". In: *Journal of Nuclear Materials* 337-339 (2005). PSI-16, pp. 154–160. ISSN: 0022-3115. DOI: https://doi.org/10.1016/j.jnucmat.2004.10.165 (cit. on p. 17).

[76] Maaziz N. et al. To be published. 2026 (cit. on pp. 18, 23, 24, 58, 63).

[77] M. et al. Kobayashi. "3D effects of edge magnetic field configuration on divertor/scrape-off layer transport and optimization possibilities for a future reactor". In: *Nuclear Fusion* 55.10 (Sept. 2015), p. 104021. DOI: 10.1088/0029-5515/55/10/104021 (cit. on pp. 18, 19).

[78] S. I. Braginskii. "Transport Processes in a Plasma". In: *Reviews of Plasma Physics*. Ed. by M. A. Leontovich. Vol. 1. New York: Consultants Bureau, 1965, pp. 205–311 (cit. on pp. 18, 26).

[79] Sardei F. et al. "Island divertor studies on W7-AS". In: *Journal of Nuclear Materials* 241-243 (1997), pp. 135–148. ISSN: 0022-3115. DOI: https://doi.org/10.1016/S0022-3115(97)80036-0 (cit. on p. 19).

[80] P. C. Stangeby. "Can detached divertor plasmas be explained as self-sustained gas targets?" In: *Nuclear Fusion* 33.11 (1993), pp. 1695–1705. DOI: 10.1088/0029-5515/33/11/I08 (cit. on pp. 19, 22).

[81] V. et al. Perseo. "Direct measurements of counter-streaming flows in a low-shear stellarator magnetic island topology". In: *Nuclear Fusion* 59.12 (Sept. 2019), p. 124003. DOI: 10.1088/1741-4326/ab4320 (cit. on p. 21).

[82] V. et al. Perseo. "2D measurements of parallel counter-streaming flows in the W7-X scrape-off layer for attached and detached plasmas". In: *Nuclear Fusion* 61.11 (Oct. 2021), p. 116039. DOI: 10.1088/1741-4326/ac277a (cit. on p. 21).

[83] David Bohm. "Minimum Ionic Kinetic Energy for a Stable Sheath". In: *The Characteristics of Electrical Discharges in Magnetic Fields*. Ed. by Andrew Guthrie and R. K. Wakerling. National Nuclear Energy Series. New York: McGraw-Hill, 1949, pp. 77–86 (cit. on p. 21).

[84] P. C. Stangeby. "Plasma sheath transmission factors for tokamak edge plasmas". In: *The Physics of Fluids* 27.3 (Mar. 1984), pp. 682–690. ISSN: 0031-9171. DOI: 10.1063/1.864677 (cit. on p. 21).

[85] Y. et al. Feng. "Physics of island divertors as highlighted by the example of W7-AS". In: *Nuclear Fusion* 46.8 (July 2006), p. 807. DOI: 10.1088/0029-5515/46/8/006 (cit. on pp. 22, 63, 66).

[86] Maaziz N. et al. "Investigating the role of divertor geometry on density build-up in the island divertor". In: *Nuclear Materials and Energy* 42 (2025), p. 101886. ISSN: 2352-1791. DOI: https://doi.org/10.1016/j.nme.2025.101886 (cit. on pp. 22, 30, 46, 71).

[87] Lyman Spitzer and Richard Härm. "Transport Phenomena in a Completely Ionized Gas". In: *Physical Review* 89.5 (1953), pp. 977–981. DOI: 10.1103/PhysRev.89.977 (cit. on p. 22).

[88] Leonard A.W. "Plasma detachment in divertor tokamaks". In: *Plasma Physics and Controlled Fusion* 60.4 (Feb. 2018), p. 044001. DOI: 10.1088/1361-6587/aaa7a9 (cit. on p. 24).

[89] H. P. Summers, W. J. Dickson, M. G. O'Mullane, N. R. Badnell, and A. D. Whiteford. "Ionization state, excited populations and emission of impurities in dynamic finite density plasmas: I. The generalized collisional–radiative model for light elements". In: *Plasma Physics and Controlled Fusion* 48.2 (2006), pp. 263–293. DOI: 10.1088/0741-3335/48/2/007 (cit. on p. 24).

[90] D. et al. Reiter. "Burn condition, helium particle confinement and exhaust efficiency". In: *Nuclear Fusion* 30.10 (1990), p. 2141. DOI: 10.1088/0029-5515/30/10/015 (cit. on p. 24).

[91] V. et al. Haak. "Overview over the neutral gas pressures in Wendelstein 7-X during divertor operation under boronized wall conditions". In: *Plasma Physics and Controlled Fusion* 65.5 (2023), p. 054002. DOI: 10.1088/1361-6587/acc8fb (cit. on p. 24).

[92] V.R. et al. Winters. "First experimental confirmation of island SOL geometry effects in a high radiation regime on W7-X". In: *Nuclear Fusion* 64.12 (Oct. 2024), p. 126047. DOI: 10.1088/1741-4326/ad820e (cit. on pp. 25, 33, 46, 71).

[93] K. Ikeda. "Progress in the ITER Physics Basis". In: *Nuclear Fusion* 47.6 (June 2007), E01. DOI: 10.1088/0029-5515/47/6/E01 (cit. on p. 25).

[94] Feng Y. et al. "A 3D Monte Carlo code for plasma transport in island divertors". In: *Journal of Nuclear Materials* 241-243 (1997), pp. 930–934. ISSN: 0022-3115. DOI: https://doi.org/10.1016/S0022-3115(97)80168-7 (cit. on p. 26).

[95] Y et al. Feng. "Monte-Carlo fluid approaches to detached plasmas in non-axisymmetric divertor configurations". In: *Plasma Physics and Controlled Fusion* 59.3 (Feb. 2017), p. 034006. DOI: 10.1088/1361-6587/59/3/034006 (cit. on p. 26).

[96] Sergei Olegovich Makarov. "Development and Implementation of a Generalized Multi-Ion Transport Model in Plasma Edge Fluid Codes". Doctoral dissertation. Munich: Technische Universität München, 2024. URL: https://mediatum.ub.tum.de/doc/1716263/document.pdf (cit. on p. 26).

[97] Feng Y. et al. "3D fluid modelling of the edge plasma by means of a Monte Carlo technique". In: *Journal of Nuclear Materials* 266-269 (1999), pp. 812–818. ISSN: 0022-3115. DOI: https://doi.org/10.1016/S0022-3115(98)00844-7 (cit. on p. 26).

[98] Reiter D. et al. "The EIRENE and B2-EIRENE Codes". In: *Fusion Science and Technology* 47.2 (2005), pp. 172–186. DOI: 10.13182/FST47-172 (cit. on p. 27).

[99] D. Reiter. *The data file AMJUEL: additional atomic and molecular data for EIRENE*. Tech. rep. Forschungszentrum Jülich GmbH, 2000. URL: http://www.eirene.de (cit. on p. 27).

[100] D. Reiter and R. K. Janev. *The data file HYDEL: hydrocarbon data for EIRENE*. Tech. rep. Forschungszentrum Jülich GmbH, 2000. URL: http://www.eirene.de (cit. on p. 27).

[101] H. P. Summers. *The ADAS User Manual, version 2.6*. Atomic Data and Analysis Structure. 2004. URL: http://www.adas.ac.uk (cit. on p. 27).

[102] Frerichs H. et al. "Stabilization of EMC3-EIRENE for detachment conditions and comparison to SOLPS-ITER". In: *Nuclear Materials and Energy* 18 (2019), pp. 62–66. ISSN: 2352-1791. DOI: https://doi.org/10.1016/j.nme.2018.11.022 (cit. on p. 28).

[103] H. Frerichs. "FLARE: field line analysis and reconstruction for 3D boundary plasma modeling". In: *Nuclear Fusion* 64.10 (Sept. 2024), p. 106034. DOI: 10.1088/1741-4326/ad7303 (cit. on pp. 28, 29).

[104] Makarov S. O. et al. To be published. 2026 (cit. on pp. 28, 29, 33, 71, 75, 77).

[105] A. Baillod. "Equilibrium pressure limits in stellarators". PhD thesis. Lausanne: École Polytechnique Fédérale de Lausanne (EPFL), 2023. DOI: 10.5075/epfl-thesis-10070 (cit. on p. 29).

[106] Sunn Pedersen T. "Experimental confirmation of efficient island divertor operation and successful neoclassical transport optimization in Wendelstein 7-X". In: *Nuclear Fusion* 62.4 (Apr. 2022), p. 042022. DOI: 10.1088/1741-4326/ac2cf5 (cit. on pp. 30, 71).

[107] M. et al. Jakubowski. "Overview of the results from divertor experiments with attached and detached plasmas at Wendelstein 7-X and their implications for steady-state operation". In: *Nuclear Fusion* 61.10 (Aug. 2021), p. 106003. DOI: 10.1088/1741-4326/ac1b68 (cit. on p. 33).

[108] Kharwandikar A. "Power Exhaust Investigations in the W7-X Island Divertor". Inauguraldissertation. Universität Greifswald, Mar. 2025 (cit. on p. 38).

[109] Moulton D. et al. “Using SOLPS to confirm the importance of total flux expansion in Super-X divertors”. In: *Plasma Physics and Controlled Fusion* 59.6 (May 2017), p. 065011. DOI: 10.1088/1361-6587/aa6ce9 (cit. on p. 52).

[110] Thompson M. W. “The energy spectrum of ejected atoms during the high energy sputtering of gold”. In: *Philosophical Magazine* 18.153 (1968), pp. 377–414. DOI: 10.1080/14786436808227358 (cit. on p. 52).

[111] P. C. Stangeby. “Basic physical processes and reduced models for plasma detachment”. In: *Plasma Physics and Controlled Fusion* 60.4 (2018), p. 044022. DOI: 10.1088/1361-6587/aaacf6 (cit. on p. 59).

[112] Kotov V. and Reiter D. “Two-point analysis of the numerical modelling of detached divertor plasmas”. In: *Plasma Physics and Controlled Fusion* 51.11 (Oct. 2009), p. 115002. DOI: 10.1088/0741-3335/51/11/115002 (cit. on p. 59).

[113] Kobayashi M. “Transport Characteristics in the Stochastic Magnetic Boundary of LHD: Magnetic Field Topology and Its Impact on Divertor Physics and Impurity Transport”. In: *Fusion Science and Technology* 58.1 (2010), pp. 220–231. DOI: 10.13182/FST10-A10809 (cit. on p. 59).

[114] P. et al. Virtanen. “SciPy 1.0: Fundamental Algorithms for Scientific Computing in Python”. In: *Nature Methods* 17 (2020), pp. 261–272. DOI: 10.1038/s41592-019-0686-2 (cit. on p. 61).

[115] Stangeby P.C. et al. “Onion-skin method (OSM) analysis of DIII-D edge measurements”. In: *Journal of Nuclear Materials* 290-293 (2001). 14th Int. Conf. on Plasma-Surface Interactions in Controlled Fusion D evices, pp. 733–737. ISSN: 0022-3115. DOI: https://doi.org/10.1016/S0022-3115(00)00532-8 (cit. on pp. 65, 73).

[116] Stangeby P.C. et al. “Onion-skin method (OSM) analysis of DIII-D edge measurements”. In: *Journal of Nuclear Materials* 290-293 (2001). 14th Int. Conf. on Plasma-Surface Interactions in Controlled Fusion D evices, pp. 733–737. ISSN: 0022-3115. DOI: https://doi.org/10.1016/S0022-3115(00)00532-8 (cit. on p. 66).

List of Figures

List of Tables

Acknowledgements

This thesis would have never existed without the help and support of several valuable people.

I would first like to thank my academic supervisor, Professor Fabio Subba, both for making this incredible experience possible in the first place, and for his constant support in navigating the unexpected events met along the way.

I am deeply grateful to my external supervisor, Felix Reimold, for welcoming me into his research group and making me immediately feel like part of the family. I owe him a great debt of gratitude for his expert guidance through the complex topics of stellarators and island divertor transport. I am immensely thankful for his unwavering support through every challenge, and for imparting essential insights into the scientific research process. His vision and dedication to advancing stellarator research are truly inspiring.

I would like to extend my gratitude to my co-supervisor, Nassim Maaziz, for his incredibly generous and selfless support. His invaluable guidance in navigating the complex computational and modelling tools was essential to the realization of this thesis.

I would also like to thank the whole IPP E5 department for the excellent professional environment and the friendships cultivated during my time there.

I am also deeply thankful to all the people I met in Turin who accompanied me on this journey; each of you has left a lasting mark on me.

To my friends, Nicolò and Gabriel: without you, I would not be the person I am today. This thesis is also the result of the constant encouragement and personal

growth that our friendship has brought into my life.

I am particularly grateful to Elisa, who stood by me unwaveringly through all the highs and lows. I thank her from the bottom of my heart for her endless patience and for giving me so much during these years.

To my parents, for raising me and shaping me into the person I am today.

Finally, my most profound gratitude goes to my grandmother, Paola. Thank you for the endless love you have always given me, for making my university studies possible and for allowing me to complete this incredible journey.